Quasicentroid Molecular Dynamics

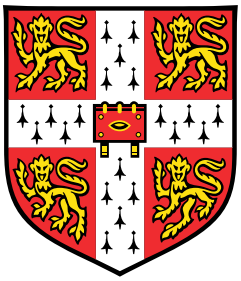

Georgijs Trenins

Department of Chemistry
University of Cambridge

This thesis is submitted for the degree of
Doctor of Philosophy

St Catharine's College

April 2020

Declaration

This thesis is the result of my own work and includes nothing which is the outcome of work done in collaboration except as declared in the Preface and specified in the text. It is not substantially the same as any that I have submitted, or, is being concurrently submitted for a degree or diploma or other qualification at the University of Cambridge or any other University or similar institution except as declared in the Preface and specified in the text. I further state that no substantial part of my thesis has already been submitted, or, is being concurrently submitted for any such degree, diploma or other qualification at the University of Cambridge or any other University or similar institution except as declared in the Preface and specified in the text. It does not exceed the prescribed word limit for the relevant Degree Committee

Georgijs Trenins
April 2020

Quasicentroid Molecular Dynamics

Georgijs Trenins

We develop a theory for approximating quantum time-correlation functions using the classical dynamics of coordinates subject to thermally averaged Feynman path fluctuations ("the mean field"). This theory approximates the dynamics of systems at thermal equilibrium that follow quantum Boltzmann statistics and undergo rapid quantum decoherence. As it relies on purely classical mechanics, the theory leads to simulation methods that scale favourably with the number of particles, and can be used for modelling condensed-matter systems.

We begin with the path-integral Liouvillian operator, which gives rise to exact quantum time-correlation functions but does not generate classical dynamics. By thermally averaging the fluctuations about smooth Feynman paths, we obtain an approximation in terms of purely classical trajectories. This presents an alternative derivation of Matsubara dynamics, a theory for approximating quantum time-correlation functions first developed by Althorpe and co-workers. As in the original formulation, the Matsubara thermal distribution function includes a complex phase, which gives rise to a sign problem. Unlike in the original, restricting the shapes of the smooth paths (limiting the number of Matsubara modes) only changes the accuracy of the dynamics, while the mean-field thermal distribution remains exact. This improves convergence with respect to the number of Matsubara modes, enough to achieve meaningful results for a two-dimensional model potential.

The results prompt us to apply a mean-field approximation to Matsubara dynamics itself. We show that such approximations can be made phase-free for certain choices of fluctuation coordinates. Our particular choice is based on average bond-angle coordinates, called "quasicentroids", due to their proximity to the true centroids of the Feynman paths. This "quasicentroid molecular dynamics", or QCMD, closely approximates the vibrational spectra of model gaseous and condensed-phase water over a broad range of temperatures, improving significantly on the established path-integral methods. We anticipate that QCMD will perform equally well for more sophisticated models and will soon be extended to general molecular systems.

Preface

I am profoundly grateful to Stuart Althorpe, who has been an outstanding supervisor, and whose insight, breadth of knowledge, and mathematical acumen never cease to inspire. I am also indebted to Michael Willatt, who first encouraged me to work in the field of path-integral methods, and who very kindly and patiently supported me during my first few years in the Althorpe group. The TRPMD+GLE(C) simulations in Chapter 5 have been performed by him. Thanks is due to Andreea Filip, who first explored the formation of artificial instantons in gaseous water, and to Raz Benson, who took the time to read through this entire work and supplied me with many useful comments and corrections. I am grateful also to all other members of the Althorpe group, past and present,—you have been a pleasure to work with. I thank Mariana Rossi for supplying the LMon-4 data used in Chapter 5, and Michele Ceriotti, for letting me work on the implementation of QCMD in i-PI. I acknowledge the Cambridge Trust for funding my degree through the Vice-Chancellor's Award, and thank St Catharine's College, and Peter Wothers in particular, for their continued support. Lastly, I am forever indebted to my parents, who have backed me every step of the way—I could never thank you enough.

Contents

List of Figures

List of Tables

Nomenclature

Latin Symbols

A_N	estimator of property A, Eq. (2.39)
A_M	estimator of property A, restricted to the Matsubara subspace, Eq. (3.2)
$\mathbf{c}$	minus the imaginary-time derivative of $\boldsymbol{\xi}$, Eq. (4.12)
C_{AB}	thermal time-correlation function of properties A and B, Eqs. (2.9) and (2.20)
$\widetilde{C}_{AB}^{[M]}$	M-mode Matsubara approximation to the quantum KTCF, Eq. (3.12)
$\mathscr{C}_{AB}^{[a]}$	curvilinear mean-field approximation to the quantum KTCF, Eq. (4.19)
$\overline{C}_{AB}$	QCMD approximation to the quantum KTCF, Eq. (4.29)
e	base of the natural logarithm, 2.71828…
$\mathcal{F}$	free energy, Eqs. (2.51) and (3.9)
$\mathbf{G}$	metric tensor, Eq. (4.3)
H	Hamiltonian function
$\hat{H}$	Hamiltonian operator
H_N	ring-polymer Hamiltonian, Eq. (2.29)
$\widetilde{H}_N$	normal-mode Hamiltonian, Eq. (2.45)
$\widetilde{H}_M$	truncated Matsubara Hamiltonian, Eq. (2.54)
$\mathcal{H}_M$	mean-field Matsubara Hamiltonian, Eqs. (3.13) and (4.2)
$\mathscr{H}_{\mathrm{MF}}$	mean-field curvilinear Hamiltonian, Eq. (4.16)
$\overline{H}$	QCMD Hamiltonian, Eq. (4.30)
i	imaginary unit, $\sqrt{-1}$

k_B	Boltzmann constant, $1.380\,649 \times 10^{-23}\ \mathrm{J\,K^{-1}}$
$\hat{L}_N$	exact path-integral Liouvillian, Eq. (A.22)
$\mathcal{L}$	classical Liouvillian, Eq. (2.3)
$\hat{L}_\mathrm{MF}$	mean-field Matsubara Liouvillian, Eq. (3.8)
$\mathscr{L}_\mathrm{MF}$	curvilinear mean-field Liouvillian, Eq. (4.8)
M	number of Matsubara modes (assumed odd)
m	particle mass
N	number of ring-polymer beads (unless stated otherwise)
$\mathbf{p}$	Cartesian (bead) momenta
$\widetilde{\mathbf{P}}$	normal-mode momenta, Eq. (2.40)
$\widetilde{P}_0$	centroid momentum, Eq. (2.42)
$\widetilde{\mathbf{P}}_M$	Matsubara momenta $\widetilde{P}_{\lvert n\rvert\le(M-1)/2}$
$\overline{\mathbf{P}}$	quasicentroid momenta conjugate to $\overline{\mathbf{Q}}$
$\mathbf{q}$	Cartesian (bead) positions
$\widetilde{\mathbf{Q}}$	normal-mode positions, Eq. (2.40)
$\widetilde{Q}_0$	centroid position, Eq. (2.42)
$\widetilde{\mathbf{Q}}_M$	Matsubara positions $\widetilde{Q}_{\lvert n\rvert\le(M-1)/2}$
$\overline{\mathbf{Q}}$	quasicentroid positions, Eq. (4.25)
S_N	ring-polymer spring energy, Eq. (2.30)
$\widetilde{S}_N$	normal-mode spring energy, Eq. (2.43)
$\widetilde{S}_M$	Matsubara mode spring energy, Eq. (3.10)
T	thermodynamic temperature
t	real time
$\hat{T}$	kinetic energy operator; not to be confused with temperature T
T_{ln}	normal-mode transformation matrix, Eq. (2.41)
V	potential energy function

$\hat{V}$	potential energy operator
$\widetilde{V}_N$	normal-mode potential energy, Eq. (2.45)
$\widetilde{V}_M$	truncated Matsubara potential energy, Eq. (3.16)
W_N	total potential energy of a ring polymer [with springs, see Eq. (3.11)]
Z	partition function, Eqs. (2.8) and (2.19)
Z_N	ring-polymer partition function, Eq. (2.28)

Greek Symbols

β	reciprocal thermodynamic temperature, $1/k_\mathrm{B}T$
β_N	$= \beta/N$
ϵ_0	vacuum permittivity, $8.854187\ldots\times10^{-12}\ \mathrm{F\,m^{-1}}$
γ	adiabaticity parameter, Eq. (3.26); not to be confused with friction γ_n
γ_n	friction experienced by the n-th normal mode
λ	path-integral Langevin equation friction parameter, Eq. (2.48)
μ	index of the highest Matsubara mode, $(M-1)/2$
$\boldsymbol{\mu}$	dipole moment
ω_N	natural frequency of a ring-polymer spring, $1/\beta_N\hbar$
ω_n	n-th normal-mode frequency of a free ring polymer, Eq. (2.44)
$\widetilde{\omega}_n$	n-th bosonic Matsubara frequency, Eq. (3.3)
π	pi (the circle constant), 3.14159…
$\boldsymbol{\pi}$	momenta conjugate to the curvilinear coordinates $\boldsymbol{\xi}$, Eq. (4.1)
$\overline{\boldsymbol{\pi}}$	curvilinear momenta $\boldsymbol{\pi}$, shifted into the complex plane, Eq. (4.5)
$\overline{\boldsymbol{\pi}}_a$	non-mean-fielded (dynamical) curvilinear momenta
$\overline{\boldsymbol{\pi}}_b$	mean-fielded curvilinear momenta
τ	imaginary time
$\boldsymbol{\tau}$	torque, Eq. (5.9); not to be confused with imaginary time
θ_M	Matsubara phase, Eq. (3.14)

$\boldsymbol{\xi}$	curvilinear ring-polymer coordinates Eq. (4.1)
$\boldsymbol{\xi}_a$	non-mean-fielded (dynamical) curvilinear coordinates
$\boldsymbol{\xi}_b$	mean-fielded curvilinear coordinates

Other Symbols

$[\,\cdot,\cdot\,]$	commutator, Eq. (2.16)
$\{\,\cdot,\cdot\,\}$	Poisson bracket, Eq. (2.4)
$\langle\,\cdot\,\rangle$	thermal average, Eqs. (2.7) and (2.18)
Δt	integration time step
$\hbar$	reduced Planck constant, $1.05457\ldots\times10^{-31}$ J s
$K_\beta(\hat{A})$	Kubo transform of operator $\hat{A}$, Eq. (2.21)
$\mathrm{Tr}[\hat{A}]$	trace of operator $\hat{A}$ (see [1, Ch. 1])

Acronyms / Abbreviations

ACF	Autocorrelation Function
ACMD	Adiabatic Centroid Molecular Dynamics
AQCMD	Adiabatic Quasicentroid Molecular Dynamics
CMD	Centroid Molecular Dynamics
CoM	Centre of Mass
DVR	Discrete Variable Representation
GLE	Generalised Langevin Equation
HEOM	Hierarchical Equations Of Motion
KTCF	Kubo-transformed Time-Correlation Function
LMon	Local Monomer
LNM	Local Normal Mode
LSC-IVR	Linearised Semiclassical Initial Value Representation
MC	Monte Carlo
MCTDH	Multi-Configuration Time-Dependent Hartree

MD	Molecular Dynamics
MF	Mean Field
NQE	Nuclear Quantum Effect
PA-CMD	Partially Adiabatic Centroid Molecular Dynamics
PILE	Path-Integral Langevin Equation
PIMC	Path-Integral Monte Carlo
PIMD	Path-Integral Molecular Dynamics
QCMD	Quasicentroid Molecular Dynamics
QTST	Quantum Transition-State Theory
QUAPI	Quasiadiabatic Propagator Path Integral
RDF	Radial Distribution Function
RPMD	Ring-Polymer Molecular Dynamics
SC-IVR	Semiclassical Initial Value Representation
TCF	Time-Correlation Function
TRPMD	Thermostatted Ring-Polymer Molecular Dynamics
ZPE	Zero-Point Energy

Chapter 1

Introduction

The behaviour of atoms in chemical systems is guided by the laws of quantum mechanics and cannot be accurately described within a purely classical framework. Nevertheless, it appears that a range of properties can be approximated to a high degree of accuracy by a combination of quantum Boltzmann statistics with classical Newtonian dynamics [2–21]. In this work we apply this idea to the simulation of water, developing what we believe is the best quantum–classical approximation of its vibrational spectrum to date [22]. The new approximation is the titular Quasicentroid Molecular Dynamics, which produces more accurate results for simulated vibrational fundamentals of water than any of the established quantum–classical approximations, and which we believe to be generalisable to near arbitrary molecular systems.

To begin, we review some of the alternative approaches to simulations of quantum systems and then address why an approximate treatment is necessary for systems such as liquid water. We note at the outset that all of our calculations are performed in the Born–Oppenheimer approximation [23], and that the electronic structure part of the problem is assumed to have been treated elsewhere. The question of simulating a quantum system is therefore reduced to one of simulating the motion of its nuclei. One way of approaching this is to solve the time-independent nuclear Schrödinger equation and describe the time-evolution in terms of the resulting stationary states [1]. This can be done efficiently in the discrete variable representation (DVR) [24, 25], which transforms the Schrödinger equation into a sparse matrix eigenvalue problem. Alternatively, one can solve the time-*dependent* Schrödinger equation directly, as done in wavepacket propagation methods such as Multi-Configuration Time-Dependent Hartree (MCTDH) [26–29]. This approach casts the Schrödinger equation as a set of equations of motion, which can be integrated efficiently provided that the propagation time is kept relatively short.

The fundamental difficulty with both these approaches is that they rely on a basis-set representation of the wavefunction, which grows exponentially with the number of degrees of freedom. This puts a limit on the number of atoms that can be treated using such direct approaches, restricting accessible system sizes to six atoms in reactive scattering calculations [30, 31], and just under twenty atoms in calculations of vibrational spectra [32, 33]. Larger systems can be accessed if one is only interested in the dynamics of a small subset of all the degrees of freedom, and is prepared to model the rest as a harmonic bath. The bath can be treated analytically, and its effect expressed in terms of an influence functional [34, 35]. This idea is at the core of the Quasiadiabatic Propagator Path Integral (QUAPI) method developed by Makri and co-workers [36, 37], and of the Hierarchical Equations Of Motion (HEOM) approach by Tanimura and co-workers [38, 39]. Both approaches have been widely successful in describing the dynamics of quantum dissipative systems [40–44], but are ultimately limited to low-dimensional system-bath problems.

The unfavourable scaling of exact quantum calculations is in contrast to classical simulations, which benefit from two important properties. First, trajectories are well-defined in classical mechanics and can be used to describe the time-evolution of any function by following the progress of a point through phase space [45, 46]. This is not possible in quantum mechanics, since the uncertainty principle prevents localisation at such a point, and one must therefore propagate a phase-space distribution instead [47]. Second, the properties calculated in classical simulations are typically given by multidimensional integrals that are amenable to calculation by importance sampling. Various Molecular Dynamics (MD) and Monte Carlo (MC) approaches have been developed to this end [48–50], and it would be of great benefit if they could also be employed in the study of quantum systems. This has become possible with the advance of semiclassical theories, capable of approximating nuclear quantum effects (NQEs), which include quantum coherence, zero-point energy, and tunnelling. These theories are based on an asymptotic approximation to the exact quantum propagator, which is expressed as an integral over classical trajectories with complex weights. The most useful of these has proven to be the Semiclassical Initial Value Representation (SC-IVR) and its various approximations [2, 4, 51–54]. The latter are a practical necessity, since inherent to SC-IVR is the evaluation of multidimensional oscillatory integrals that are not easily tackled by importance sampling—a feature commonly referred to as the "sign problem". Techniques have been developed that ameliorate this and make semiclassical calculations feasible for systems of tens of atoms [55–58], although simulations of condensed-matter systems at thermodynamic equilibrium remain beyond reach. The one exception is the classical Wigner or *linearised* semiclassical initial value representation (LSC-IVR), which offers a highly practical approx-

imation for thermal time-correlation functions [59, 60]. Semiclassically, a time-correlation function is given by an integral over phase space that involves the interference between a pair of classical paths, which LSC-IVR approximates to first order in their difference. The result is a time-correlation of Wigner functions calculated along classical trajectories, initialised from the thermal Wigner distribution [47]. Subject to a further, physically motivated approximation [61], this distribution can be sampled efficiently using Path-Integral Molecular Dynamics (PIMD—see below). LSC-IVR simulations are thus feasible for systems such as liquid water, and give good short-time approximations to their quantum time-correlation functions [11, 62–64]. Despite this, there is a major flaw in the method, since classical trajectories do not conserve the thermal Wigner distribution, causing zero-point energy leakage from high- to low-frequency degrees of freedom [11, 62, 65]. The effects of this can be seen in the spurious melting of crystal lattices in water ice simulations (on sub-picosecond timescales), as well as in the unphysical broadening and shifting of simulated infrared absorption bands [22].

Another criticism of LSC-IVR is that the linearisation approximation implies a complete neglect of real-time quantum coherence [52, 66]. However, in condensed-phase simulations for which zero-point energy leakage is not too severe, LSC-IVR tends to approximate the properties of quantum systems very well [67–69]. Therefore an alternative and fruitful interpretation is that quantum coherence does not play a major role in the dynamics of extended quantum systems at thermal equilibrium, and that it should be possible to approximate their behaviour by combining exact quantum statistics (which accounts for the static NQEs like zero-point energy and tunnelling) with classical dynamics. This is an attractive proposition, since efficient techniques for simulating exact quantum Boltzmann statistics have by now become well-established. These are based on the observation that, within the path-integral formulation of quantum mechanics, there is an exact isomorphism between the quantum Boltzmann distribution and the Boltzmann distribution of an extended classical system. This quantum–classical isomorphism was first identified by Feynman and Hibbs [35], and applied to molecular simulations by Chandler and Wolynes [70]. Since it relies on purely classical mechanics, the isomorphic representation can employ classical techniques for simulating quantum systems at thermal equilibrium, giving rise to Path-Integral Monte Carlo (PIMC) and Path-Integral Molecular Dynamics (PIMD) [50]. Recent advances [71–75] have reduced the cost of such simulations to no more than a few times that of the analogous classical calculations, so that they can now be done routinely for complex systems [21, 76, 77].

Unfortunately no such exact quantum–classical isomorphism exists for real-time quantum propagation. However, it is possible to combine the path-integral representation of the quantum Boltzmann distribution with classical dynamics in a way that ensures the distribution

is conserved. This kind of approach was pioneered by Cao and Voth [78], who introduced the Centroid Molecular Dynamics (CMD) method. This was followed by the development of Ring-Polymer Molecular Dynamics (RPMD) by Craig and Manolopoulos [5], and Thermostatted Ring-Polymer Molecular Dynamics (TRPMD) by Rossi *et al.* [15]. All three methods are free from zero-point energy leakage and are exact in a number of important limits. Even so, they were originally introduced as heuristic techniques and lacked a clear connection with exact quantum theory. (T)RPMD was given some justification when its connection with exact quantum transition state theory (QTST) was established [18, 79, 80]. However the biggest change came about with the development of Matsubara dynamics by Althorpe and co-workers [81], who have shown that the path-integral representation of the exact quantum propagator is classical when restricted to the subspace of smooth (Matsubara) paths. The quantum–classical isomorphism for static properties remains exact when restricted to this subspace, and since real-time propagation of smooth paths is classical without any approximation, Matsubara dynamics rigorously combines quantum statistics with classical dynamics in a way that conserves the exact quantum Boltzmann distribution. Furthermore, LSC-IVR has been shown to be an "unfiltered" version of Matsubara dynamics, in which the smooth Matsubara subspace is allowed to couple to the other, jagged coordinates. Since the dynamics of the jagged coordinates is not rigorously classical, this causes the unphysical zero-point energy leakage seen in anharmonic potentials. The harmonic potential is special, since its functional form precludes any such coupling, making Matsubara dynamics and LSC-IVR produce the same (exact) results. Therefore Matsubara dynamics has at least as firm a theoretical justification as LSC-IVR, while also being free of its spurious features.

Given the many advantages of Matsubara dynamics one might ask why it has not superseded the earlier heuristic approximations (CMD and [T]RPMD) as a practical means of simulating molecular systems. The answer to this lies in the way that the quantum Boltzmann distribution is represented in the Matsubara framework. Much like with other semiclassical approximations, nuclear quantum effects are incorporated into the thermal distribution by means of a complex phase factor, which appears deceptively simple in comparison with what is found, for example, in SC-IVR. In reality, the Matsubara sign problem is considerably more severe than in SC-IVR, and cannot be tackled by the same means. It has limited the scope of feasible numerical calculations to one-dimensional potentials—a situation that is not likely to be improved much beyond what is described in this work. Therefore the real strength of Matsubara dynamics is in its use as a theoretical framework for constructing and studying the more approximate, practical path-integral methods.

For example, it has been shown [82, 83] that one arrives at (T)RPMD starting from an analytically continued Matsubara dynamics, where the momenta have been redefined so as to absorb the phase, and then shifted onto the real axis, causing the Matsubara equations of motion to become complex. These manipulations do not involve any approximations and give rise to a Boltzmann distribution that is formally phase-free. However, the resulting trajectories are complex and no easier to converge than the original oscillatory phase-space integral. RPMD resolves this by neglecting the imaginary part of the equations of motion, while TRPMD replaces it with a Langevin equation. These approximations do not directly affect the centres of mass (the centroids) of the Matsubara paths, since the neglected terms only involve the non-centroid fluctuation coordinates. This has a bearing on how well (T)RPMD approximates different kinds of time-correlation functions, and it is found to perform much better when the correlated properties are linear in position or momentum, and therefore only depend on the centroid dynamics. For this reason we refer to RPMD and TRPMD as "centroid-following" methods. As might be deduced from its name, CMD also belongs to this category, and can be viewed as a mean-field Matsubara approximation [82]. It relies on the fact that the Matsubara phase is partitioned entirely between the non-centroid fluctuation coordinates. Hence, rather than analytically continuing and modifying their dynamics, CMD resolves the sign problem by propagating only the dynamics of the centroid, subject to thermally averaged fluctuation forces.

Since all three of these approaches make quite drastic approximations to the dynamics of Matsubara fluctuations, their predictions of certain dynamical properties suffer from serious artefacts, even if the properties depend explicitly only on the centroid coordinates. Simulated infrared absorption spectra offer a striking example of this. In RPMD, the spectra are corrupted by spurious resonances due to the fluctuation modes, which create unphysical absorption peaks and cause physical spectral features to deform and split [10]. TRPMD was designed to combat this problem, and indeed its simulated spectra give reliable estimates of peak positions [15, 16]. However the fluctuation modes, which in TRPMD are propagated according to the Langevin equation, introduce spurious friction into the dynamics of the centroids, causing spectral line shapes to broaden considerably, especially at low temperatures. Recent work by Rossi *et al.* [84] suggests that using the generalised Langevin equation (GLE) to propagate the fluctuation dynamics can mitigate this problem, although in its current form the GLE treatment corrupts the low-frequency part of the spectrum.

CMD experiences none of these problems, since it does not involve any dynamical coupling to the fluctuation modes. Of the three path-integral methods introduced here, CMD performs the best in spectroscopic simulations of bulk condensed matter at high and intermediate

temperatures, giving accurate estimates of both peak positions and spectral line shapes [10, 17, 20]. However the quality of this approximation rapidly deteriorates when the temperature is decreased beyond a certain, potential-dependent threshold, or when the simulation is conducted in the gas phase or at a liquid–gas interface. The breakdown, which involves a temperature-dependent redshift and a progressive broadening of the line shape, is known as the "curvature problem", and has previously been described by Marx and co-workers [85, 86]. Since their investigation, we are not aware of any attempts to improve on the CMD approximation in a way that is analogous to TRPMD and its GLE modification. We are therefore encouraged to subject CMD to further analysis in an effort to find a practical solution to the curvature problem.

We begin by giving a brief overview of some useful concepts in statistical thermodynamics in Chapter 2, followed by a theoretical summary of the established path-integral methods for simulating quantum systems at thermal equilibrium. In Chapter 3 we develop an alternative formulation of Matsubara dynamics, casting it as a mean-field approximation to the exact quantum theory. Our proposed formulation is equivalent to the original theory by Hele *et al.* [81] in the limit of an infinite-dimensional Matsubara subspace, but is advantageous when the number of the "smooth" degrees of freedom ("Matsubara modes") is small. This is because in the new formulation the quantum Boltzmann distribution is described exactly, regardless of how the configuration space is partitioned into Matsubara and non-Matsubara modes. Hence for the first time we are able to converge some Matsubara dynamics simulations for a chemically relevant model system, gaining new insight into the failure of the CMD approximation when applied to a two-dimensional OH diatomic. We are persuaded that CMD faithfully reproduces Matsubara dynamics spectra at sufficiently high temperatures, and enters the curvature-problem regime when its mean-field distribution ceases to be compact about the dynamical centroid coordinate. This leads us to introduce a broader class of mean-field approximations to Matsubara dynamics that extends beyond the Cartesian centroid, encompassing general sets of curvilinear coordinates. We derive this general approximation in Chapter 4 and give a sufficient condition for the approximate dynamics to be real and phase-free. In the same chapter, we give a particular example of curvilinear coordinates, whose mean-field dynamics produces remarkably accurate approximations to Matsubara dynamics spectra of the two-dimensional OH model, at all temperatures tested, with no sign of the curvature problem. Since the new approach is based on the centroids of plane polar coordinates, which are invariably close to the Cartesian centroids for thermally accessible path configurations, we call the new method Quasicentroid Molecular Dynamics or QCMD. In Chapter 5 we extend this approach to QCMD simulations of gaseous and condensed-

phase water. The gas-phase simulations show none of the spurious features associated with TRPMD or CMD, and are believed by us to approach the highest level of accuracy that can be expected of a (quasi-)centroid following method in the context of vibrational dynamics. With the exception of some minor deviations in the libration peak region due to a known approximation to the quasicentroid torque, the same is true for simulations of liquid water and ice. In Chapter 6 we discuss how these results can be further improved, speculating, backed by preliminary work, on the extension of QCMD to arbitrary non-dissociative molecular systems. We conclude the discussion by outlining the fundamental limitations of centroid-following methods, namely their inability to accurately describe phenomena that depend explicitly on the dynamics of non-centroid fluctuations. These include overtones, combination bands, and Fermi resonances—all of which can be approximately captured by LSC-IVR. It may therefore be possible to describe these features using a suitable quantum–classical approximation derived within the Matsubara dynamics framework, and we hope that the generalised mean-field theory presented in this work can serve as a starting point for such development.

Chapter 2

Background theory

2.1 Thermal averages and time-correlation functions

When it comes to describing a chemical system, we are rarely interested in the microscopic arrangement of its components. Instead, we are mostly after the average values of some of its measurable properties. For example, the pressure P exerted by N particles occupying a volume $\mathcal{V}$ at temperature T is

$$P = \frac{N k_\mathrm{B} T}{\mathcal{V}} + \left\langle \frac{1}{3\mathcal{V}} \sum_{j>i} \sum_{i} \mathbf{f}(\mathbf{r}_{ij}) \cdot \mathbf{r}_{ij} \right\rangle .$$

Here $\langle \cdot \rangle$ denotes a thermal average, k_B is the Boltzmann constant, $\mathbf{r}_{ij}$ is the displacement between particles i and j, and $\mathbf{f}(\mathbf{r}_{ij})$ is the interparticle force [49]. The value of the average does not depend on how the particles get from one arrangement to another, but only on how likely a particular arrangement is, making pressure a *static* property. Another example is the diffusion coefficient D, which can be calculated as [49]

$$D = \frac{1}{3} \int_0^\infty \mathrm{d}t \, C_{\mathbf{v}\cdot\mathbf{v}}(t) = \frac{1}{3} \int_0^\infty \mathrm{d}t \, \langle \mathbf{v}(0) \cdot \mathbf{v}(t) \rangle,$$

where t is time, $\mathbf{v}$ is a particle's velocity and $C_{\mathbf{v}\cdot\mathbf{v}}$ is the velocity autocorrelation function. This contains information on how the particles move (their dynamics), which makes the diffusion coefficient a *dynamic* property. Clearly the different kinds of thermal averages are central to the mathematical description of systems at thermodynamic equilibrium, and their precise definitions depend on whether the system follows the laws of classical or quantum mechanics.

2.1.1 Classical systems

A classical system is characterised by its total energy, which can often be decomposed into kinetic and potential energy contributions,

$$E = \sum_{j=1}^{N} \frac{p_j^2}{2m_j} + V(\mathbf{q}), \tag{2.1}$$

where p_j is the momentum of particle j, q_j is its position, m_j is its mass, and $V(\mathbf{q})$ is the potential energy function that describes the system. The expression is valid for N particles in one spatial dimension and is straightforward to generalise. In most cases[1] we can identify the total energy with the Hamiltonian, $H(\mathbf{p}, \mathbf{q}) = E$. This arises naturally in Hamiltonian mechanics [46], in which the classical laws of motion are expressed as

$$\frac{\mathrm{d}\mathbf{p}}{\mathrm{d}t} = -\frac{\partial H}{\partial \mathbf{q}} \qquad\qquad \frac{\mathrm{d}\mathbf{q}}{\mathrm{d}t} = \frac{\partial H}{\partial \mathbf{p}}. \tag{2.2}$$

Using these identities, we can write the full time derivative of property A as

$$\frac{\mathrm{d}A}{\mathrm{d}t} = \frac{\partial A}{\partial t} + \sum_{j=1}^{N} \left\{ \frac{\partial H}{\partial p_j}\frac{\partial A}{\partial q_j} - \frac{\partial H}{\partial q_j}\frac{\partial A}{\partial p_j} \right\} = \frac{\partial A}{\partial t} + \mathcal{L}A, \tag{2.3}$$

where the last term is the classical Liouvillian operator. It is sometimes written as a Poisson bracket, $\mathcal{L} = \{\,\cdot\,, H\}$, generally defined as [1]

$$\{f, g\} \equiv \sum_{j=1}^{N} \frac{\partial f}{\partial q_j}\frac{\partial g}{\partial p_j} - \frac{\partial f}{\partial p_j}\frac{\partial g}{\partial q_j}. \tag{2.4}$$

The Liouvillian formally describes how a function with no explicit time dependence changes along a trajectory,

$$A(\mathbf{p}_t, \mathbf{q}_t) = \mathrm{e}^{\mathcal{L}t} A(\mathbf{p}, \mathbf{q}), \tag{2.5}$$

where $(\mathbf{p}, \mathbf{q})$ are the initial momenta and positions, and $(\mathbf{p}_t, \mathbf{q}_t)$ are the momenta and positions after a time t. In the special case that $A(\mathbf{p}, \mathbf{q}) = H(\mathbf{p}, \mathbf{q})$, we can use the fact that $\{H, H\} = 0$ to derive the law of conservation of energy,

$$H(\mathbf{p}_t, \mathbf{q}_t) = \mathrm{e}^{\mathcal{L}t} H(\mathbf{p}, \mathbf{q}) = H(\mathbf{p}, \mathbf{q}). \tag{2.6}$$

[1] Specifically when the total energy does not explicitly depend on time.

This leads us into the discussion about classical thermal averages. A *static* property A is given by the thermal average

$$\langle A \rangle = \frac{(2\pi\hbar)^{-N}}{Z_{\mathrm{cl}}} \int \mathrm{d}^N\mathbf{p} \int \mathrm{d}^N\mathbf{q}\, \mathrm{e}^{-\beta H(\mathbf{p},\mathbf{q})} A(\mathbf{p},\mathbf{q}), \tag{2.7}$$

where $\beta = 1/k_{\mathrm{B}}T$, and

$$Z_{\mathrm{cl}} = (2\pi\hbar)^{-N} \int \mathrm{d}^N\mathbf{p} \int \mathrm{d}^N\mathbf{q}\, \mathrm{e}^{-\beta H(\mathbf{p},\mathbf{q})} \tag{2.8}$$

is the classical partition function. Various *dynamic* properties can be derived from a time-correlation function (TCF) of the form [87, Ch. 11]

$$C_{AB}(t) = \frac{(2\pi\hbar)^{-N}}{Z_{\mathrm{cl}}} \int \mathrm{d}^N\mathbf{p} \int \mathrm{d}^N\mathbf{q}\, \mathrm{e}^{-\beta H(\mathbf{p},\mathbf{q})} A(\mathbf{p},\mathbf{q})\, \mathrm{e}^{\mathcal{L}t} B(\mathbf{p},\mathbf{q}), \tag{2.9}$$

where A and B are some functions of momenta and positions. When the two functions are the same, we refer to the result as an "autocorrelation function" (ACF). The conservation law in Eq. (2.6) means that classical dynamics conserves the Boltzmann distribution,

$$\mathrm{e}^{\mathcal{L}t} \left[\frac{\mathrm{e}^{-\beta H(\mathbf{p},\mathbf{q})}}{Z_{\mathrm{cl}}} \right] = \frac{\mathrm{e}^{-\beta H(\mathbf{p},\mathbf{q})}}{Z_{\mathrm{cl}}}. \tag{2.10}$$

Hence it can be shown [88] that static thermal averages do not depend on time,

$$\langle A(t) \rangle = \langle A \rangle, \tag{2.11}$$

and that TCFs satisfy the detailed balance condition,

$$C_{AB}(t) = C_{BA}(-t). \tag{2.12}$$

We will see that the same is true for quantum systems.

2.1.2 Quantum systems

For a quantum system, every measurable property A is associated with a Hermitian operator $\hat{A}$ [1]. For example, the energy of a quantum system is given by the action of the Hamiltonian operator

$$\hat{H} = \hat{T} + \hat{V} = \sum_{j=1}^{N} \frac{\hat{p}_j^2}{2m_j} + V(\hat{\mathbf{q}}), \tag{2.13}$$

where $\hat{T}$ and $\hat{V}$ are the kinetic and potential energy contributions. In the Heisenberg picture, operators change in time according to [1]

$$\hat{A}(t) = \mathrm{e}^{\mathrm{i}\hat{H}t/\hbar}\hat{A}\mathrm{e}^{-\mathrm{i}\hat{H}t/\hbar}, \tag{2.14}$$

where $\hbar$ is the reduced Planck constant. Differentiating this with respect to time leads to the Heisenberg equation of motion,

$$\frac{\mathrm{d}\hat{A}}{\mathrm{d}t} = \frac{\partial\hat{A}}{\partial t} + \frac{1}{\mathrm{i}\hbar}\left[\hat{A},\hat{H}\right], \tag{2.15}$$

where $[\,\cdot\,,\,\cdot\,]$ is the commutator

$$\left[\hat{A},\hat{H}\right] \equiv \hat{A}\hat{H} - \hat{H}\hat{A}. \tag{2.16}$$

Note the similarity of these expressions to Eqs. (2.3) and (2.4). Since any operator commutes with itself, we can show that

$$\frac{\mathrm{d}\hat{H}}{\mathrm{d}t} = \left[\hat{H},\hat{H}\right] = 0 \tag{2.17a}$$

and

$$\hat{H}(t) = \mathrm{e}^{\mathrm{i}\hat{H}t/\hbar}\hat{H}\mathrm{e}^{-\mathrm{i}\hat{H}t/\hbar} = \mathrm{e}^{\mathrm{i}\hat{H}t/\hbar}\mathrm{e}^{-\mathrm{i}\hat{H}t/\hbar}\hat{H} = \hat{H}. \tag{2.17b}$$

In other words, quantum dynamics conserves the Hamiltonian operator. The definition of thermal averages follows the analogy with classical mechanics, so that

$$\langle A\rangle = \frac{1}{Z}\mathrm{Tr}\left[\mathrm{e}^{-\beta\hat{H}}\hat{A}\right], \tag{2.18}$$

where

$$Z = \mathrm{Tr}\left[\mathrm{e}^{-\beta\hat{H}}\right] \tag{2.19}$$

is the quantum partition function. Even though $\hat{H}$ and $\hat{A}$ generally do not commute, there is no ambiguity in the definition because the trace is invariant under cyclic permutation [89]. The same is not true of the TCF, for which multiple definitions are possible. In our case the most natural choice is the Kubo-transformed time-correlation function (KTCF),

$$C_{AB}(t) = \frac{1}{Z}\mathrm{Tr}\left[K_\beta(\hat{A})\,\mathrm{e}^{\mathrm{i}\hat{H}t/\hbar}\hat{B}\mathrm{e}^{-\mathrm{i}\hat{H}t/\hbar}\right], \tag{2.20}$$

where

$$K_\beta(\hat{A}) = \frac{1}{\beta}\int_0^\beta \mathrm{d}\lambda\, \mathrm{e}^{-\lambda\hat{H}}\,\hat{A}\mathrm{e}^{-(\beta-\lambda)\hat{H}}. \tag{2.21}$$

This form arises naturally in quantum linear response theory [87] and has the same symmetries as the classical TCF [5, 88].

Using the commutation relation in Eq. (2.17) and the cyclic permutation property of the trace it can be shown that the quantum thermal average and the KTCF satisfy Eqs. (2.11) and (2.12), just as in the classical case. This is a consequence of the quantum Boltzmann distribution being conserved by the dynamics, which will play an important role in the subsequent discussion.

2.2 Path-integral quantum statistics

The classical thermal averages in Eqs. (2.7) and (2.9) are in the form of multidimensional integrals that can be estimated using importance sampling [49, 50]. This is the basis of Monte Carlo (MC) and Molecular Dynamics (MD) methods, which can be scaled to large system sizes and are routinely used in the computational modelling of materials and biomolecules.

The wide range of simulation techniques available for this purpose make it an attractive proposition to cast the quantum thermal averages in Eqs. (2.18) and (2.20) into a similar form. For static properties this can be done by exploiting the isomorphism of the discretised path-integral representation of Eq. (2.18) with a thermal average in an extended classical system [35, 70, 90]. It will be instructive to derive this isomorphism for the quantum partition function in Eq. (2.19). First we express the trace in the eigenbasis of the position operator, which for a single particle in one dimension reads

$$Z = \mathrm{Tr}\left[\mathrm{e}^{-\beta\hat{H}}\right] = \int_{-\infty}^{\infty}\mathrm{d}q\,\langle q|\mathrm{e}^{-\beta\hat{H}}|q\rangle, \tag{2.22}$$

where we have used Dirac's bra–ket notation [1]. Next we write the quantum Boltzmann operator as the product of N identical terms,

$$\mathrm{e}^{-\beta\hat{H}} = \prod_{l=1}^{N}\mathrm{e}^{-\beta_N\hat{H}}, \tag{2.23}$$

where $\beta_N \equiv \beta/N$. Recalling that $\hat{H} = \hat{T} + \hat{V}$, we decompose the product using the symmetrised Trotter formula [91],

$$\prod_{l=1}^{N} \mathrm{e}^{-\beta_N \hat{H}} = \left[\hat{\Omega}_N\right]^N + O(N^{-2}), \tag{2.24}$$

where

$$\hat{\Omega}_N = \mathrm{e}^{-\beta_N \hat{V}/2} \mathrm{e}^{-\beta_N \hat{T}} \mathrm{e}^{-\beta_N \hat{V}/2}. \tag{2.25}$$

We then insert a resolution of the identity, $\int_{-\infty}^{\infty} \mathrm{d}q_l \, |q_l\rangle\langle q_l|$, between each pair of factors, which yields

$$Z = \lim_{N\to\infty} \prod_{l=1}^{N} \int_{-\infty}^{\infty} \mathrm{d}q_l \, \langle q_l|\hat{\Omega}_N|q_{l+1}\rangle, \tag{2.26}$$

with $q_{N+l} \equiv q_l$. In this factorised form, the matrix elements can be calculated analytically [1, 35, 90],

$$\begin{aligned} \langle q_l|\hat{\Omega}_N|q_{l+1}\rangle = \exp\left\{-\frac{\beta_N}{2}\left[V(q_l) + V(q_{l+1}) + m\omega_N^2(q_{l+1}-q_l)^2\right]\right\} \\ \times \frac{1}{2\pi\hbar}\int_{-\infty}^{\infty} \mathrm{d}p_l' \, \exp\left\{-\frac{\beta_N}{2m}\left[p_l' + \mathrm{i}m\omega_N(q_{l+1}-q_l)\right]^2\right\}, \end{aligned} \tag{2.27}$$

where $\omega_N = 1/\beta_N\hbar$. Changing the momentum variables to $p_l = p_l' + \mathrm{i}m\omega_N(q_{l+1} - q_l)$ and shifting the integration contour onto the real axis gives the final expression for the quantum partition function

$$Z = \lim_{N\to\infty} Z_N \equiv \lim_{N\to\infty} (2\pi\hbar)^{-N} \int \mathrm{d}^N\mathbf{p} \int \mathrm{d}^N\mathbf{q} \, \mathrm{e}^{-\beta_N H_N(\mathbf{p},\mathbf{q})}, \tag{2.28}$$

where we define the path-integral Hamiltonian,

$$H_N(\mathbf{p},\mathbf{q}) = \sum_{l=1}^{N}\left\{\frac{p_l^2}{2m} + V(q_l)\right\} + S_N(\mathbf{q}), \tag{2.29}$$

with spring energy

$$S_N(\mathbf{q}) = \sum_{l=1}^{N} \frac{m\omega_N^2}{2}(q_{l+1}-q_l)^2 \,. \tag{2.30}$$

The "nascent" path-integral partition function Z_N is exactly the same as the classical partition function [see Eq. (2.8)] of N replicas of the original particle, connected by harmonic springs of frequency ω_N and held at a temperature that is N times higher than the original. The springs

connect the replicas (sometimes called "beads") into a cyclic "ring polymer" and contribute a potential energy $S_N(\mathbf{q})$.

At this stage it may not be entirely clear what relation Eq. (2.28) bears to path integrals. This is made apparent once we rewrite Eq. (2.28) as

$$Z = \lim_{N\to\infty} \left[\prod_{l=1}^{N} \int_{-\infty}^{\infty} \frac{\mathrm{d}q_l}{\alpha}\right] \exp\left\{-\frac{\epsilon}{\hbar}\sum_{l=1}^{N}\left[\frac{m}{2}\left(\frac{q_{l+1}-q_l}{\epsilon}\right)^2 + V(q_l)\right]\right\}, \tag{2.31}$$

where

$$\alpha = \left(\frac{m}{2\pi\hbar\epsilon}\right)^{1/2} \qquad \text{and} \qquad \epsilon = \beta\hbar/N. \tag{2.32}$$

In the continuum picture,

$$\lim_{N\to\infty} \frac{m}{2}\left(\frac{q_{l+1}-q_l}{\epsilon}\right)^2 = \lim_{\delta\tau\to 0} \frac{m}{2}\left(\frac{q(\tau+\delta\tau)-q(\tau)}{\delta\tau}\right)^2 = \frac{m}{2}\left(\frac{\mathrm{d}q}{\mathrm{d}\tau}\right)^2, \tag{2.33}$$

and

$$\lim_{N\to\infty} \sum_{l=1}^{N} \epsilon\, f(q_l) \equiv \int_0^{\beta\hbar} \mathrm{d}\tau\, f\big(q(\tau)\big). \tag{2.34}$$

Thus the quantum partition function can be expressed as

$$Z = \oint \mathcal{D}q(\cdot)\, \mathrm{e}^{-\mathscr{A}_E[q(\cdot)]/\hbar}, \tag{2.35}$$

where $\mathscr{A}_E$ is the Euclidean action

$$\mathscr{A}_E[q(\cdot)] = \int_0^{\beta\hbar} \mathrm{d}\tau \left[\frac{m}{2}\left(\frac{\mathrm{d}q}{\mathrm{d}\tau}\right)^2 + V(q)\right], \tag{2.36}$$

and $\oint \mathcal{D}q(\cdot)$ denotes integration over all closed paths,

$$\oint \mathcal{D}q(\cdot) \equiv \lim_{N\to\infty} \left[\prod_{l=1}^{N} \int_{-\infty}^{\infty} \frac{\mathrm{d}q_l}{\alpha}\right]. \tag{2.37}$$

The symbol τ denotes *imaginary time*, so called because Eqs. (2.35) and (2.36) are related to real-time path integrals by a Wick rotation $t \to -\mathrm{i}\tau$ [35, Ch. 10]. Equation (2.28) is the discretised representation of the imaginary-time path integral, which we will use throughout; the continuous formalism in Eqs. (2.35) to (2.37) is introduced because it will be useful for our discussion of imaginary-time symmetries in Chapter 4.

As with the partition function, it is possible to cast the quantum thermal average in Eq. (2.18) into a ring-polymer form,

$$\langle A\rangle = \lim_{N\to\infty}\langle A\rangle_N \equiv \lim_{N\to\infty}\frac{(2\pi\hbar)^{-N}}{Z_N}\int \mathrm{d}^N\mathbf{p}\int \mathrm{d}^N\mathbf{q}\,\mathrm{e}^{-\beta_N H_N(\mathbf{p},\mathbf{q})}\,A_N(\mathbf{q}). \tag{2.38}$$

The function $A_N(\mathbf{q})$ is an *estimator*, defined as an average over the beads

$$A_N(\mathbf{q}) = \frac{1}{N}\sum_{l=1}^{N} A(q_l). \tag{2.39}$$

An analogous definition holds if A is a linear function of momentum, $A(p) \propto p$. Again, the nascent thermal average $\langle A\rangle_N$ is the same as a classical thermal average [see Eq. (2.7)] derived from an extended ring-polymer system.

The convergence of Eqs. (2.28) and (2.38) with respect to N (the number of beads) is sufficiently fast that these expressions can be used to simulate many-particle systems that are far beyond the reach of traditional wavefunction-based approaches. Because the path-integral representation is exactly isomorphic with classical statistical mechanics [70], classical methodologies can be applied directly, giving rise to Path-Integral Monte Carlo (PIMC) and Path-Integral Molecular Dynamics (PIMD) [50]. These two methods offer a practical way of computing exact quantum thermal averages, but are only applicable to static properties. No exact quantum–classical isomorphism exists in general for the time-correlation function, and we must therefore rely on approximations.

2.3 Path-integral approximations to quantum dynamics

Although we cannot map exact quantum dynamics onto an extended classical system, it is possible to construct approximations that combine exact quantum statistics with quantum-Boltzmann-conserving classical dynamics. This approach ensures that static thermal averages remain exact and independent of time, and that the approximate TCFs satisfy the detailed balance condition. Such methods can fully account for zero-point energy (ZPE) effects and certain kinds of tunnelling, which is argued to be sufficient for many condensed-matter simulations, where coupling to the environment ensures rapid quantum decoherence [4, 14, 18].

2.3.1 Normal-mode coordinates

Before we begin the discussion of path-integral dynamics approximations, it will be convenient to introduce the so-called "normal-mode" coordinates,

$$\widetilde{Q}_n = \frac{1}{\sqrt{N}} \sum_{l=1}^{N} T_{ln} q_l \quad \Leftrightarrow \quad q_l = \sqrt{N} \sum_{n=-\nu}^{\nu} T_{ln} \widetilde{Q}_n, \tag{2.40}$$

where N is odd,[2] $\nu = (N-1)/2$, and T_{ln} are elements of an orthogonal transformation matrix

$$T_{ln} = \begin{cases} N^{-1/2} & n = 0, \\ \sqrt{2/N}\sin(2\pi ln/N) & n = 1, \ldots, \nu, \\ \sqrt{2/N}\cos(2\pi ln/N) & n = -1, \ldots, -\nu. \end{cases} \tag{2.41}$$

The normalisation by $N^{-1/2}$ in Eq. (2.40) is added to prevent the numerical values of $\widetilde{Q}_n$ from diverging in the limit as $N \to \infty$. With this normalisation, the coordinates scale as $O(N^0)$ and the $n = 0$ component is the ring-polymer centroid

$$\widetilde{Q}_0 = \frac{1}{N} \sum_{l=1}^{N} q_l. \tag{2.42}$$

Such coordinates are frequently referred to as "normal modes" because they diagonalise the ring-polymer spring potential

$$\frac{1}{N} S_N(\mathbf{q}) = \widetilde{S}_N(\widetilde{\mathbf{Q}}) = \sum_{|n|\leq\nu} \frac{m\omega_n^2 \widetilde{Q}_n^2}{2}, \tag{2.43}$$

where

$$\omega_n = 2\omega_N \sin\left(\frac{\pi n}{N}\right). \tag{2.44}$$

Expressed in normal-mode coordinates, the ring-polymer Hamiltonian becomes

$$\frac{1}{N} H_N(\mathbf{p}, \mathbf{q}) = \widetilde{H}_N(\widetilde{\mathbf{P}}, \widetilde{\mathbf{Q}}) = \sum_{|n|\leq\nu} \left\{ \frac{\widetilde{P}_n^2}{2m} + \frac{m\omega_n^2 \widetilde{Q}_n^2}{2} \right\} + \frac{1}{N} \sum_{l=1}^{N} V\left(\sqrt{N} \sum_{|n|\leq\nu} T_{ln} \widetilde{Q}_n \right) \tag{2.45}$$

where the final term is the external potential $\widetilde{V}_N(\widetilde{\mathbf{Q}})$. In the absence of this potential, the coordinates $\widetilde{\mathbf{Q}}$ are precisely the ring-polymer normal modes, with natural frequencies $|\omega_n|$.

[2] For the sake of brevity, we do not extend this to even N, which has been done elsewhere [92].

2.3.2 (Thermostatted) Ring-Polymer Molecular Dynamics

In PIMD, thermal averages of static properties [see Eq. (2.38)] are calculated using the molecular dynamics approach. The ring polymers are equilibrated at an inverse temperature of β_N and propagated according to the classical equations of motion given by Eq. (2.2) with a Hamiltonian $H_N(\mathbf{p}, \mathbf{q})$. A thermostat is often attached to the beads, to ensure proper and efficient sampling of the ring-polymer Boltzmann distribution [92].

Presented in this way, the ring-polymer dynamics is entirely fictitious, serving only as a means to sample the distribution (but see Section 2.3.4). However, it can be shown that interpreting the dynamics literally often produces a reasonable approximation to the exact quantum KTCF,

$$C_{AB}(t) \approx \lim_{N\to\infty} \langle A(0)B(t)\rangle_N \equiv \lim_{N\to\infty} \frac{(2\pi\hbar)^{-N}}{Z_N} \int \mathrm{d}^N\mathbf{p} \int \mathrm{d}^N\mathbf{q}\, \mathrm{e}^{-\beta_N H_N(\mathbf{p},\mathbf{q})}\, A_N(\mathbf{q}) B_N(\mathbf{q}_t), \quad (2.46)$$

where $B_N(\mathbf{q}_t)$ is the estimator evaluated at a time t along the trajectory. This is because the Ring-Polymer Molecular Dynamics (RPMD) approximation satisfies several important criteria [5, 93]:

1. it correctly reduces to the classical TCF in the high-temperature limit;
2. it is exact for static thermal averages and for KTCFs at $t = 0$;
3. it conserves the quantum Boltzmann distribution;
4. it is exact for the harmonic oscillator if either of A or B is linear in position;
5. it is in general a high-order short-time approximation.

Additionally, RPMD transition-state theory (RPMD TST) has been shown to be identical with the exact quantum transition-state theory (QTST) [80], and to bear a close relation to semiclassical instanton rate theory [79]. It is thus routinely applied to calculations of reaction rate constants, including in the deep tunnelling regime [7, 12, 14], and has also been used to study quantum diffusion in liquid hydrogen [8], water [9], and metal lattices [94–96].

One area in which RPMD runs into difficulty is the simulation of vibrational spectra [10]. The fictitious ring-polymer dynamics produces spurious resonances of the centroid $\widetilde{Q}_0$ with the "non-centroid" fluctuation modes, $\widetilde{Q}_{n\neq 0}$. The resonances appear as unphysical peaks in the simulated spectra, and can also interfere with physical features. A partial solution was proposed by Rossi *et al.* [15], who suggested attaching a white-noise Langevin thermostat to

each of the non-centroid modes, thus changing the equations of motion to

$$\frac{\mathrm{d}\widetilde{P}_n}{\mathrm{d}t} = -\frac{\partial V_N(\widetilde{\mathbf{Q}})}{\partial \widetilde{Q}_n} - m\omega_n^2 \widetilde{Q}_n - \gamma_n \widetilde{P}_n + \sqrt{\frac{2m\gamma_n}{\beta}}\xi_n(t) \tag{2.47a}$$

$$\frac{\mathrm{d}\widetilde{Q}_n}{\mathrm{d}t} = \frac{\widetilde{P}_n}{m}. \tag{2.47b}$$

The only change compared to RPMD is the addition of the last two terms in Eq. (2.47a). These involve the friction γ_n and the random noise $\xi_n(t)$, which is an uncorrelated Gaussian process with zero mean and unit variance, i.e. $\langle \xi_n(t) \rangle = 0$ and $\langle \xi_{n_1}(0)\xi_{n_2}(t) \rangle = \delta_{n_1 n_2}\delta(t)$. Note that the coefficient multiplying $\xi_n(t)$ contains a factor of β instead of the β_N that appears in Eq. (16) of Ref. [15]. We have made the change because the equations of motion for bead coordinates $(\mathbf{p}, \mathbf{q})$ with a Hamiltonian $H_N(\mathbf{p}, \mathbf{q})$ and temperature β_N are exactly equivalent to the equations of motion for normal-mode coordinates $(\widetilde{\mathbf{P}}, \widetilde{\mathbf{Q}})$ with a Hamiltonian $\widetilde{H}_N(\widetilde{\mathbf{P}}, \widetilde{\mathbf{Q}})$ and temperature β. The second representation is better suited for our discussion, and so we adopt it from here onwards.

The thermostat dampens the fluctuations of the non-centroid modes, reducing the unphysical artefacts that corrupt the RPMD spectra. Since we do not wish to interfere with the dynamics of the centroid, the centroid friction is set to zero, $\gamma_0 = 0$, although sometimes this may be replaced by a weak global thermostat to improve the sampling (see Chapter 5 and Ref. [16]). The friction parameters of the non-centroid modes are chosen as a compromise between damping the spurious resonances and minimising interference with the vibrational dynamics of the centroid. They are generally defined as

$$\gamma_n = \lambda \times 2|\omega_n|, \tag{2.48}$$

where $2|\omega_n|$ is the friction that minimises the energy decorrelation time of a free ring polymer. Numerical simulation and harmonic analysis suggest that setting $\lambda = 0.5$ gives the optimal result for simulating Thermostatted Ring-Polymer Molecular Dynamics (TRPMD) spectra [15, 83]. This value is used in all of our TRPMD simulations.

Simulated TRPMD spectra generally give accurate positions of the vibrational fundamental bands, although the line shapes are broadened by the interactions with the thermostatted non-centroid modes, especially at low temperatures. Despite this, TRPMD remains the most reliable of the three methods in this chapter, excluding Matsubara dynamics, when applied to spectroscopic simulations. A recent modification by Rossi *et al.* [84, 97] that uses coloured-noise (correlated) thermostatting may further improve this approximation by reducing the

unphysical broadening. The modified approach is discussed further in Chapter 5, where we compare the results from Ref. [84] against our simulated spectra.

2.3.3 Centroid Molecular Dynamics

An alternative approach is to make a mean-field approximation to the exact quantum TCF, which is discussed at length in Chapters 3 and 4. Here we give a brief account of the first successful method to use this kind of approximation. Centroid Molecular Dynamics (CMD), proposed by Cao and Voth [78], approximates quantum TCFs as

$$C_{AB}(t) \approx \frac{(2\pi\hbar)^{-1}}{Z_0} \int \mathrm{d}\widetilde{P}_0 \int \mathrm{d}\widetilde{Q}_0 \, \mathrm{e}^{-\beta[\widetilde{P}_0^2/2m + \mathcal{F}(\widetilde{Q}_0)]} \, A(\widetilde{Q}_0) B(\widetilde{Q}_{0,t}), \tag{2.49}$$

where

$$Z_0 = \frac{1}{2\pi\hbar} \int \mathrm{d}\widetilde{P}_0 \int \mathrm{d}\widetilde{Q}_0 \, \mathrm{e}^{-\beta[\widetilde{P}_0^2/2m + \mathcal{F}(\widetilde{Q}_0)]}. \tag{2.50}$$

The free energy $\mathcal{F}(\widetilde{Q}_0)$ corresponds to the centroid-constrained mean-field force

$$-\frac{\partial \mathcal{F}(\widetilde{Q}_0)}{\partial \widetilde{Q}_0} = \frac{\int \mathrm{d}^N\widetilde{\mathbf{P}}' \int \mathrm{d}^N\widetilde{\mathbf{Q}}' \, \delta(\widetilde{Q}_0' - \widetilde{Q}_0) \, \mathrm{e}^{-\beta \widetilde{H}_N(\widetilde{\mathbf{P}}', \widetilde{\mathbf{Q}}')} \left(-\frac{\partial \widetilde{V}_N(\widetilde{\mathbf{Q}}')}{\partial \widetilde{Q}_0'} \right)}{\int \mathrm{d}^N\widetilde{\mathbf{P}}' \int \mathrm{d}^N\widetilde{\mathbf{Q}}' \, \delta(\widetilde{Q}_0' - \widetilde{Q}_0) \, \mathrm{e}^{-\beta \widetilde{H}_N(\widetilde{\mathbf{P}}', \widetilde{\mathbf{Q}}')}}, \tag{2.51}$$

which gives rise to the CMD equations of motion

$$\frac{\mathrm{d}\widetilde{P}_0}{\mathrm{d}t} = -\frac{\partial \mathcal{F}(\widetilde{Q}_0)}{\partial \widetilde{Q}_0} \qquad \frac{\mathrm{d}\widetilde{Q}_0}{\mathrm{d}t} = \frac{\widetilde{P}_0}{m}. \tag{2.52}$$

The resulting dynamics satisfies the same criteria as listed for (T)RPMD in Section 2.3.2 [78], subject to the caveat that both A and B must be linear in position (or momentum), and therefore only depend on the centroid.

If one or both of the operators are non-linear, CMD has to rely on the additional approximation $A_N(\mathbf{q}) \approx A(\widetilde{Q}_0)$, meaning that the static thermal averages and the $t = 0$ values of the TCFs are no longer exact. However, in the next few chapters we will see that (at least in some cases) this is relatively minor compared to the artefacts produced by the mean-field approximation when it falls outside of its region of validity.

Once again, simulated vibrational spectra provide an instructive example. At high temperatures CMD produces high-quality approximations to exact quantum spectra, both in terms of band positions and line shapes [10, 85]. This includes systems with non-linear dipole moments, where the "static" approximation to the dipole estimator appears to play a very

minor role [17, 20]. In this regime, CMD can be said to outperform its chief competitor, TRPMD.

At lower temperatures the mean-field approximation begins to break down, in what is commonly referred to as the "curvature problem" [85, 86]. This causes the simulated vibrational bands to shift to lower frequencies and eventually broaden, both of which are unphysical artefacts. The curvature problem is discussed in much greater detail in Chapter 3, where we analyse its origins and propose a way to overcome it. For now it suffices to say that the severity of the problem can prevent the use of CMD in spectroscopic simulations of some systems even at room temperature.

2.3.4 Matsubara Dynamics

The path-integral approximations we have so far discussed were originally introduced as heuristic techniques. Despite this, their success implies that there must be an underlying theory that rigorously combines exact quantum Boltzmann statistics with classical dynamics in a way that satisfies the detailed balance condition. This theory, called "Matsubara dynamics", was developed by Althorpe and co-workers [81]. They showed that classical dynamics emerges naturally from the path-integral representation of the exact KTCF when the paths are constrained to be smooth,

$$\widetilde{Q}_n = 0 \quad \text{for} \quad |n| > (M-1)/2 \equiv \mu \quad \text{where} \qquad M \ll N.$$

This condition is equivalent to neglecting the effects of real-time quantum coherence, which is often justified in the condensed phase.

In Chapter 3 we derive Matsubara dynamics in a way that simplifies the original reasoning in Ref. [81] and improves the convergence properties of the corresponding TCFs. At this stage we simply state that, without any further approximations, the smoothness condition gives rise to the Matsubara TCF

$$C_{AB}^{\text{Mats}}(t) = \lim_{M\to\infty} \frac{\alpha_M (2\pi\hbar)^{-1}}{\widetilde{Z}_M} \int \mathrm{d}^M \widetilde{\mathbf{P}}_M \int \mathrm{d}^M \widetilde{\mathbf{Q}}_M \mathrm{e}^{-\beta[\widetilde{H}_M - \mathrm{i}\theta_M]} A_M(\widetilde{\mathbf{Q}}_M) B_M(\widetilde{\mathbf{Q}}_{M,t}). \tag{2.53}$$

Here, the Matsubara Hamiltonian is

$$\widetilde{H}_M(\widetilde{\mathbf{P}}_M, \widetilde{\mathbf{Q}}_M) = \frac{|\widetilde{\mathbf{P}}_M|^2}{2m} + \frac{1}{N}\sum_{l=1}^{N} V\left(\sum_{|n|\le\mu} \sqrt{N} T_{ln} \widetilde{Q}_n\right), \tag{2.54}$$

where $\widetilde{\mathbf{Q}}_M$ are the "smooth" Matsubara positions $\widetilde{Q}_{|n|\leq\mu}$, and $\widetilde{\mathbf{P}}_M$ are the corresponding momenta. The Matsubara phase θ_M is given by

$$\theta_M = \sum_{|n|\leq\mu} \omega_n \widetilde{P}_n \widetilde{Q}_{-n}, \tag{2.55}$$

the function $A_M(\widetilde{\mathbf{Q}}_M)$ is the estimator $A_N(\mathbf{q})$ restricted to the Matsubara subspace,

$$A_M(\widetilde{\mathbf{Q}}_M) = \lim_{N\to\infty} \frac{1}{N} \sum_{l=1}^{N} A\left(\sum_{|n|\leq\mu} \sqrt{N} T_{ln} \widetilde{Q}_n \right), \tag{2.56}$$

with an analogous definition for $B_M(\widetilde{\mathbf{Q}}_M)$. The remaining terms are

$$\alpha_M = \hbar^{(1-M)}[(M-1)/2]!^2 \tag{2.57}$$

and

$$\widetilde{Z}_M = \alpha_M (2\pi\hbar)^{-1} \int \mathrm{d}^M \widetilde{\mathbf{P}}_M \int \mathrm{d}^M \widetilde{\mathbf{Q}}_M \mathrm{e}^{-\beta[\widetilde{H}_M - \mathrm{i}\theta_M]}. \tag{2.58}$$

Crucially, the dynamics of the coordinates $\widetilde{\mathbf{P}}_M$ and $\widetilde{\mathbf{Q}}_M$ is purely classical and conserves the quantum Boltzmann distribution $\mathrm{e}^{-\beta[\widetilde{H}_M - \mathrm{i}\theta_M]}$. In the case when the number of Matsubara modes is $M = 1$, the expression is identical to the classical thermal TCF in Eq. (2.9).

The TCFs calculated according to Eq. (2.53) not only satisfy all of the properties listed in Section 2.3.2, but are also exact for *any* pair of properties A and B in the harmonic limit [81, 83]. Furthermore, it has been shown that CMD, RPMD, and TRPMD are all approximations to Matsubara dynamics [82, 83]. All this, together with supporting numerical calculations, leads us to believe that Matsubara dynamics is the most rigorous way of combining exact quantum statistics with classical dynamics.

The reason for introducing further approximations, as done in CMD and (T)RPMD, is the Matsubara phase θ_M, which gives rise to a sign problem. Because of the phase, the Boltzmann distribution is complex (it is now a *quasi*probability distribution), and the integrand in Eq. (2.53) is highly oscillatory. Such integrals cannot be evaluated using importance sampling unless the system is small enough for a brute-force approach [98, Ch. 4], making Matsubara dynamics too expensive to be used as a practical method [81]. Instead, it is best seen as a theoretical framework, within which one can devise practical path-integral approximations, as we shall see in the next few chapters.

Chapter 3

Mean-field Matsubara dynamics

3.1 Derivation

To obtain a mean-field approximation to the exact Kubo-transformed time-correlation function we start from its path-integral representation,

$$C_{AB}(t) = \lim_{N\to\infty} \frac{(2\pi\hbar)^{-N}}{Z_N} \int \mathrm{d}^N\mathbf{q} \int \mathrm{d}^N\mathbf{p}\, \left[\mathrm{e}^{-\beta\hat{H}}\right]_{\overline{N}}(\mathbf{p},\mathbf{q})\, A_N(\mathbf{q})\, \mathrm{e}^{\hat{L}_N t} B_N(\mathbf{q}), \tag{3.1}$$

derived in Appendices A.1 and A.2. The generalised Wigner transform $[\mathrm{e}^{-\beta\hat{H}}]_{\overline{N}}$ and the path-integral Liouvillian $\hat{L}_N$ are defined in Eqs. (A.14) and (A.22) respectively. Following Hele *et al.* [81], we refer to the long-established result that quantum thermal averages of static properties can be calculated exactly while only using smooth Feynman paths [99, 100]. Hence we restrict the estimators A_N and B_N to the subspace of smooth normal-mode coordinates (see Section 2.3.1), suppressing their dependence on $\{\widetilde{Q}_n,\ |n| > (M-1)/2\}$, where $M \ll N$, so that

$$A_N(\mathbf{q}),\ B_N(\mathbf{q}) \xrightarrow[M\ll N]{N\to\infty} A_M(\widetilde{\mathbf{Q}}_M),\ B_M(\widetilde{\mathbf{Q}}_M)$$

with

$$A_M(\widetilde{\mathbf{Q}}_M) = \lim_{N\to\infty} \frac{1}{N} \sum_{l=1}^{N} A\left(\sum_{|n|\le\mu} \sqrt{N} T_{ln} \widetilde{Q}_n \right), \tag{3.2}$$

and $\mu \equiv (M-1)/2$ for odd M. To make an analogy with a discrete Fourier transform, this is equivalent to applying a low-pass filter to a discretised Feynman path. The frequencies of the

remaining smooth modes tend to the bosonic Matsubara frequencies [101]

$$\lim_{\frac{n}{N}\to 0} \omega_n = \frac{2\pi n}{\beta\hbar} \equiv \widetilde{\omega}_n, \tag{3.3}$$

which is why $\widetilde{\mathbf{Q}}_M$ are referred to as the "Matsubara modes". Using the smoothed estimators in Eq. (3.2), the value of $C_{AB}(0)$ remains exact as $M \to \infty$, and so no approximation is made to the quantum statistics.

Now we introduce the *only* approximation that we apply to the quantum dynamics, which is to replace the exact Liouvillian with its mean-field average,

$$\hat{L}_{\mathrm{MF}}(\widetilde{\mathbf{P}}_M, \widetilde{\mathbf{Q}}_M) = \lim_{N\to\infty} \frac{\int \mathrm{d}^N\mathbf{p} \int \mathrm{d}^N\mathbf{q} \left[\mathrm{e}^{-\beta\hat{H}}\right]_{\overline{N}} \delta(\mathbf{q}, \widetilde{\mathbf{Q}}_M)\, \delta(\mathbf{p}, \widetilde{\mathbf{P}}_M)\, \hat{L}_N(\mathbf{p}, \mathbf{q})}{\int \mathrm{d}^N\mathbf{p} \int \mathrm{d}^N\mathbf{q} \left[\mathrm{e}^{-\beta\hat{H}}\right]_{\overline{N}} \delta(\mathbf{q}, \widetilde{\mathbf{Q}}_M)\, \delta(\mathbf{p}, \widetilde{\mathbf{P}}_M)}, \tag{3.4}$$

where $\delta(\mathbf{q}, \widetilde{\mathbf{Q}}_M)$ constrains the smooth components of the path at $\widetilde{\mathbf{Q}}_M$, as defined in Eq. (A.36). In terms of the Matsubara modes, the exact Liouvillian is

$$\lim_{N\to\infty} \hat{L}_N = \mathcal{L}_M + \lim_{N\to\infty} \hat{L}_{N,M}, \tag{3.5}$$

where

$$\mathcal{L}_M = \lim_{N\to\infty} \left[\frac{1}{m} \widetilde{\mathbf{P}}_M \cdot \boldsymbol{\nabla}_{\widetilde{\mathbf{Q}}_M} - \widetilde{V}_N(\widetilde{\mathbf{Q}}) \frac{2N}{\hbar} \sin\left(\frac{\hbar}{2N} \overleftarrow{\boldsymbol{\nabla}}_{\widetilde{\mathbf{Q}}_M} \cdot \overrightarrow{\boldsymbol{\nabla}}_{\widetilde{\mathbf{P}}_M} \right) \right]. \tag{3.6}$$

The arrows over the gradient operators indicate the direction in which they act. $\mathcal{L}_M$ contains all the derivatives involving only the modes with indices $|n| \leq \mu$, and $\hat{L}_{N,M}$ contains the remaining terms. We can get an explicit expression for $\hat{L}_{N,M}$ [81], but this isn't necessary since the expression vanishes under mean-fielding. In addition, if we choose our Matsubara modes so that $(M^3/N^2) \to 0$ as $N \to \infty$ [88], $\mathcal{L}_M$ reduces to the classical Liouvillian,

$$\mathcal{L}_M = \lim_{N\to\infty} \left[\frac{1}{m} \widetilde{\mathbf{P}}_M \cdot \boldsymbol{\nabla}_{\widetilde{\mathbf{Q}}_M} - \boldsymbol{\nabla}_{\widetilde{\mathbf{Q}}_M} \widetilde{V}_N(\mathbf{q}) \cdot \boldsymbol{\nabla}_{\widetilde{\mathbf{P}}_M} \right]. \tag{3.7}$$

On calculating its mean-field average (see Appendix A.3), we get

$$\hat{L}_{\mathrm{MF}}(\widetilde{\mathbf{P}}_M, \widetilde{\mathbf{Q}}_M) = \sum_{|n|\leq\mu} \frac{\widetilde{P}_n}{m} \frac{\partial}{\partial \widetilde{Q}_n} - \frac{\partial \mathcal{F}_M(\widetilde{\mathbf{Q}}_M)}{\partial \widetilde{Q}_n} \frac{\partial}{\partial \widetilde{P}_n}, \tag{3.8}$$

where

$$\mathrm{e}^{-\beta\mathcal{F}_M(\widetilde{\mathbf{Q}}_M)} = \left(\frac{m}{2\pi\beta_N\hbar^2}\right)^{(N-M)/2} N^{M/2}\int \mathrm{d}^N\mathbf{q}\,\delta(\mathbf{q},\widetilde{\mathbf{Q}}_M)\,\mathrm{e}^{-\beta[W_N(\mathbf{q})-\widetilde{S}_M(\widetilde{\mathbf{Q}}_M)]}, \tag{3.9}$$

$$\widetilde{S}_M(\widetilde{\mathbf{Q}}_M) = \sum_{|n|\leq\mu}\frac{m\widetilde{\omega}_n^2\widetilde{Q}_n^2}{2}, \tag{3.10}$$

and

$$W_N(\mathbf{q}) = \frac{1}{N}\sum_{l=1}^{N}\left[V(q_l)+\frac{m\omega_N^2}{2}(q_{l+1}-q_l)^2\right]. \tag{3.11}$$

The exact KTCF is therefore approximated by

$$\widetilde{C}_{AB}^{[M]}(t) = \frac{(2\pi\hbar)^{-M}}{Z_M}\int \mathrm{d}^M\widetilde{\mathbf{Q}}_M\int \mathrm{d}^M\widetilde{\mathbf{P}}_M\,\mathrm{e}^{-\beta[\mathcal{H}_M-\mathrm{i}\theta_M]}A_M(\widetilde{\mathbf{Q}}_M)\mathrm{e}^{\hat{L}_{\mathrm{MF}}t}B_M(\widetilde{\mathbf{Q}}_M), \tag{3.12}$$

where

$$\mathcal{H}_M = \frac{|\widetilde{\mathbf{P}}_M|^2}{2m}+\mathcal{F}_M(\widetilde{\mathbf{Q}}_M) \tag{3.13}$$

is the mean-field Hamiltonian,

$$\theta_M = \sum_{|n|\leq\mu}\widetilde{\omega}_n\widetilde{P}_n\widetilde{Q}_{-n} \tag{3.14}$$

is the Matsubara phase, and the partition function Z_M is defined in Eq. (3.17). The Liouvillian can be expressed as the Poisson bracket

$$\hat{L}_{\mathrm{MF}}(\widetilde{\mathbf{P}}_M,\widetilde{\mathbf{Q}}_M) = \{\,\cdot\,,\mathcal{H}_M\}, \tag{3.15}$$

showing that the mean-field Hamiltonian is conserved. Furthermore, the same argument as in the original formulation [81] shows that the Matsubara phase θ_M is also conserved by the dynamics. Therefore Eq. (3.12) conserves the MF Matsubara quasiprobability distribution.

The only difference between our formulation and the original derivation in Ref. [81] is the step that takes Eq. (3.7) to Eq. (3.8). Whereas we make no further approximations, the original approach truncates the dependence of the external potential on the non-Matsubara modes,

$$\widetilde{V}_N(\widetilde{\mathbf{Q}}) \to \widetilde{V}_M(\widetilde{\mathbf{Q}}_M) \equiv \frac{1}{N}\sum_{l=1}^{N}\left(\sum_{|n|\leq\mu}\sqrt{N}T_{ln}\widetilde{Q}_n\right). \tag{3.16}$$

On the one hand, this allows the integration in Eq. (3.9) to be done analytically, giving a "truncated" Matsubara potential in closed form. On the other hand, this approximation means

that the truncated Matsubara partition function, static thermal averages, and $t = 0$ values of the TCFs are only exact in the limit as $M \to \infty$. In contrast, the MF Matsubara partition function,

$$Z = Z_M = \frac{1}{(2\pi\hbar)^M} \int \mathrm{d}^M \widetilde{\mathbf{Q}}_M \int \mathrm{d}^M \widetilde{\mathbf{P}}_M \, \mathrm{e}^{-\beta[\mathcal{H}_M - \mathrm{i}\theta_M]}, \tag{3.17}$$

is exact for any choice of M, as are the static thermal averages and $t = 0$ values of TCFs involving linear operators.

The case of $M = 1$ is special because it does not have a phase. At this point MF Matsubara dynamics reduces to CMD, which can be viewed as the first rung of a ladder of approximations that in the limit as $M \to \infty$ tend to the most general quantum-Boltzmann-conserving classical dynamics. Given that CMD typically approximates exact quantum TCFs better than classical dynamics, we hope that MF Matsubara dynamics will generally be a better approximation than the original "truncated" Matsubara dynamics for the same number of modes M. In the rest of this chapter we report on the numerical simulations that test this idea for a one-dimensional quartic potential and a two-dimensional model of an OH bond.

3.2 The one-dimensional quartic potential

In this section we consider the quartic potential $V(q) = q^4/4$, a popular one-dimensional test system that is particularly demanding of approximate dynamics methods due to its high levels of quantum coherence.

3.2.1 Numerical results

To assess the performance of MF Matsubara dynamics we calculate the position ACF ($\hat{A} = \hat{B} = \hat{q}$) at $\beta = 1$ and $\beta = 8$. We work in reduced units throughout, so that $m = 1$ and $\hbar = 1$. The exact reference TCFs are calculated by solving the time-independent Schrödinger equation in the discrete variable representation due to Colbert and Miller [25]. We compare these against the results from four approximate methods: classical dynamics, truncated Matsubara dynamics ($M = 3$), CMD, and MF Matsubara dynamics ($M = 3$).

All four methods rely on the standard velocity Verlet algorithm to integrate the equations of motion, and use a local Langevin thermostat [92, 102] with friction $\gamma_0 = 1.0$ a.u. to ensure proper sampling during the thermalisation. The forces for three-mode Matsubara dynamics

are derived from the analytical $M = 3$ Matsubara potential,[1]

$$\widetilde{V}_M(\widetilde{Q}_0, r_1) = \frac{1}{4}\widetilde{Q}_0^4 + \frac{3}{2}\widetilde{Q}_0^2 r_1^2 + \frac{3}{8}r_1^4, \tag{3.18}$$

where

$$r_1 = \sqrt{\widetilde{Q}_1^2 + \widetilde{Q}_{-1}^2}. \tag{3.19}$$

The mean-field forces for CMD and MF Matsubara dynamics [MF(3)] are approximated with interpolating cubic splines [98]. The imaginary-time translation symmetry of the MF Matsubara potential means that a two-dimensional grid in Q_0 and r_1 is sufficient for the MF(3) calculations. We refer the reader to Appendix A.6 for further simulation details.

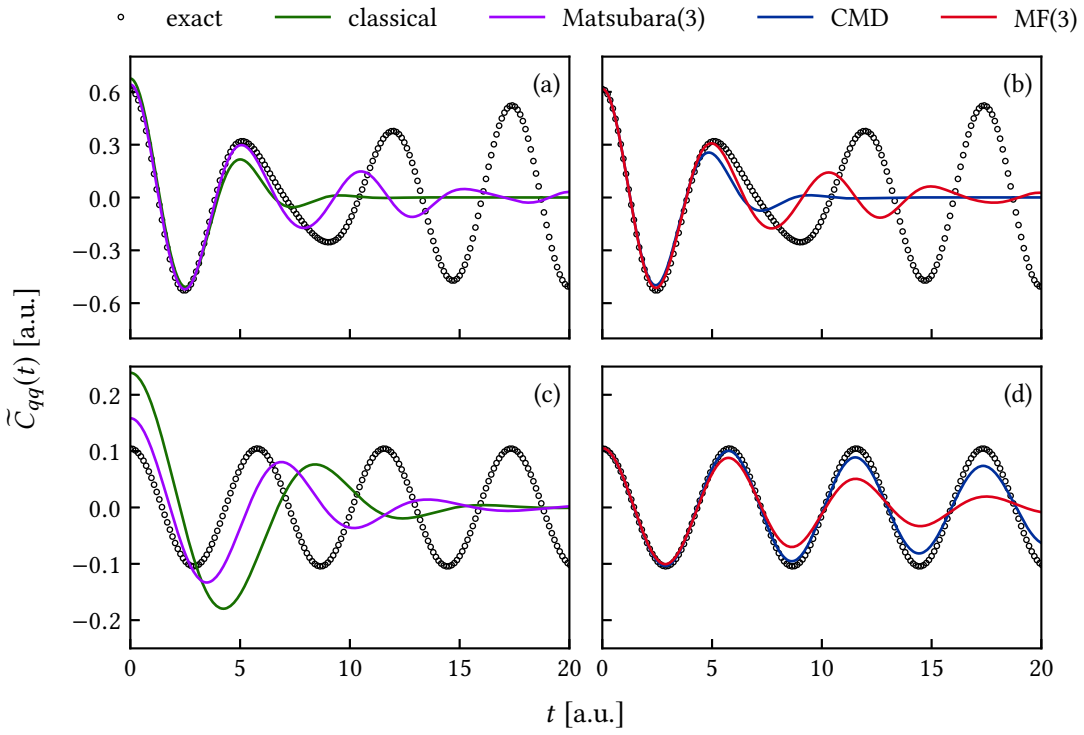

Figure 3.1 Kubo-transformed position ACFs for the quartic oscillator $V(q) = q^4/4$ at $\beta = 1$ (top) and $\beta = 8$ (bottom). Panels (a) and (c) compare "truncated" Matsubara dynamics to the exact quantum results, and panels (b) and (d) compare MF Matsubara dynamics to the same set of results. The number in parentheses refers to the number of Matsubara modes. Note that one-mode truncated Matsubara dynamics is equivalent to classical dynamics, whereas one-mode MF Matsubara dynamics is equivalent to CMD.

[1] See supplementary material for Ref. [81].

The results of our calculations are shown in Figure 3.1, where the top two panels show the high-temperature regime ($\beta = 1$), and the bottom two panels show the low-temperature regime ($\beta = 8$). At $\beta = 1$ there is little difference between the "truncated" approximations in panel (a) and the mean-field approximations in panel (b). This is because at $\beta = 1$ the first Matsubara frequency ($\widetilde{\omega}_1 = 2\pi$ a.u.) is significantly higher than the natural oscillation frequency of ~ 1 a.u. Hence the mean-fielded modes are nearly harmonic (the spring term in Eq. (3.11) dominates the potential energy term) and do not contribute much to the free energy $\mathcal{F}_M(\widetilde{\mathbf{Q}}_M)$. On the other hand, at $\beta = 8$ there is a significant difference between the two sets of results (panels (c) and (d) of Figure 3.1). The first Matsubara frequency is now of the same magnitude as the natural oscillation frequency, and the corresponding normal modes must make a considerable contribution to the free energy $\mathcal{F}_M(\widetilde{\mathbf{Q}}_M)$, creating noticeable deviations from the truncated potential $\widetilde{V}_M(\widetilde{\mathbf{Q}}_M)$.

Unsurprisingly, none of the approximations reproduce the long-time behaviour of the quantum TCF, which keeps oscillating indefinitely due to quantum coherence. The latter can be described as the interference between forward–backward paths in the path-integral representation of the quantum TCF [66]. All of the approximations considered in this work set the difference between such paths to zero, explicitly neglecting real-time quantum coherence. Despite this, the CMD results for this potential become a better approximation to the exact TCF as the temperature is decreased. This feature, first explained by Ramírez and López-Ciudad [103], arises whenever the thermal energy is small compared to the separation between the ground state energy E_0 and the first excited state E_1. In this regime, the CMD potential becomes increasingly harmonic, with a frequency approaching the correct quantum limit of $(E_1 - E_0)/\hbar$ [88]. Hence CMD TCFs of linear operators tend to the exact result as $\beta \to \infty$.

Overall our calculations confirm that truncated and MF Matsubara dynamics produce similar results when the harmonic frequencies of the mean-fielded modes $\omega_{|n|>\mu}$ exceed the "physical" oscillation frequency of the potential $V(q)$. We also see that when this condition is not met, the mean-field approach gives a better approximation than its truncated counterpart with the same number of modes. Further analysis is complicated by the Ramírez oscillations, which lead to uncharacteristically good agreement between the CMD TCF and the exact quantum result at low temperatures. Such behaviour should not be expected in condensed-phase systems, which have closely spaced energy levels and never reach the Ramírez limit, $k_\mathrm{B}T \ll (E_1 - E_0)$, in practical simulations. To get a more realistic picture we must consider a higher-dimensional potential. This requires a way to calculate mean-field forces on the fly, as grid-based calculations are unfeasible for $M > 1$ beyond one-dimensional potentials due to the exponential scaling of the grid size with system dimensionality.

3.2.2 Adiabatic implementation

Single-mode ($M = 1$) MF Matsubara dynamics reduces to CMD, for which there is a well-established way of calculating mean-field forces on the fly, known as Adiabatic Centroid Molecular Dynamics (ACMD) [10, 104]. ACMD approximates the mean-field forces on the centroid by making the non-centroid modes move on a faster timescale. This is achieved by shifting them to an adiabatic frequency Ω and scaling the corresponding masses,

$$\omega_n \to \Omega, \qquad m \to m(\omega_n/\Omega)^2. \tag{3.20}$$

To ensure ergodicity, the non-centroid modes are additionally subjected to thermostatting. As the separation of timescales increases in the limit $\Omega \to \infty$, the time averages of the instantaneous forces on the centroid tend to the true mean-field averages, and the dynamics of the centroid becomes equivalent to CMD [104]. This comes at the cost of having to use a smaller time step for the numerical propagation to remain stable. In practice, convergence is reached at relatively small values of Ω (see e.g. Ref. [10]), making ACMD a practical method.

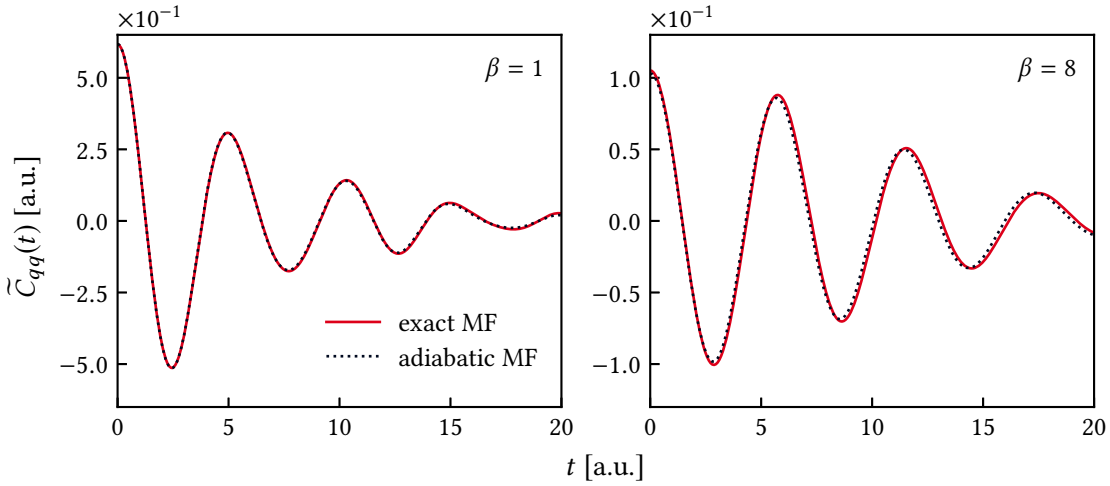

Figure 3.2 MF Matsubara ($M = 3$) position ACFs for the quartic potential $V(q) = q^4/4$ calculated using interpolated forces ("exact MF") and on-the-fly forces yielded by the adiabatic algorithm ("adiabatic MF"). The two sets of results are in close agreement at both temperatures ($\beta = 1$, $N = 16$ and $\beta = 8$, $N = 64$) for an adiabatic frequency $\Omega = 4N^{N/(N-1)}/\beta\hbar$.

A similar approach should work for MF Matsubara dynamics with $M > 1$. The only reservation is that at small adiabatic frequencies Ω the Matsubara phase θ_M is not conserved on the decorrelation timescale of the TCF. This could mean that to converge the dynamics, impractically large values of Ω have to be used. In our simulations we find that this is not the

case. Figure 3.2 compares the Matsubara TCFs calculated using interpolated ("exact MF") and on-the-fly ("adiabatic MF") forces. We chose the adiabatic frequency according to a modified prescription due to Habershon *et al.* [10],

$$\Omega = 4 \times N^{N/(N-1)}/\beta\hbar, \tag{3.21}$$

where the factor of 4 had to be introduced in order to reach satisfactory agreement with the reference TCFs. Further simulation details can be found in Appendix A.6. While considerable, the adiabatic frequency is not so large as to be prohibitively expensive, so we can hope to converge at least some MF Matsubara TCFs for the two-dimensional system in the following section.

3.3 The two-dimensional Morse potential

We consider a two-dimensional "champagne-bottle" model of a vibrating, rotating OH bond similar to that used in Ref. [85]. The radial polar coordinate r represents the OH bond length and the polar angle θ represents rotation in the plane. The potential is taken to be a Morse function

$$V(r) = D_0\left[1 - \mathrm{e}^{-\alpha(r-r_{\mathrm{eq}})}\right]^2 \tag{3.22}$$

with $r_{\mathrm{eq}} = 1.8324$, $D_0 = 0.18748$ and $\alpha = 1.1605$ a.u.; the reduced mass is set to $m = 1741.05$ a.u. In what follows we compare various path-integral approximations to the vibrational density of states (also called the power spectrum), which can be obtained from the position ACF [9],

$$N(\omega) = \omega^2 \int_{-\infty}^{\infty} \mathrm{d}t\, \mathrm{e}^{-\mathrm{i}\omega t} C_{\mathbf{q}\cdot\mathbf{q}}(t) f(t), \tag{3.23}$$

or the velocity ACF[2]

$$N(\omega) = \int_{-\infty}^{\infty} \mathrm{d}t\, \mathrm{e}^{-\mathrm{i}\omega t} C_{\mathbf{v}\cdot\mathbf{v}}(t) f(t). \tag{3.24}$$

The factor $f(t)$ is a window function that dampens the tail of the TCF, reducing ringing artefacts due to imperfect convergence. When applied to the exact quantum TCF, $f(t)$ serves the additional purpose of removing the recurrences caused by real-time quantum coherence. In our two-dimensional model, the recurrences are well separated from the initial decay of

[2] See supplementary material for Ref. [16].

the TCF, suggesting a sensible choice for $f(t)$ to be a sigmoid window with a sharp cut-off,

$$f(t) = \frac{1}{1 + \mathrm{e}^{(|t|-t_{1/2})/w}}, \tag{3.25}$$

with $t_{1/2} = 400$ fs and $w = 25$ fs. We refer to Appendix A.6 for further details on how the exact reference spectra were calculated.

We choose to focus on the power spectrum because it derives from a linear function of position.[3] The exact estimators $A_M(\widetilde{\mathbf{Q}}_M) = B_M(\widetilde{\mathbf{Q}}_M) = \widetilde{\mathbf{Q}}_0$ can therefore be used for any choice of M, allowing us to focus on the approximations made to the dynamics, without having to also consider the approximations made to the statistics. We calculate the power spectrum instead of directly comparing the TCFs because the differences between the various approximations are seen more clearly in the frequency domain. Additionally, the power spectrum is proportional to the infrared absorption spectrum of a linear dipole moment $\boldsymbol{\mu} \propto \mathbf{q}$, giving further physical meaning to our results.

3.3.1 Convergence of mean-field Matsubara dynamics calculations

Before we compare MF Matsubara dynamics to other approximations, we need to determine the adiabatic separation that produces sufficiently accurate mean-field forces. We define the adiabatic frequency differently to Eq. (3.21), setting

$$\omega_n \longrightarrow \Omega = \frac{\gamma N}{\beta\hbar} \qquad m \longrightarrow m_n = m\left(\frac{\beta\hbar\omega_n}{\gamma N}\right)^2, \tag{3.26}$$

where γ is the "adiabaticity parameter". Otherwise, we follow the procedure outlined in Section 3.2.2. The convergence study is conducted for $T = 200$ K, where the Matsubara sign problem is mild enough to yield converged TCFs after relatively few sample trajectories. The resulting spectra are plotted in Figure 3.3, illustrating the convergences of MF Matsubara dynamics ($M = 3$, $N = 32$) with respect to the adiabaticity parameter.

As seen from the figure, the rotational peak at 200 cm^{-1} and the vibrational fundamental at 3600 cm^{-1} converge quickly with respect to the adiabatic separation. The only major changes with increasing γ are the "wiggles" at around 700 and 3000 cm^{-1}. These are artefacts due incomplete convergence with respect to M that are also present in truncated Matsubara spectra and are not due to under-sampling. The spurious wiggles at 3000 cm^{-1} disappear if the fluctuations about the centroid $\widetilde{\mathbf{Q}}_0$ are approximated by local normal modes (see Appendix A.4),

[3] Equivalently, a linear function of momentum, with $A_M(\widetilde{\mathbf{Q}}_M) = B_M(\widetilde{\mathbf{Q}}_M) = \widetilde{P}_0/m$.

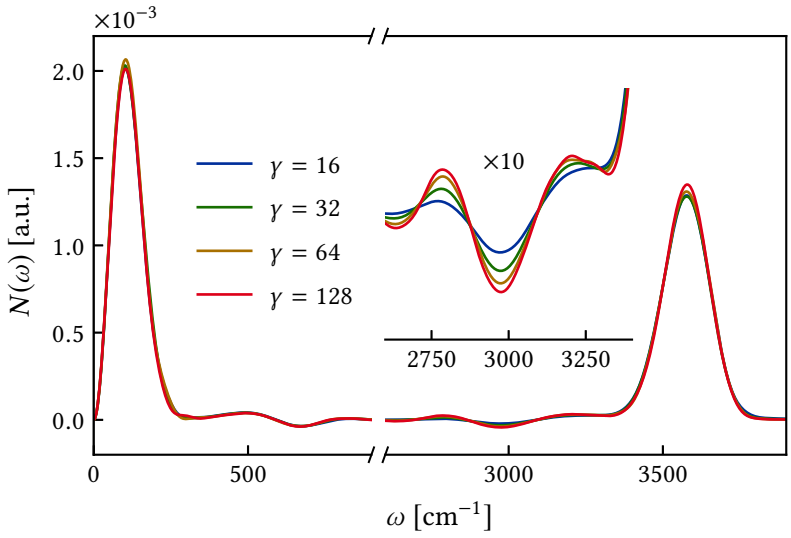

Figure 3.3 Vibrational power spectra for the two-dimensional Morse potential in Eq. (3.22), calculated with three-mode adiabatic MF Matsubara dynamics at $T = 200$ K, using $N = 32$ ring-polymer beads. The plot illustrates convergence with respect to the adiabaticity parameter γ, with key features at 200 and 3600 cm^{-1} already converged at $\gamma = 16$. The features at 700 cm^{-1} and 3000 cm^{-1}, which take longer to converge, are known artefacts and are not important for subsequent analysis.

suggesting that they are caused by rotation–vibration coupling. The wiggles at 700 cm^{-1} probably arise from the way that the elliptical ($M = 3$) Matsubara loops scatter off the curved potential energy surface, and would disappear in the limit $M \to \infty$ or if we used curvilinear rather than Cartesian coordinates (see Chapter 4).

Based on these results, we conclude that an adiabatic separation of $\gamma = 32$ is sufficient to get converged Matsubara spectra. The sign problem prevents us from further increasing M to ascertain the convergence of the spectra with respect to the number of Matsubara modes, but we can draw some conclusions from the temperature dependence of the spectral features in Figure 3.4. On the left, in colour, are shown the MF Matsubara spectra calculated at 300–600 K for $M = 3$ and at 200 K for $M = 5$. These are the highest values of M that it was possible to converge. The grey dashed lines show the mean-field spectra for 600 K, $M = 1$ (more intense), and 200 K, $M = 3$ (less intense). On the right are the results from the analogous truncated Matsubara simulations.

The two sets of results show qualitatively different behaviour. Three-mode MF Matsubara dynamics produces vibrational fundamentals with the same maximum absorption frequency until the temperature drops to 200 K. At this point the three-mode result is shifted to the red; increasing the number of modes to $M = 5$ causes the absorption maximum to move back

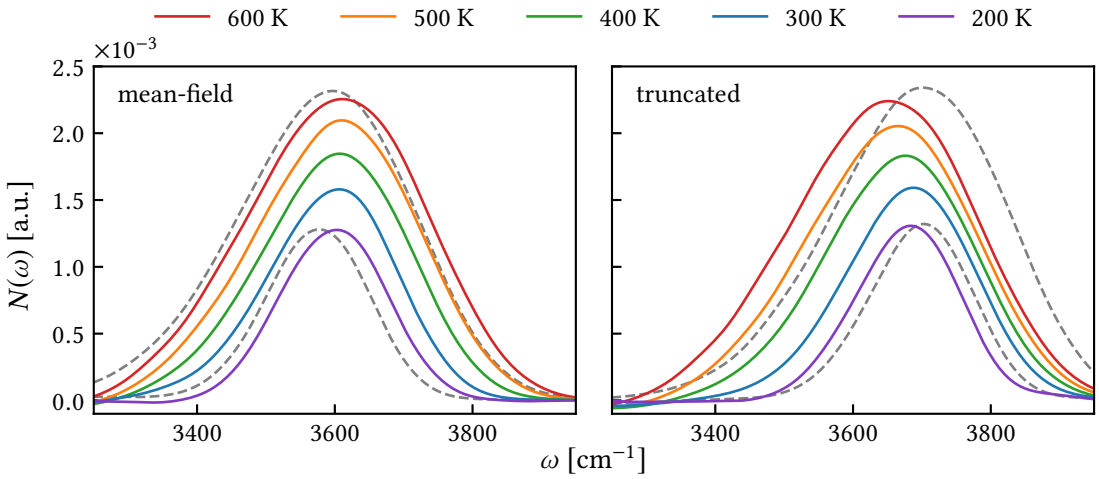

Figure 3.4 Vibrational power spectra for the two-dimensional Morse potential in Eq. (3.22), calculated with adiabatic MF Matsubara dynamics (left) and truncated Matsubara dynamics (right) at temperatures between 200 and 600 K. The coloured solid lines were calculated using $M = 5$ at $T = 200\ K$, and $M = 3$ at $T \geq 300\ K$. The two intense dashed peaks in grey are for $T = 600$ K, $M = 1$. The other two dashed peaks are for $T = 200$ K, $M = 3$.

into alignment with the high-temperature results.[4] In contrast, the truncated three-mode Matsubara spectra steadily shift to the blue as the temperature is lowered, mirroring classical simulations. Given that thermal energy is small compared to vibrational excitation energy, we expect a temperature-independent absorption maximum, and MF Matsubara dynamics is in line with this expectation. We take this as an indication that our mean-field dynamics results are essentially converged with respect to M, unlike their truncated counterparts.

3.3.2 Comparison of path-integral approximations

In the top panel of Figure 3.5 we show the exact power spectra for the two-dimensional Morse potential, calculated for temperatures between 200 and 800 K using the DVR due to Colbert and Miller [25]. In this temperature range the thermal energy $k_B T$ is much smaller than the separation between the vibrational energy levels, and so we expect the only vibrational transition to be from the ground state to the first excited state. This is indeed the case, with the stretch fundamental showing a temperature-independent maximum at 3588(1) cm^{-1}.

The bottom three panels show the various approximations to the exact quantum spectra, calculated using different path-integral methods. In the second panel we show the results of mean-field Matsubara dynamics simulations, where the spectra at 200, 400, and 600 K are

[4] The maxima are at 3603, 3606, 3608, 3610, and 3611 cm^{-1} at 200–600 K.

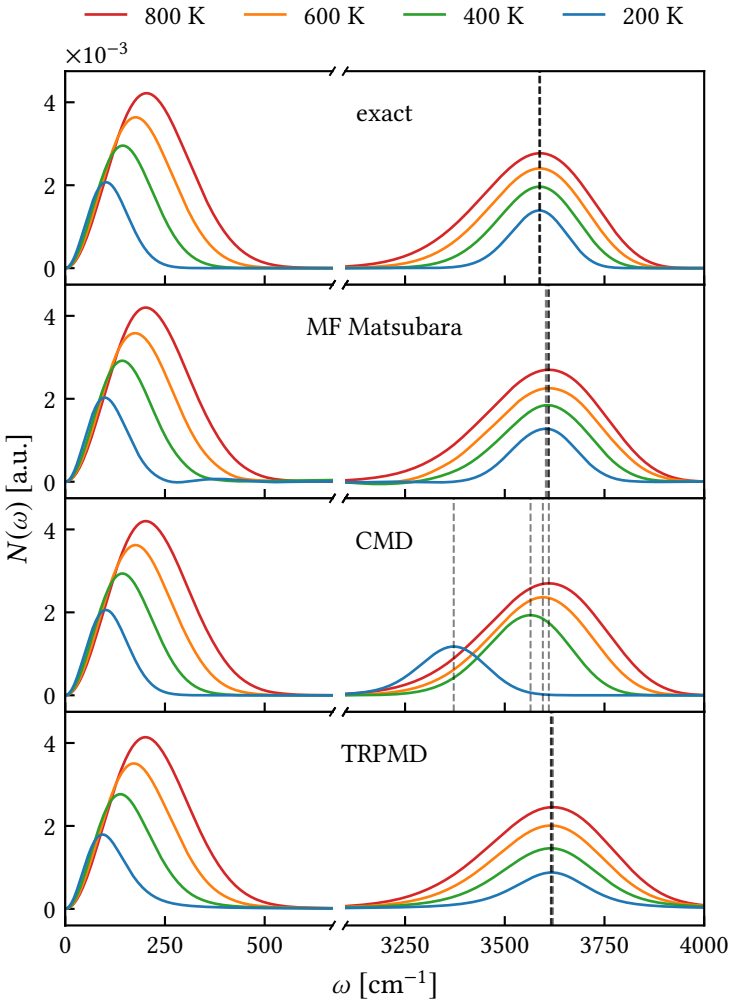

Figure 3.5 Exact power spectra for the champagne-bottle Morse potential in Eq. (3.22), compared with the results of MF Matsubara dynamics, CMD, and TRPMD simulations. The MF Matsubara spectra were calculated using $M = 1$, 3, 3, and 5 modes at 800, 600, 400, and 200 K respectively. The dashed grey lines indicate the positions of the absorption maxima for the stretch band. Note the temperature-independent absorption maxima of the Matsubara and TRPMD peaks, and the CMD redshift that grows rapidly on decreasing the temperature from 400 to 200 K.

the same as in Section 3.3.1 ($M = 5$, $M = 3$ and $M = 3$ respectively), and the spectrum at 800 K is from a CMD calculation ($M = 1$), which at this temperature is likely close to the converged Matsubara result. Even with the convergence artefacts discussed in Section 3.3.1, the Matsubara results in Figure 3.5 are in strikingly good agreement with the exact quantum results across the entire 200–800 K range. Most importantly, the Matsubara vibrational peak positions are correctly independent of temperature. The only difference is a 22 cm^{-1} blueshift, which remains constant to within the sampling error,[5] and a broadening of the vibrational line shapes, which in part could be due to incomplete adiabatic separation, as suggested by the comparison of the (adiabatic) MF Matsubara and (grid-based) CMD results at $T \geq 400$ K.

[5]The blueshifts are 22, 22, 20, and 17 cm^{-1} at 800, 600, 400, and 200 K, with a 4 cm^{-1} error bar at 200 K.

In the third panel we show the CMD spectra, which suffer from the well-known "curvature problem" [85, 86], whereby the CMD vibrational peak shifts to the red as the temperature is decreased. Two aspects of this behaviour are worth pointing out. First, as discussed previously, the CMD peak at 800 K aligns with the Matsubara results at lower temperatures and is in very close agreement with the exact quantum peak, except for the 22 cm^{-1} blueshift and a slight broadening. For comparison, the classical peak at this temperature (not shown) is blueshifted by about 105 cm^{-1} on account of zero-point energy violation, and is similarly broadened. Second, the redshifting of the CMD peak increases gradually down to about 250 K, and the line shape scarcely changes; below 250 K, the redshift increases dramatically (to 215 cm^{-1}at 200 K), and the line shape broadens noticeably. We return to these two points in the next section.

In the last panel of Figure 3.5 we show the spectra calculated using TRPMD with a PILE thermostat (friction parameter $\lambda = 0.5$). As expected, TRPMD does very well in predicting the position of the absorption maximum, which is correctly temperature-independent and blueshifted relative to the exact quantum result by about 28 cm^{-1}. Unlike in the Matsubara spectra, the TRPMD peaks are significantly broadened, especially at the lower temperatures. This effect is well-known and caused by the coupling of the centroid to the strongly thermostatted non-centroid modes. We believe that the additional blueshift is also due to the thermostat. In Chapter 5 we will see that both these effects are mitigated in coloured-noise TRPMD proposed by Rossi *et al.* [84].

In summary, Matsubara dynamics spectra closely approximate the exact quantum result. If we rule out the possibility of a long convergence tail in M changing the position of the vibrational peak, the 22 cm^{-1} redshift and the slight narrowing of the quantum vibrational peak are the only significant quantum coherence effects. Based on the position of this peak, we can also infer that CMD agrees closely with Matsubara dynamics at 800 K, and gives a reasonable approximation down to about 250 K. In this temperature range, the CMD redshifts are small and can be corrected by releasing the $|n| = 1$ Matsubara modes from the mean field. Below 250 K, the CMD redshift increases dramatically, with $|n| = 2$ modes required to correct the redshift at 200 K. Further calculations (not shown) suggest that many more modes would be required at lower temperatures. This parallel between the curvature problem in CMD and the number of modes required to converge Matsubara dynamics is very suggestive and prompts further investigation.

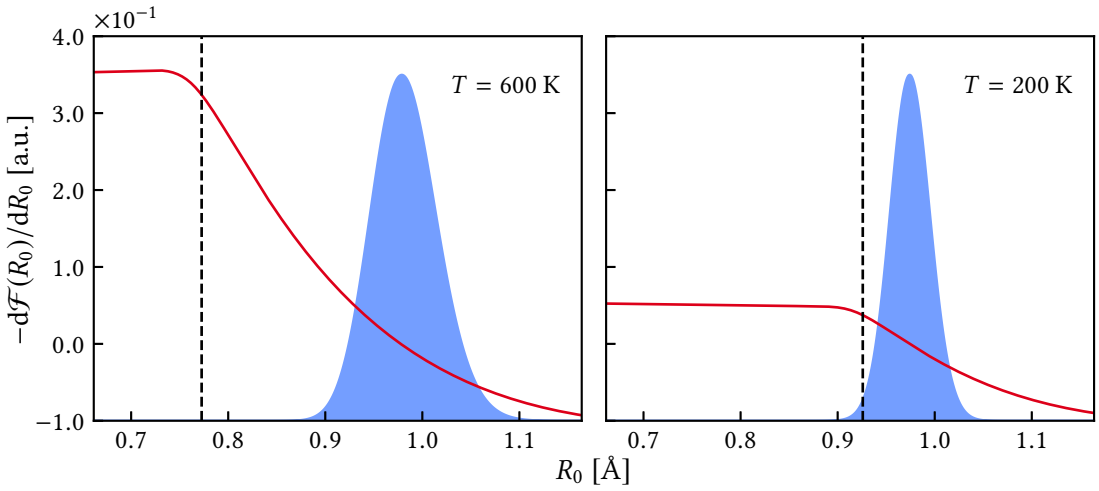

Figure 3.6 The CMD mean-field force $-\mathrm{d}\mathcal{F}(R_0)/\mathrm{d}R_0$ (red line) plotted on top of the corresponding radial distribution function $\propto R_0 e^{-\beta\mathcal{F}(R_0)}$ (shaded blue). The dotted vertical lines indicate the position of the critical radius R_c given by Eq. (3.27). Note that R_c coincides with the onset of the flattening of the force, and that the Boltzmann distribution overlaps R_c at 200 K.

3.3.3 Analysis of the curvature problem in CMD

To investigate why CMD breaks down rapidly below 250 K, we plot in Figure 3.6 the centroid mean-field force $-\mathrm{d}\mathcal{F}/\mathrm{d}R_0$, $R_0 = \sqrt{\widetilde{X}_0^2 + \widetilde{Y}_0^2}$, at 600 and 200 K, and overlay this with the CMD radial distribution function (RDF). As has been noted previously [85, 86], the force flattens for R_0 below a certain radius, and this radius increases as the temperature decreases. Figure 3.6 shows clearly why CMD breaks down below about 250 K: at 600 K the quantum Boltzmann distribution is well separated from the flat region, but at 200 K the distribution starts to overlap it.

It is easy to identify the origin of the flattening. Figure 3.7 shows the centroid-constrained ring-polymer distribution at three points along a single trajectory at 600 and 200 K. The 200 K trajectory is one of the 6% of trajectories that make it into the flat region at this temperature. During the 600 K trajectory, the distribution moves as a relatively compact "blob", stretching slightly at the inner turning point as it pushes against the repulsive wall; the minimum-energy ring polymer within the distribution is collapsed onto a point at the centroid. During the 200 K trajectory, by contrast, the distribution smears out at the turning point, where the minimum-energy ring polymer has a delocalised geometry. Since this geometry is an extremal point on the ring-polymer potential energy surface, subject to the centroid constraint, the path followed by the beads corresponds to a periodic orbit on the inverted potential energy

surface subject to a time-averaged constraint. In other words, the centroid constraint in CMD gives rise to artificial instantons below 250 K.

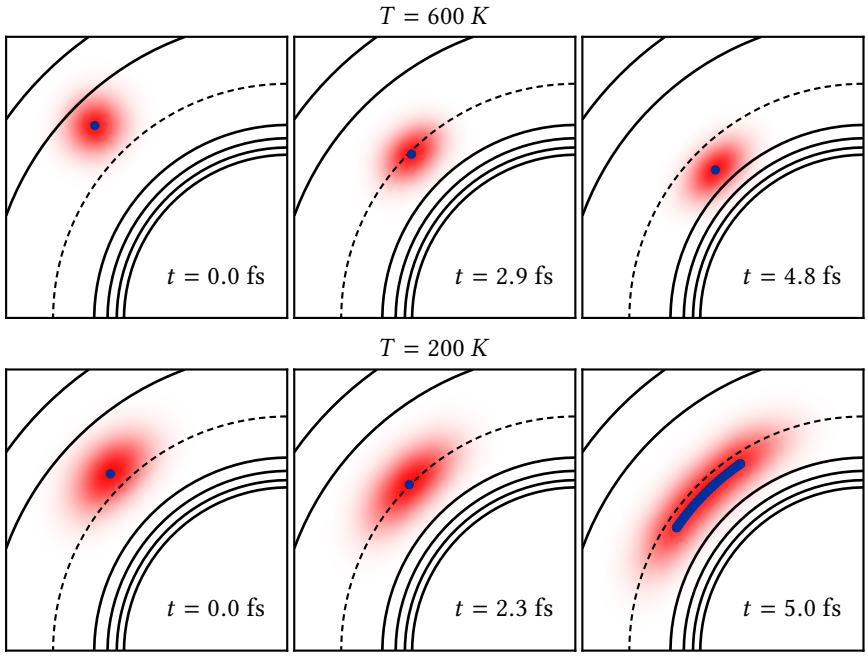

Figure 3.7 Snapshots of CMD trajectories on the Morse potential of Eq. (3.22), shown as a black contour plot with $r = r_{\mathrm{eq}}$ indicated with a dotted line. The centroid-constrained bead distributions are shown in red and the corresponding minimum-energy ring-polymer configurations are in blue. The initial configurations for the trajectories were taken from a short thermostatted PIMD simulation, and were chosen to have extremely short, but thermally accessible, inner turning points. Note the artificial instanton in the 200 K trajectory at $t = 5.0$ fs.

We can make analogies with instanton formation in quantum rate theory [13, 79, 105–107] to understand what is happening at lower temperatures. In rate theory, instantons form below a cross-over temperature; in the centroid mean-field dynamics considered here, it is more convenient to first define a "cross-over radius" R_{c}. By minimising the ring-polymer energy subject to the centroid constraint, one can show that (see Appendix A.5)

$$R_{\mathrm{c}} = -\frac{1}{m\widetilde{\omega}_1^2}\frac{\mathrm{d}V}{\mathrm{d}r}\bigg|_{r=R_{\mathrm{c}}}. \tag{3.27}$$

The values of R_{c} at 600 and 200 K are shown in Figure 3.6, and are generally found to coincide with the onset of the flat region of the centroid force. For $R_0 < R_{\mathrm{c}}$, the potential is sufficiently

curved that a centroid-constrained ring polymer can minimise its energy by stretching and moving radially outwards, following an approximately parabolic curve that cuts through the circular potential energy surface. For $R_0 > R_c$, the potential is not sufficiently curved for the ring polymers to lower their energy by cutting through the potential, hence the minimum-energy configuration is collapsed to a point at the centroid.

Given the dependence of the critical radius on temperature, quantum Boltzmann statistics can respond to the curvature of the potential in two distinct ways, giving rise to "shallow curvature" and "deep curvature" regimes, which are loosely analogous to the "shallow tunnelling" and "deep tunnelling" regimes in quantum rate theory [79]. Above the cross-over temperature (250 K in our model), the critical radius is not thermally accessible, and the ring-polymer distribution fluctuates about the centroid. Hence the repulsive part of the mean-field potential is only softened slightly. Below the cross-over temperature, the critical radius becomes thermally accessible and gives rise to artificial instantons in the dynamics. The ring-polymer distribution at the inner turning point now fluctuates about the artificial instanton instead of the centroid, drastically softening the mean-field potential. This explains why CMD gives a reasonable approximation to Matsubara dynamics above the cross-over temperature, but a poor one below it. Although tested on a simple model, we expect this result to generalise, and for it to be possible to estimate the cross-over temperature in bulk systems by searching for centroid-constrained instantons.

Chapter 4

Quasicentroid molecular dynamics

4.1 Introduction

In the previous chapter we showed that a mean-field approximation to the Kubo-transformed time-correlation function can produce accurate results, provided that the mean-field distribution is centred on the dynamical coordinate. The reason for Centroid Molecular Dynamics (CMD) breaking down at low temperatures is that its choice of coordinate allows artificial instantons to form, causing the mean-field distribution to fluctuate about these delocalised structures rather than the centroid ("the curvature problem"). Treating CMD as a special single-mode case of mean-field Matsubara dynamics, we can overcome this by releasing more normal-mode coordinates from the mean field. This works as a proof of concept, but does not constitute a practical solution to the curvature problem, since non-centroid modes (or any linear combination thereof) introduce a phase factor into the Boltzmann distribution, creating a sign problem and rendering the calculation of converged time-correlation functions unfeasible in all but the smallest systems. In light of this, we set out to formulate a theory of mean-field approximations to the quantum KTCF in *curvilinear coordinates*, hoping that this can yield a phase-free dynamics that is based on ring-polymer distributions that are compact about the dynamical coordinate.

4.2 Derivation

We begin by deriving the mean-field approximation for a general set of curvilinear coordinates in Section 4.2.1. There, we give the sufficient conditions for the corresponding dynamics to be real and phase-free, and therefore not affected by the sign problem. In Section 4.2.2 we give a particular example of curvilinear coordinates that satisfy these conditions, and discuss some

approximations to the their exact equations of motion. These approximations enable the practical implementation of a new method, which we call Quasicentroid Molecular Dynamics or QCMD.

4.2.1 General curvilinear coordinates

Consider a set of curvilinear coordinates that are related to the Matsubara modes by a canonical transformation [1],

$$\xi_k = \xi_k(\widetilde{\mathbf{Q}}_M), \qquad \widetilde{P}_{|n|\leq\mu} = \sum_{k=1}^{M} \frac{\partial \xi_k}{\partial \widetilde{Q}_n} \pi_k, \tag{4.1}$$

where $k = 1 \ldots M$. For the sake of brevity, we will drop the subscript M in $\widetilde{\mathbf{X}}_M$ and assume that $\widetilde{\mathbf{X}}$ always refers to the set of modes with $|n| \leq (M-1)/2 \equiv \mu$. In terms of these coordinates, the mean-field Matsubara Hamiltonian in Eq. (3.13) is

$$\mathcal{H}_M(\boldsymbol{\pi}, \boldsymbol{\xi}) = \frac{1}{2} \boldsymbol{\pi}^\top \mathbf{G}^{-1} \boldsymbol{\pi} + \mathcal{F}_M(\boldsymbol{\xi}), \tag{4.2}$$

where we introduce the metric tensor [89]

$$G_{kl} = \sum_n \frac{\partial \widetilde{Q}_n}{\partial \xi_k} \frac{\partial \widetilde{Q}_n}{\partial \xi_l} \tag{4.3}$$

and use mass-weighted coordinates throughout. Expressed in these coordinates, the Matsubara phase is

$$\theta_M(\boldsymbol{\pi}, \boldsymbol{\xi}) = \sum_{|n|\leq\mu} \widetilde{\omega}_n \widetilde{Q}_{\overline{n}} \widetilde{P}_n = \sum_{k=1}^{M} \left(\sum_{|n|\leq\mu} \widetilde{\omega}_n \widetilde{Q}_{\overline{n}} \frac{\partial \xi_k}{\partial \widetilde{Q}_n} \right) \pi_k = \mathbf{c}^\top \boldsymbol{\pi}, \tag{4.4}$$

where the components of the vector $\mathbf{c}$ are defined by the sum in brackets, and where we adopt the shorthand notation $\overline{n} \equiv -n$. Defining a new set of variables

$$\overline{\boldsymbol{\pi}} = \boldsymbol{\pi} - \mathrm{i}\mathbf{G}\mathbf{c}, \tag{4.5}$$

the exact quantum partition function can be written as

$$Z = \frac{1}{(2\pi\hbar)^M} \int \mathrm{d}^M \boldsymbol{\xi} \int \mathrm{d}^M \overline{\boldsymbol{\pi}}\, \mathrm{e}^{-\beta \overline{\mathcal{H}}_M(\overline{\boldsymbol{\pi}}, \boldsymbol{\xi})}, \tag{4.6}$$

where

$$\overline{\mathcal{H}}_M(\overline{\boldsymbol{\pi}}, \boldsymbol{\xi}) = \frac{1}{2}\overline{\boldsymbol{\pi}}^\top \mathbf{G}^{-1}\overline{\boldsymbol{\pi}} + \mathcal{F}_M(\boldsymbol{\xi}) + \frac{1}{2}\mathbf{c}^\top \mathbf{G}\mathbf{c}, \tag{4.7}$$

which does not appear to contain a complex phase. In reality, the phase is now part of the complex momenta $\overline{\boldsymbol{\pi}}$, and the sign problem persists. For the partition function this can be overcome by shifting the integration contour onto the real axis, making $\overline{\boldsymbol{\pi}}$ real. Then $\overline{\mathcal{H}}_M$ becomes precisely the RPMD Hamiltonian that has been mean-fielded over the non-Matsubara modes, with the last term in Eq. (4.7) being the spring energy in Eq. (3.10), expressed in curvilinear coordinates.

Repeating the same procedure for the time-correlation function in Eq. (3.12) does not solve the sign problem: analytically continuing the dynamics in this way makes it complex, as previously shown by Willatt *et al.* [82, 88]. Despite this, we may be able to obtain a real, phase-free dynamics if we apply a mean-field approximation to some of $(\boldsymbol{\pi}, \boldsymbol{\xi})$. Let us divide the curvilinear coordinates into two sets, so that $\boldsymbol{\xi} = (\boldsymbol{\xi}_a\ \boldsymbol{\xi}_b)$ and $\overline{\boldsymbol{\pi}} = (\overline{\boldsymbol{\pi}}_a\ \overline{\boldsymbol{\pi}}_b)$. We mean field the Matsubara Liouvillian in Eq. (3.8) over $(\overline{\boldsymbol{\pi}}_b, \boldsymbol{\xi}_b)$, to get a new operator

$$\mathscr{L}_{\mathrm{MF}}(\overline{\boldsymbol{\pi}}_a, \boldsymbol{\xi}_a) = \frac{\int \mathrm{d}^M\overline{\boldsymbol{\pi}}' \int \mathrm{d}^M\boldsymbol{\xi}'\, \mathrm{e}^{-\beta\overline{\mathcal{H}}_M(\overline{\boldsymbol{\pi}}', \boldsymbol{\xi}')}\, \delta(\boldsymbol{\xi}', \boldsymbol{\xi}_a)\, \delta(\overline{\boldsymbol{\pi}}', \overline{\boldsymbol{\pi}}_a)\, \hat{L}_{\mathrm{MF}}(\overline{\boldsymbol{\pi}}', \boldsymbol{\xi}')}{\int \mathrm{d}^M\overline{\boldsymbol{\pi}}' \int \mathrm{d}^M\boldsymbol{\xi}'\, \mathrm{e}^{-\beta\overline{\mathcal{H}}_M(\overline{\boldsymbol{\pi}}', \boldsymbol{\xi}')}\, \delta(\boldsymbol{\xi}', \boldsymbol{\xi}_a)\, \delta(\overline{\boldsymbol{\pi}}', \overline{\boldsymbol{\pi}}_a)}, \tag{4.8}$$

with

$$\delta(\boldsymbol{\xi}', \boldsymbol{\xi}_a) = \prod_{k\in a} \delta\left(\xi_k' - \xi_k\right), \tag{4.9}$$

and an analogous definition for $\delta(\overline{\boldsymbol{\pi}}', \overline{\boldsymbol{\pi}}_a)$. The Matsubara Liouvillian can be written as

$$\hat{L}_{\mathrm{MF}} = \mathcal{L}_a + \mathcal{L}_b, \tag{4.10}$$

where $\mathcal{L}_a$ acts only on set a and will become the operator $\mathscr{L}_{\mathrm{MF}}$ upon mean-fielding, whereas $\mathcal{L}_b$ acts only on set b and can be discarded. We show in Appendix B.1 that

$$\begin{aligned}\mathcal{L}_a = \sum_{k\in a}\Bigg\{ \left(\mathbf{G}^{-1}\overline{\boldsymbol{\pi}}\right)_k \frac{\partial}{\partial \xi_k} + \sum_{j=1}^{M} c_j \frac{\partial (\mathbf{G}\mathbf{c})_k}{\partial \xi_j}\frac{\partial}{\partial \overline{\pi}_k} - \left[\frac{\partial \mathcal{F}_M}{\partial \xi_k} + \frac{1}{2}\overline{\boldsymbol{\pi}}^\top \frac{\partial \mathbf{G}^{-1}}{\partial \xi_k}\overline{\boldsymbol{\pi}} + \frac{1}{2}\mathbf{c}^\top \frac{\partial \mathbf{G}}{\partial \xi_k}\mathbf{c}\right]\frac{\partial}{\partial \overline{\pi}_k}\Bigg\} \\ + \mathrm{i}\sum_{k\in a}\Bigg\{ c_k \frac{\partial}{\partial \xi_k} + \sum_{j=1}^{M}\left(\mathbf{G}^{-1}\overline{\boldsymbol{\pi}}\right)_j \left[\left(\frac{\partial \mathbf{G}}{\partial \xi_k}\mathbf{c}\right)_j - \left(\frac{\partial \mathbf{G}\mathbf{c}}{\partial \xi_j}\right)_k\right]\frac{\partial}{\partial \overline{\pi}_k}\Bigg\}.\end{aligned} \tag{4.11}$$

We can make the first term in the imaginary part of the Liouvillian vanish by requiring that $c_{k\in a} = 0$. Note that

$$c_k = \sum_{|n|\leq\mu} \widetilde{\omega}_n \widetilde{Q}_{\overline{n}} \frac{\partial \xi_k}{\partial \widetilde{Q}_n} = -\sum_{|n|\leq\mu} \frac{\mathrm{d}\widetilde{Q}_n}{\mathrm{d}\tau} \frac{\partial \xi_k}{\partial \widetilde{Q}_n} = -\frac{\mathrm{d}\xi_k}{\mathrm{d}\tau}, \tag{4.12}$$

where τ is imaginary time, and the derivative $\mathrm{d}\widetilde{Q}_n/\mathrm{d}\tau$ is defined in Eq. (B.6). Therefore enforcing the condition $c_{k\in a} = 0$ is equivalent to making all $\xi_{k\in a}$ invariant under imaginary-time translation. In Appendix B.2.2 we prove that it is possible to make *all* of $\boldsymbol{\xi}$ satisfy this property, except for a single coordinate ξ_τ, which instead satisfies

$$\frac{\partial \widetilde{Q}_n}{\partial \xi_\tau} = \alpha \frac{\mathrm{d}\widetilde{Q}_n}{\mathrm{d}\tau} = -\alpha \widetilde{\omega}_n \widetilde{Q}_{\overline{n}}, \tag{4.13}$$

where α is a proportionality constant, so that

$$c_k = -\frac{\mathrm{d}\xi_k}{\mathrm{d}\tau} = -\alpha^{-1} \frac{\partial \xi_k}{\partial \xi_\tau} = \begin{cases} -\alpha^{-1} & \text{if } \xi_k \equiv \xi_\tau, \\ 0 & \text{otherwise.} \end{cases} \tag{4.14}$$

We also prove that each of the coordinates in such a symmetrised set is either symmetric (Σ^+) or antisymmetric (Σ^-) with respect to imaginary-time reversal, $\tau \longrightarrow -\tau$. Choosing all of $\xi_{k\in a}$ to be Σ^+ (see Appendix B.2.3) causes the imaginary terms in the Liouvillian to vanish under mean-fielding, giving

$$\mathscr{L}_{\mathrm{MF}}(\overline{\boldsymbol{\pi}}_a, \boldsymbol{\xi}_a) = \{\,\cdot\,, \mathscr{H}_{\mathrm{MF}}\} = \sum_{k\in a} \frac{\partial \mathscr{H}_{\mathrm{MF}}}{\partial \overline{\pi}_k} \frac{\partial}{\partial \xi_k} - \frac{\partial \mathscr{H}_{\mathrm{MF}}}{\partial \xi_k} \frac{\partial}{\partial \overline{\pi}_k} \tag{4.15}$$

where

$$\begin{aligned} \mathrm{e}^{-\beta \mathscr{H}_{\mathrm{MF}}(\overline{\boldsymbol{\pi}}_a, \boldsymbol{\xi}_a)} &= \frac{1}{(2\pi\hbar)^b} \int \mathrm{d}^M \overline{\boldsymbol{\pi}}' \int \mathrm{d}^M \boldsymbol{\xi}' \mathrm{e}^{-\beta \overline{\mathcal{H}}_M(\overline{\boldsymbol{\pi}}, \boldsymbol{\xi})}\, \delta(\boldsymbol{\xi}', \boldsymbol{\xi}_a)\, \delta(\overline{\boldsymbol{\pi}}', \boldsymbol{\pi}_a) \\ &= \lim_{N\to\infty} \frac{1}{(2\pi\hbar)^{N-a}} \int \mathrm{d}^N \mathbf{p} \int \mathrm{d}^N \mathbf{q}\, \mathrm{e}^{-\beta_N H_N(\mathbf{p},\mathbf{q})}\, \delta(\mathbf{q}, \boldsymbol{\xi}_a)\, \delta(\mathbf{p}, \overline{\boldsymbol{\pi}}_a), \end{aligned} \tag{4.16}$$

with $H_N(\mathbf{p}, \mathbf{q})$ denoting the ring-polymer Hamiltonian in Eq. (2.29). In the final line we rely on the fact that the free energy $\mathscr{H}_{\mathrm{MF}}(\overline{\boldsymbol{\pi}}_a, \boldsymbol{\xi}_a)$ is a static property, and must therefore be the same in the limit $M \longrightarrow \infty$, regardless of whether the curvilinear coordinates $(\overline{\boldsymbol{\pi}}_a, \boldsymbol{\xi}_a)$ are defined in terms of all the normal modes or are restricted to the Matsubara space. This allows us to

re-express the variables in terms of the bead coordinates, with

$$\delta(\mathbf{q}, \boldsymbol{\xi}_a) = \prod_{k \in a} \delta\big(\xi'_k(\mathbf{q}) - \xi_k\big) \tag{4.17}$$

and

$$\delta(\mathbf{p}, \overline{\boldsymbol{\pi}}_a) = \prod_{k \in a} \delta\Bigg(\sum_{l=1}^{N} \frac{\partial q_l}{\partial \xi_k} p_l - \overline{\pi}_k\Bigg). \tag{4.18}$$

The exact KTCF is then approximated by

$$\mathscr{C}_{AB}^{[a]}(t) = \frac{1}{(2\pi\hbar)^a} \int \mathrm{d}^a \overline{\boldsymbol{\pi}}_a \int \mathrm{d}^a \boldsymbol{\xi}_a \, \mathrm{e}^{-\beta \mathscr{H}_{\mathrm{MF}}(\overline{\boldsymbol{\pi}}_a, \boldsymbol{\xi}_a)} A(\boldsymbol{\xi}_a) \mathrm{e}^{\mathscr{L}_{\mathrm{MF}}(\overline{\boldsymbol{\pi}}_a, \boldsymbol{\xi}_a) t} B(\boldsymbol{\xi}_a), \tag{4.19}$$

where $A(\boldsymbol{\xi}_a), B(\boldsymbol{\xi}_a)$ are some suitably chosen estimators. From Eq. (4.15) we see that the corresponding dynamics is real, classical, and conserves the mean-field quantum Boltzmann distribution.[1] Crucially, it does not suffer from the sign problem and should therefore be computationally tractable, provided that the derivatives of the Hamiltonian in Eq. (4.15) are available. In the next section we discuss how this can be achieved in practice for a particular set of curvilinear coordinates.

4.2.2 Polar quasicentroids

One set of coordinates that are invariant under imaginary-time translation and reversal are the Cartesian centroids $\widetilde{\mathbf{Q}}_0$. They are key to the CMD method, and form a good basis for the mean-field approximation of quantum TCFs so long as the mean-field ring-polymer distribution fluctuates about $\widetilde{\mathbf{Q}}_0$. We have seen in Chapter 3 that this is not always the case on curved potential energy surfaces, where the distribution can instead fluctuate about a delocalised instanton. This causes the quality of the mean-field approximation to deteriorate and leads to the curvature problem. Rather than using Cartesian centroids, which are the averages of Cartesian coordinates,

$$\widetilde{X}_0 = \frac{1}{N} \sum_{l=1}^{N} x_l \qquad\qquad \widetilde{Y}_0 = \frac{1}{N} \sum_{l=1}^{N} y_l, \tag{4.20}$$

[1] We have shown this for a one-dimensional system, but can easily generalise.

we can instead consider the averages of polar coordinates,

$$R = \frac{1}{N}\sum_{l=1}^{N} r_l \qquad\qquad \Theta = \frac{1}{N}\sum_{l=1}^{N} \theta_l, \tag{4.21}$$

defined here for a two-dimensional system, so that[2]

$$r_l = \sqrt{x_l^2 + y_l^2} \qquad\qquad \theta_l = \tan^{-1}(y_l/x_l). \tag{4.22}$$

Clearly these coordinates have Σ^+ symmetry, and so their mean-field dynamics must be real and phase-free. Furthermore, on the potential energy surfaces considered here, it is impossible for a ring polymer constrained at an average radius and angle to lower its energy by stretching into an instanton (see Appendix B.3.1). This ensures that the coordinates (R, Θ) always describe the centre of the ring-polymer distribution, rather than its approximate focal point. The exact mean-field Hamiltonian associated with these coordinates is given by

$$\begin{aligned} \mathrm{e}^{-\beta\mathscr{H}_{\mathrm{MF}}(\pi_R,\pi_\Theta,R,\Theta)} &= N\left(\frac{m}{2\pi\beta_N\hbar^2}\right)^{N-1}\int \mathrm{d}^N\mathbf{r}'\int \mathrm{d}^N\boldsymbol{\theta}' \\ &\times \frac{J(\mathbf{r}')}{\rho(\mathbf{r}')}\mathrm{e}^{-\beta[T(\pi_R,\pi_\Theta,\rho(\mathbf{r}'))+W_N(\mathbf{r}',\boldsymbol{\theta}')]}\delta(R'-R)\delta(\Theta'-\Theta), \end{aligned} \tag{4.23}$$

where we have integrated the momenta analytically (see Appendix B.3.2), and defined

$$T(\pi_R,\pi_\Theta,\rho) = \frac{\pi_R^2}{2m} + \frac{\pi_\Theta^2}{2m\rho^2}, \qquad \rho(\mathbf{r}) = \left(\frac{1}{N}\sum_{l=1}^{N} r_l^2\right)^{1/2}, \qquad J(\mathbf{r}) = \prod_{l=1}^{N} r_l. \tag{4.24}$$

In principle, we could now use Eq. (4.15) to set up the equations of motion for R and Θ. However, standard numerical integrators rely on the Hamiltonian being separable [46], and so we would like to write $\mathscr{H}_{\mathrm{MF}}$ as a sum of a kinetic energy that depends only on the momenta, and a potential energy that depends only on the positions. To do this, we introduce the Cartesian coordinates

$$\overline{Q}_x = R\cos\Theta \qquad\qquad \overline{Q}_y = R\sin\Theta. \tag{4.25}$$

In general, $\overline{\mathbf{Q}} \neq \widetilde{\mathbf{Q}}_0$ due to the non-linear relation between bead Cartesian and polar coordinates. However, it is easy to show that $\overline{\mathbf{Q}} \simeq \widetilde{\mathbf{Q}}_0$ if the distribution is reasonably compact, and that $\overline{\mathbf{Q}} \to \widetilde{\mathbf{Q}}_0$ in the high-temperature limit. We will therefore refer to $\overline{\mathbf{Q}}$ as the position of the

[2] The branch cut in $\tan^{-1}$ is chosen so that all the beads lie on the same branch.

"quasicentroid". We can express the mean-field kinetic energy in terms of the quasicentroid momenta if we approximate the moment of inertia $2m\rho^2$ by $2mR^2$, giving

$$T(\pi_R, \pi_\Theta, \rho) \simeq \frac{\pi_R^2}{2m} + \frac{\pi_\Theta^2}{2mR^2} = \frac{|\overline{\mathbf{P}}|^2}{2m}, \tag{4.26}$$

which factorises out of the integral in Eq. (4.23). For consistency, we also make the substitution $\rho(\mathbf{r}) \longrightarrow R$ in the remaining factor, which defines the mean-field potential energy $\mathscr{F}_{\mathrm{MF}}$. On expanding its gradient $\boldsymbol{\nabla}_{\overline{\mathbf{Q}}}\mathscr{F}_{\mathrm{MF}}$ it appears that the mean-field forces have significant contributions from the springs $S_N(\mathbf{r}, \boldsymbol{\theta})$, in contrast to the centroids in CMD. In fact, we show in Appendix B.3.3 that the spring forces are cancelled almost exactly by contributions from the Jacobian $J(\mathbf{r})$, so we can make the approximation

$$\frac{\partial \mathscr{F}_{\mathrm{MF}}}{\partial \overline{\mathbf{Q}}} \simeq \frac{1}{\overline{Z}(\overline{\mathbf{Q}})} \left\langle \frac{\partial V_N(\mathbf{q})}{\partial \overline{\mathbf{Q}}} \right\rangle_{(R,\Theta)}, \tag{4.27}$$

where

$$\langle \cdots \rangle_{(R,\Theta)} \equiv N \left(\frac{m}{2\pi\beta_N\hbar^2} \right)^{N-1} \int \mathrm{d}^{2N}\mathbf{q}' \, (\cdots) \, \mathrm{e}^{-\beta W_N(\mathbf{q}')} \, \delta(R' - R) \, \delta(\Theta' - \Theta), \tag{4.28}$$

and $\overline{Z}(\overline{\mathbf{Q}}) = \langle 1 \rangle_{(R,\Theta)}$. A similar approximation in Chapter 5 will allow us to calculate mean-field forces in more complicated systems. Combining Eqs. (4.26) and (4.27) we get the QCMD time-correlation function, which in two dimensions reads

$$\overline{C}_{AB}(t) = \frac{1}{(2\pi\hbar)^2} \int \mathrm{d}^2\overline{\mathbf{P}} \int \mathrm{d}^2\overline{\mathbf{Q}} \, \mathrm{e}^{-\beta \overline{H}(\overline{\mathbf{P}}, \overline{\mathbf{Q}})} A(\overline{\mathbf{Q}}) B(\overline{\mathbf{Q}}_t), \tag{4.29}$$

with

$$\overline{H}(\overline{\mathbf{P}}, \overline{\mathbf{Q}}) = |\overline{\mathbf{P}}|^2/2m + \overline{F}(\overline{\mathbf{Q}}), \tag{4.30}$$

where $\overline{F}(\overline{\mathbf{Q}}) \simeq \mathscr{F}_{\mathrm{MF}}(\overline{\mathbf{Q}})$ is the free energy obtained by doing work with the approximate force in Eq. (4.27), and $\overline{\mathbf{Q}}_t$ is the quasicentroid configuration that has been propagated for time t according to

$$\dot{\overline{\mathbf{Q}}} = \overline{\mathbf{P}}/m, \qquad \dot{\overline{\mathbf{P}}} = -\boldsymbol{\nabla}\overline{F}(\overline{\mathbf{Q}}). \tag{4.31}$$

In the next section we test how well this approximation works for the quantum TCFs of a two-dimensional model system.

4.3 The two-dimensional Morse potential

We consider the Morse potential of Section 3.3 and use QCMD to calculate the power spectrum defined in Eqs. (3.23) and (3.24). We compare our results to the outcomes of CMD simulations, which only approximate the dynamics, but conserve the exact quantum Boltzmann distribution and use the exact position and velocity estimators. QCMD replaces the exact mean-field Hamiltonian with the one defined in Eq. (4.30) and substitutes $(\overline{\mathbf{P}}, \overline{\mathbf{Q}})$ for the exact estimators $(\widetilde{\mathbf{P}}_0, \widetilde{\mathbf{Q}}_0)$. We thus expect QCMD to be less accurate than CMD when the temperature is high enough to neglect the curvature problem. However at lower temperatures, where it cannot be neglected, we expect the better treatment of the dynamics by QCMD to far outweigh the small errors in the Boltzmann distribution.

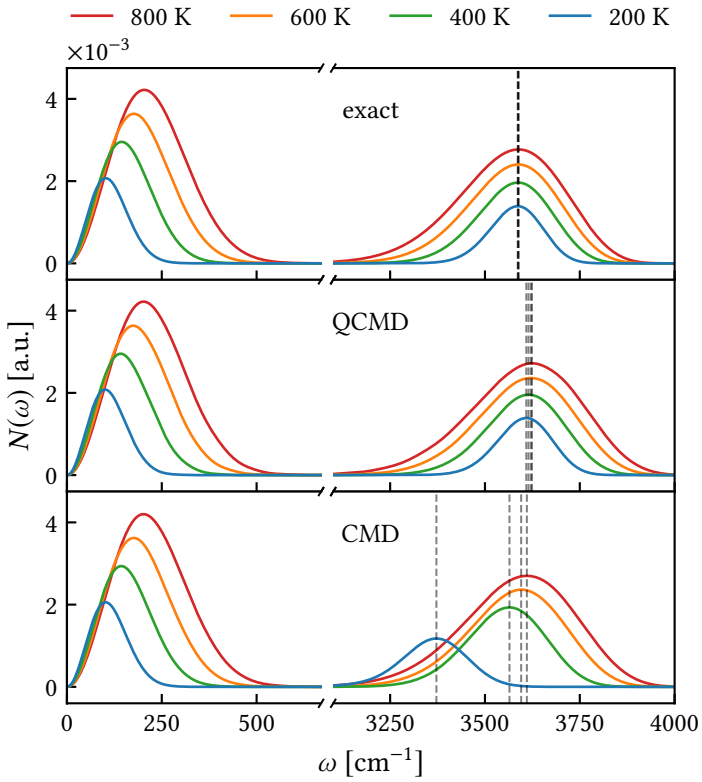

Figure 4.1 Simulated vibrational power spectra for the Morse potential in Eq. (3.22). The spectra in the first and third panel (exact and CMD) are the same as in Figure 3.5. The QCMD spectra in the second panel are new and show an OH-stretch peak (around 3600 cm^{-1}) that maintains its shape and, to a large extent, its position as the temperature is lowered from 800 to 200 K. Overall the absorption maximum (dotted line) only shifts by about 15 cm^{-1}. This is in contrast to CMD, for which the OH stretch shifts by over 200 $\mathrm{cm}^{-1}$and noticeably broadens as the temperature is lowered.

To run the QCMD simulations, we first calculate the mean-field forces in Eq. (4.27). Because the Morse potential is centrosymmetric, the corresponding estimator takes the form

$$-\frac{\partial V_N(\mathbf{q})}{\partial \overline{\mathbf{Q}}} = \frac{\overline{\mathbf{Q}}}{R} f_R(\mathbf{q}), \tag{4.32}$$

where

$$f_R(\mathbf{q}) \equiv -\frac{\partial V_N(\mathbf{q})}{\partial R} = -\frac{1}{N}\sum_{l=1}^{N}\frac{\mathbf{q}_l}{r_l}\cdot\boldsymbol{\nabla}V(\mathbf{q}_l), \tag{4.33}$$

which does not depend on Θ. It is therefore sufficient to calculate $\langle f_R(\mathbf{q})\rangle_{(R,\Theta)}$ on a one-dimensional grid in R, using standard PIMD [50] and imposing the quasicentroid constraints with SHAKE/RATTLE [50, 108–110]. Further simulation details can be found in Appendix B.4.

The simulated spectra (Figure 4.1) are in excellent agreement with the exact quantum results at all temperatures tested, with no sign of a curvature problem. Figure 4.2 makes a close comparison of the QCMD OH-stretch band with the mean-field Matsubara results of Section 3.3. We see that the QCMD peaks have small (≈ 10 cm^{-1}) blueshifts with respect to the Matsubara peaks. The shifts change slightly with temperature, ranging from 14 cm^{-1} at 800 K to 6 cm^{-1} at 200 K. This variation appears to be the result of small differences in the line shape, rather than an underlying curvature problem. It may also partly stem from the convergence artefacts in the Matsubara results.

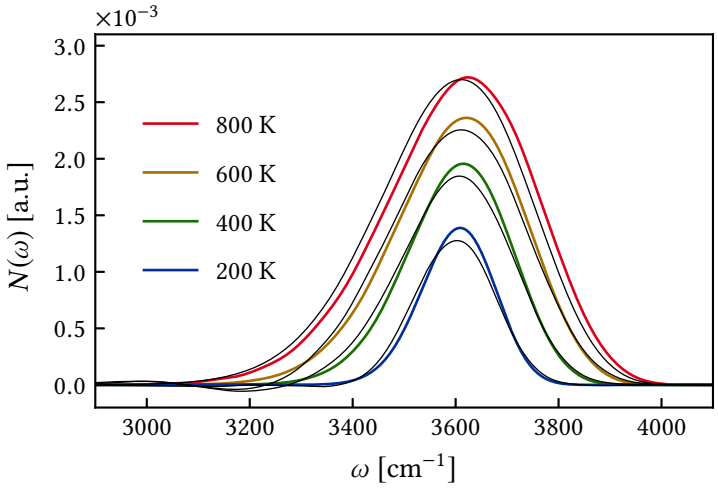

Figure 4.2 A zoomed-in view of the QCMD spectra in the OH-stretch region, overlaid with the mean-field Matsubara spectra (black lines) from the second panel of Figure 3.5.

As expected, the QCMD distributions show no artificial instantons (see Figure 4.3), always remaining compact about the quasicentroid. Alternatively, we can say that the quasicentroid is always representative of the mean-field bead distribution, residing at or near its mode.[3] This is precisely the property that we have singled out as crucial for the accuracy of a mean-field approximation, and our results give further support to this idea. Even as we attempt to push QCMD to its limits by reducing the simulation temperature to 50 K, the ring-polymer distribution remains compact, and the agreement of QCMD with the exact quantum spectrum

[3]Here "mode" is meant in a statistical sense, and not as in "normal mode".

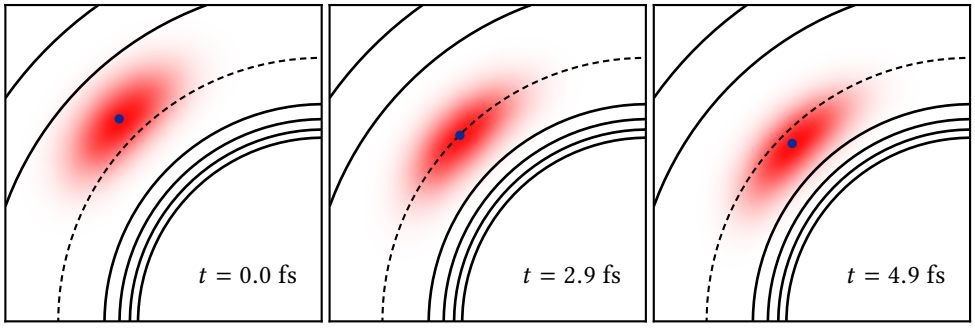

Figure 4.3 Snapshots of a 200 K QCMD trajectory on the Morse potential of Eq. (3.22), shown as a black contour plot with $r = r_{\mathrm{eq}}$ indicated with a dotted line. The quasicentroid-constrained bead distribution is drawn in red and the corresponding quasicentroid is in blue. The initial configuration was taken from a thermalised QCMD trajectory, and chosen to have an extremely short, yet thermally accessible, inner turning point. Note that the bead distribution remains compact about the quasicentroid, in contrast to the 200 K CMD trajectory in Figure 3.7.

is as close as at the higher temperatures shown in Figure 4.1. This suggests that QCMD continues to give a good approximation to Matsubara dynamics down to 50 K, where we are unable to compute the Matsubara spectrum due to the severity of the sign problem.

Given the excellent agreement of the QCMD and Matsubara spectra, we expect that the approximations QCMD makes to the quantum Boltzmann distribution and the estimators are relatively small. This can be tested by comparing QCMD static averages with the results of exact quantum calculations. We find that the QCMD expectation values of the bond length are in perfect agreement with the exact values (to within sampling error) at all temperatures tested. The largest error in the $t = 0$ limit of the dipole autocorrelation function is 2% at 200 K, and the dipole-*derivative* autocorrelation function is exact at $t = 0$ by construction. Overall, this confirms that the additional approximations made by QCMD do not have a significant effect, and encourages us to apply the new method to more complicated systems.

Chapter 5

Vibrational dynamics of water

5.1 Implementation

In the previous chapter we introduced Quasicentroid Molecular Dynamics (QCMD)—a new path-integral method based on the mean-field dynamics of curvilinear centroids. We have shown that QCMD produces remarkably accurate approximations to Matsubara dynamics spectra of a two-dimensional model system. Now we will use QCMD to simulate the vibrational dynamics of more complex systems, namely a single (gaseous) water molecule described by the Partridge–Schwenke potential [111, 112], and a box of water molecules in the condensed phase (96 molecules for ice, 128 for liquid), described by the q-TIP4P/F potential [11]. To do this, we define a new set of quasicentroid coordinates, suitable for a bent triatomic molecule, and introduce some further approximations that allow us to calculate the mean-field forces on the fly.

5.1.1 Quasicentroid coordinates

To describe a single water molecule we need nine coordinates, which should ideally give rise to compact mean-field distributions. By analogy with Section 4.2.2, we define three of them to be the bond-angle centroids

$$R_1 = \frac{1}{N}\sum_l r_{l1}, \quad r_{l1} = \left|\mathbf{q}_l^{(\mathrm{OH}_1)}\right|, \qquad R_2 = \frac{1}{N}\sum_l r_{l2}, \quad r_{l2} = \left|\mathbf{q}_l^{(\mathrm{OH}_2)}\right|, \tag{5.1a}$$

$$\Theta = \frac{1}{N}\sum_l \theta_l, \quad \theta_l = \arccos\left[\frac{\mathbf{q}_l^{(\mathrm{OH}_1)}\cdot\mathbf{q}_l^{(\mathrm{OH}_2)}}{r_{l1}r_{l2}}\right], \tag{5.1b}$$

where $\mathbf{q}_l^{(\mathrm{OH}_{1,2})} = \mathbf{q}_l^{(\mathrm{H}_{1,2})} - \mathbf{q}_l^{(\mathrm{O})}$ are the displacement vectors between the oxygen and hydrogen atoms in the l-th water molecule replica ($l = 1 \dots N$).

A further six coordinates are needed to specify the centre of mass (CoM) and the orientation. For this we take inspiration from molecular spectroscopy, where such external degrees of freedom are defined using the Eckart frame. This relates the instantaneous molecular configuration to a reference geometry—usually the equilibrium structure [113, 114]. In our "Eckart-like" frame, the instantaneous configuration is that of the ring polymers describing a water molecule, and the "reference" is given by the corresponding quasicentroids. These are oriented so as to satisfy the conditions

$$\sum_{\alpha,l} m_\alpha (\mathbf{q}_l^{(\alpha)} - \overline{\mathbf{Q}}^{(\alpha)}) = \mathbf{0}, \tag{5.2a}$$

$$\sum_{\alpha,l} m_\alpha \overline{\mathbf{Q}}^{(\alpha)} \times (\mathbf{q}_l^{(\alpha)} - \overline{\mathbf{Q}}^{(\alpha)}) = \mathbf{0}, \tag{5.2b}$$

where $\overline{\mathbf{Q}}^{(\alpha)}$ are the atom quasicentroids with $\alpha = (\mathrm{H}_1, \mathrm{H}_2, \mathrm{O})$. It is easy to show that these conditions are equivalent to

$$\sum_{\alpha} m_\alpha (\widetilde{\mathbf{Q}}_0^{(\alpha)} - \overline{\mathbf{Q}}^{(\alpha)}) = \mathbf{0}, \tag{5.3a}$$

$$\sum_{\alpha} m_\alpha \overline{\mathbf{Q}}^{(\alpha)} \times (\widetilde{\mathbf{Q}}_0^{(\alpha)} - \overline{\mathbf{Q}}^{(\alpha)}) = \mathbf{0}, \tag{5.3b}$$

where $\widetilde{\mathbf{Q}}_0^{(\alpha)}$ are the atom centroids. Unlike the internal (bond-angle) coordinates, the external coordinates are defined implicitly. We can get an explicit form for the quasicentroid CoM coordinate from Eq. (5.2a), or, equivalently, Eq. (5.3a); namely, we can show that it is equal to the centroid centre of mass. We cannot easily get an explicit form for the orientational coordinate, but can describe some of their properties. In particular, it can be shown that enforcing the orientational Eckart condition in Eqs. (5.2b) and (5.3b) has the effect of rotating the molecule so that the sum

$$\sum_{\alpha,l} m_\alpha |\mathbf{q}_l^{(\alpha)} - \overline{\mathbf{Q}}^{(\alpha)}|^2$$

or, equivalently,

$$\sum_{\alpha} m_\alpha |\widetilde{\mathbf{Q}}_0^{(\alpha)} - \overline{\mathbf{Q}}^{(\alpha)}|^2,$$

is minimised [115, 116]. Therefore, according to our definition, the quasicentroid configuration of a ring-polymerised water molecule has the internal coordinates given by Eq. (5.1), shares its centre of mass with the ring-polymerised molecule, and is oriented so as to minimise the mass-weighted sum of square distances between the quasicentroids and the corresponding replica atoms (or, equivalently, their centroids).

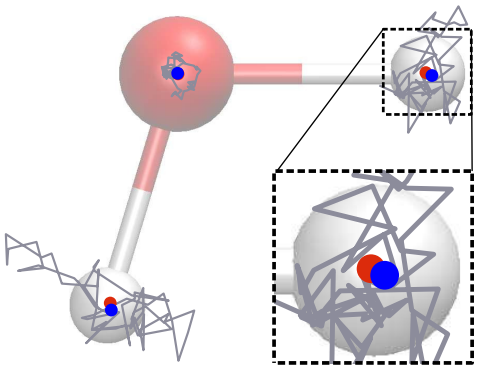

Figure 5.1 A typical ring-polymer geometry from a QCMD water simulation at 150 K, showing how the quasicentroids defined using the Eckart-like conditions are oriented so that the atom centroids (red) almost coincide with the atom quasicentroids (blue).

The Eckart-like conditions thus ensure that the quasicentroid-constrained ring-polymer distribution is compact with respect to the orientational degrees of freedom, and that the atom centroids and quasicentroids are usually very close (see Figure 5.1).

5.1.2 Quasicentroid forces

To calculate the quasicentroid forces we make use of the two approximations in Section 4.2.2. We first assume that the kinetic energy of the Cartesian quasicentroids is separable, so that

$$\dot{\overline{\mathbf{Q}}}^{(\alpha)} = \overline{\mathbf{P}}^{(\alpha)}/m_\alpha, \tag{5.4}$$

where $\overline{\mathbf{P}}^{(\alpha)}$ is the Cartesian quasicentroid momentum of atom α, and m_α is its mass. Next we assume that the quasicentroid forces derived from the ring-polymer springs and the transformation Jacobian average to zero, so that

$$\dot{\overline{\mathbf{P}}} = -\frac{\partial \mathscr{F}_{\mathrm{MF}}}{\partial \overline{\mathbf{Q}}} \simeq \frac{1}{\overline{Z}(\overline{\mathbf{Q}})} \left\langle -\frac{\partial V_N(\mathbf{q})}{\partial \overline{\mathbf{Q}}} \right\rangle_{\overline{\mathbf{Q}}}, \tag{5.5}$$

where

$$\langle \cdots \rangle_{\overline{\mathbf{Q}}} = \int \mathrm{d}\mathbf{q}' \, (\cdots) \, \mathrm{e}^{-\beta W_N(\mathbf{q}')} \delta(\overline{\mathbf{Q}}' - \overline{\mathbf{Q}}), \tag{5.6}$$

and $\overline{Z}(\overline{\mathbf{Q}}) = \langle 1 \rangle_{\overline{\mathbf{Q}}}$. To get an expression for $-\partial V_N(\mathbf{q})/\partial \overline{\mathbf{Q}}$ we introduce bond-angle coordinates for each of the water-molecule replicas. These are the r_{l1}, r_{l2}, and θ_l defined in Eq. (5.1). To

complete the set we define the centre-of-mass coordinates

$$\mathbf{q}_l^{(c)} = \left(\sum_\alpha m_\alpha \mathbf{q}_l^{(\alpha)} \right) \Big/ \left(\sum_\alpha m_\alpha \right), \tag{5.7}$$

and the orientational coordinates $\boldsymbol{\omega}_l$, which we leave unspecified. For a given molecule, its l-th replica experiences a centre-of-mass (CoM) force

$$\mathbf{f}_l^{(c)} = -\frac{\partial V(\mathbf{q})}{\partial \mathbf{q}_l^{(c)}} = -\sum_\alpha \frac{\partial V(\mathbf{q})}{\partial \mathbf{q}_l^{(\alpha)}}. \tag{5.8}$$

The replica also experiences a torque about its centre of mass,

$$\boldsymbol{\tau}_l^{(c)} = -\frac{\partial V(\mathbf{q})}{\partial \boldsymbol{\omega}_l} = -\sum_\alpha \left(\mathbf{q}_l^{(\alpha)} - \mathbf{q}_l^{(c)} \right) \times \frac{\partial V(\mathbf{q})}{\partial \mathbf{q}_l^{(\alpha)}}. \tag{5.9}$$

The Cartesian forces acting on atom α of this replica can be written as

$$-\frac{\partial V(\mathbf{q})}{\partial \mathbf{q}_l^{(\alpha)}} = \mathbf{f}_{\mathrm{int},l}^{(\alpha)} + m_\alpha \left[\frac{\mathbf{f}_l^{(c)}}{m_{\mathrm{tot}}} + \left(\mathbf{I}_l^{-1} \boldsymbol{\tau}_l^{(c)} \right) \times \left(\mathbf{q}_l^{(\alpha)} - \mathbf{q}_l^{(c)} \right) \right], \tag{5.10}$$

where $\mathbf{I}_l$ is the inertia tensor about $\mathbf{q}_l^{(c)}$ [89, pp. 950–951]. The first term in square brackets is the atom's contribution to the net CoM force. The second term is its contribution to the rotational force about the CoM. The remainder $\mathbf{f}_{\mathrm{int},l}^{(\alpha)}$ is its contribution to the internal forces, which act to distort the molecule but contribute no net CoM force or torque. From these we can isolate the forces on the bond lengths r_{lk} $(k = 1, 2)$,

$$f_l^{(r_k)} = \frac{\mathbf{q}_l^{(\mathrm{OH}_k)}}{r_{lk}} \cdot \mathbf{f}_{\mathrm{int},l}^{(\mathrm{H}_k)}, \tag{5.11}$$

and the bond angle θ_l,

$$f_l^{(\theta)} = \frac{r_{l1}}{\sin\theta_l} \left(\frac{\mathbf{q}_l^{(\mathrm{OH}_1)}}{r_{l1}} \cos\theta_l - \frac{\mathbf{q}_l^{(\mathrm{OH}_2)}}{r_{l2}} \right) \cdot \mathbf{f}_{\mathrm{int},l}^{(\mathrm{H}_1)}. \tag{5.12}$$

In the absence of an external torque, the corresponding internal quasicentroid forces are just the averages

$$\overline{f}^{(R_k)} = \frac{1}{N} \sum_{l=1}^{N} f_l^{(r_k)} \qquad \overline{f}^{(\Theta)} = \frac{1}{N} \sum_{l=1}^{N} f_l^{(\theta)}. \tag{5.13}$$

When there is a net torque acting on the molecule, this remains a good approximation, as the Eckart conditions in Eq. (5.2) minimise the coupling between the vibrational and rotational coordinates [114]. Converted to Cartesian representation, Eq. (5.13) becomes

$$\overline{\mathbf{f}}_{\text{int}}^{(\text{H}_k)} = \frac{\overline{\mathbf{Q}}^{(\text{OH}_k)}}{R_k}\overline{f}^{(R_k)} + \frac{1}{R_k \sin\Theta}\left(\frac{\overline{\mathbf{Q}}^{(\text{OH}_k)}}{R_k}\cos\Theta - \frac{\overline{\mathbf{Q}}^{(\text{OH}_j)}}{R_j}\right)\overline{f}^{(\Theta)} \tag{5.14a}$$

$$\overline{\mathbf{f}}_{\text{int}}^{(\text{O})} = -\left(\overline{\mathbf{f}}_{\text{int}}^{(\text{H}_1)} + \overline{\mathbf{f}}_{\text{int}}^{(\text{H}_2)}\right), \tag{5.14b}$$

where $(k, j) = (1, 2)$ or $(2, 1)$. For the external forces, the CoM component is also a simple average,

$$\overline{\mathbf{f}}^{(c)} = \frac{1}{N}\sum_{l=1}^{N}\mathbf{f}_l^{(c)}. \tag{5.15}$$

The same is not true for the rotational component, but in the absence of an explicit expression for the orientational quasicentroid coordinate we nonetheless approximate the corresponding torque as

$$\overline{\boldsymbol{\tau}}^{(c)} \simeq \frac{1}{N}\sum_{l=1}^{N}\boldsymbol{\tau}_l^{(c)}. \tag{5.16}$$

Substituting the quasicentroid coordinates and forces from Eqs. (5.14) to (5.16) into Eq. (5.10) gives the final expression for $-\partial V_N(\mathbf{q})/\partial\overline{\mathbf{Q}}$.

Note on the quasicentroid torque The approximation we made in Eq. (5.16) is somewhat crude and leads to low-frequency artefacts in simulated infrared absorption spectra (see Section 5.3). We have since devised a different approximation, which gives the quasicentroid torque as the solution to

$$\mathbf{M}\mathbf{I}^{-1}\overline{\boldsymbol{\tau}} = \sum_{\alpha}\left[\overline{\mathbf{f}}_{\text{int}}^{(\alpha)} \times \widetilde{\mathbf{D}}^{(\alpha)} + \frac{\partial V_N(\mathbf{q})}{\partial \widetilde{\mathbf{Q}}_0^{(\alpha)}} \times \overline{\mathbf{D}}^{(\alpha)}\right], \tag{5.17}$$

where $\overline{\mathbf{D}}^{(\alpha)}$ and $\widetilde{\mathbf{D}}^{(\alpha)}$ denote the (quasi-)centroid coordinates in the CoM frame, and $\mathbf{I}$ is the quasicentroid inertia tensor about the centre of mass. The matrix $\mathbf{M}$ is given by

$$M_{jk} = \sum_{\alpha} m_\alpha \left\{\left(\overline{\mathbf{D}}^{(\alpha)} \cdot \widetilde{\mathbf{D}}^{(\alpha)}\right)\delta_{jk} - \overline{D}_j^{(\alpha)}\widetilde{D}_k^{(\alpha)}\right\}, \tag{5.18}$$

as derived in Appendix C.1. At the time of writing, this expression was still undergoing numerical testing and showing great promise based on preliminary results from simulations of q-TIP4P/F liquid water at 300 K [117].

5.1.3 Adiabatic propagator

In Section 4.3 of the previous chapter and in Section 5.2 of this chapter we apply QCMD to systems that are small enough for the mean-field quasicentroid forces to be pre-calculated on a grid. To apply QCMD to larger systems, we will adapt the adiabatic CMD (ACMD) algorithm used in previous work to calculate the mean-field centroid force on the fly [104, 118, 119]. As discussed in Chapter 3, ACMD achieves adiabatic separation by making the non-centroid modes move on a faster timescale, scaling their masses and frequencies as

$$m_n = m \;\rightarrow\; m_n = m\left(\frac{\beta\hbar\omega_n}{\gamma N}\right)^2 \qquad \omega_n \;\rightarrow\; \omega_n = \frac{\gamma N}{\beta\hbar} \tag{5.19}$$

where γ is the "adiabaticity parameter". The time-averaged forces on the centroid tend to their exact mean-field value in the limit as $\gamma \rightarrow \infty$ [104], although relatively small values of γ are sufficient to produce converged rovibrational spectra. For example, a value of $\gamma = 64$ gives a good approximation to CMD in gas-phase water at 150 K.

It is possible to modify ACMD to adiabatically separate the motion of the quasicentroids from that of the other degrees of freedom. As part of this, we need to address the fact that QCMD does not explicitly define the "non-quasicentroid" modes, and even if it did, the RPMD Hamiltonian expressed in such coordinates would not be separable [46]. Therefore we cannot achieve adiabatic separation by rescaling the masses of a subset of the ring-polymer degrees of freedom. Instead, we modify *all* of the masses, scaling the centroid mass by γ^{-2} and the non-centroid masses by the factor in Eq. (5.19). Alongside the mass-scaled ("fast") ring-polymer system we introduce a second ("slow") system that consists of the quasicentroids with unmodified physical masses. The two systems are propagated in parallel using a modification of the constrained integrator due to Leimkuhler and Matthews [110]. A propagation step begins with the thermostatting of the momenta:

O1. Propagate the quasicentroid momenta $\overline{\mathbf{P}}$ for half a time step ($\Delta t/2$) under the action of a Langevin thermostat.

O2. Propagate the bead momenta $\mathbf{p}$ for $\Delta t/2$ under the path-integral Langevin (PILE) thermostat [92], followed by RATTLE [109] to constrain the quasicentroid components.

The momenta are then updated according to the forces acting on the system:

B1. Propagate $\overline{\mathbf{P}}$ for $\Delta t/2$ under the quasicentroid forces.

B2. Propagate $\mathbf{p}$ for $\Delta t/2$ under the forces derived from the ring-polymer potential $W_N(\mathbf{q})$, followed by RATTLE.

Then, the positions are updated:

A1. Propagate the quasicentroid positions $\overline{\mathbf{Q}}$ for a full time step Δt according to the current values of the momenta $\overline{\mathbf{P}}$.

A2. Propagate the bead positions $\mathbf{q}$ for Δt according to the current values of $\mathbf{p}$, followed by SHAKE [108], which constrains the ring-polymer geometry to be consistent with the quasicentroid configuration $\overline{\mathbf{Q}}$ at the end of step A1.

The propagation step is concluded by executing B1–B2 using the forces evaluated at the updated positions, followed by O1–O2. A useful feature of this algorithm is that it requires explicit forces only on the quasicentroids (B1) and the bead coordinates (B2), but does *not* require explicit forces on the non-quasicentroid modes. This new adiabatic QCMD (AQCMD) algorithm reduces to ACMD in the special case that the "quasicentroid coordinate" is the ring-polymer centroid, which leads us to suppose that the two algorithms have similar convergence properties.

5.2 Gaseous water

Given the quasicentroid coordinates and forces in Sections 5.1.1 and 5.1.2, we can now perform a QCMD simulation of gaseous water. We haven chosen the Partridge–Schwenke potential to describe the internal forces [111], together with the corresponding dipole-moment function [112] to calculate the infrared absorption spectrum.

There are no external forces acting on the water molecules in our simulations, so in the notation of Eq. (5.10), $-\partial V(\mathbf{q})/\partial \mathbf{q}_l^{(\alpha)} = \mathbf{f}_{\mathrm{int},l}^{(\alpha)}$. The mean-field averages of the internal forces expressed in terms of $\boldsymbol{\xi} = (\xi_1, \xi_2, \xi_3) = (R_1, R_2, \Theta)$ depend only on these coordinates, and not on the position of the centre of mass or the molecular orientation. We may therefore write

$$\begin{aligned} \langle \ldots \rangle_{\boldsymbol{\xi}} &= \frac{1}{\overline{z}_0(\boldsymbol{\xi})} \int \mathrm{d}\mathbf{q}' \, \mathrm{e}^{-\beta W_N(\mathbf{q}')} (\ldots) \, \delta(\boldsymbol{\xi}' - \boldsymbol{\xi}), \\ \overline{z}_0(\boldsymbol{\xi}) &= \int \mathrm{d}\mathbf{q}' \mathrm{e}^{-\beta W_N(\mathbf{q}')} \, \delta(\boldsymbol{\xi}' - \boldsymbol{\xi}), \end{aligned} \tag{5.20}$$

where $(\ldots)$ are the $\overline{f}^{(R_1)}$, $\overline{f}^{(R_2)}$, and $\overline{f}^{(\Theta)}$ defined in Eqs. (5.11) to (5.13). We pre-calculate the mean-field averages on a grid and convert them into Cartesian representation as per Eq. (5.14). Using cubic splines to interpolate between grid points, we propagate an ensemble of QCMD trajectories subject to these mean-field forces, and calculate the ACF

$$\overline{C}_{\mu\mu}(t) = \frac{1}{(2\pi\hbar)^9} \int \mathrm{d}\overline{\mathbf{P}} \int \mathrm{d}\overline{\mathbf{Q}}\, \mathrm{e}^{-\beta \overline{H}(\overline{\mathbf{P}},\overline{\mathbf{Q}})}\, \boldsymbol{\mu}(\overline{\mathbf{Q}}) \cdot \boldsymbol{\mu}(\overline{\mathbf{Q}}_t), \tag{5.21}$$

with

$$\overline{H}(\overline{\mathbf{P}}, \overline{\mathbf{Q}}) = \sum_{\alpha} \left[\overline{\mathbf{P}}^{(\alpha)}\right]^2 / 2m_\alpha + \overline{F}(\overline{\mathbf{Q}}), \tag{5.22}$$

where $\overline{F}(\overline{\mathbf{Q}})$ is the free energy obtained by doing work with the approximate mean-field forces. As in Sections 3.3 and 4.3, we damp the TCF before calculating its Fourier transform, this time using a Hann window [98] of width $w = 750$ fs [see Eq. (C.9)]. This produces the QCMD IR absorption spectrum, which we compare to the corresponding exact quantum, CMD, and TRPMD simulation results. The exact spectra are calculated using the DVR3D package of Tennyson *et al.* [120], and the path-integral results are obtained using standard PIMD techniques, as detailed in Appendix C.3. A comparison with Matsubara dynamics is not possible because the sign problem is too severe.

From Figure 5.2, we see that QCMD works extremely well for gas-phase water. The overall agreement with the exact quantum results is excellent, even at 150 K, where there is again no sign of a curvature problem. There are small differences between the QCMD and quantum spectra: the QCMD bend ($\approx$1600 cm^{-1}) and stretch ($\approx$3800 cm^{-1}) have different internal structures from those in the exact spectrum, and the stretch is blueshifted by about 60 cm^{-1}. The main cause of these differences is most likely the neglect of quantum coherence by QCMD. Note that the positions of the TRPMD bands are very close to those of the QCMD bands, implying that, as expected, TRPMD gives a good description of the short-time dynamics of gas-phase water.

As in the two-dimensional model, the gas-phase water QCMD distributions remain compact at inner turning points because there are no quasicentroid-constrained instantons. Figure 5.3 compares the distributions at inner turning points of an "extreme" QCMD and CMD trajectory at 150 K. As in the two-dimensional case, the QCMD distribution remains localised, whereas the CMD distribution spreads around a centroid-constrained instanton. This artefact breaks the approximate axial symmetry around the OH bond, causing the mean-field ring-polymer distribution to become bimodal ("banana-shaped").

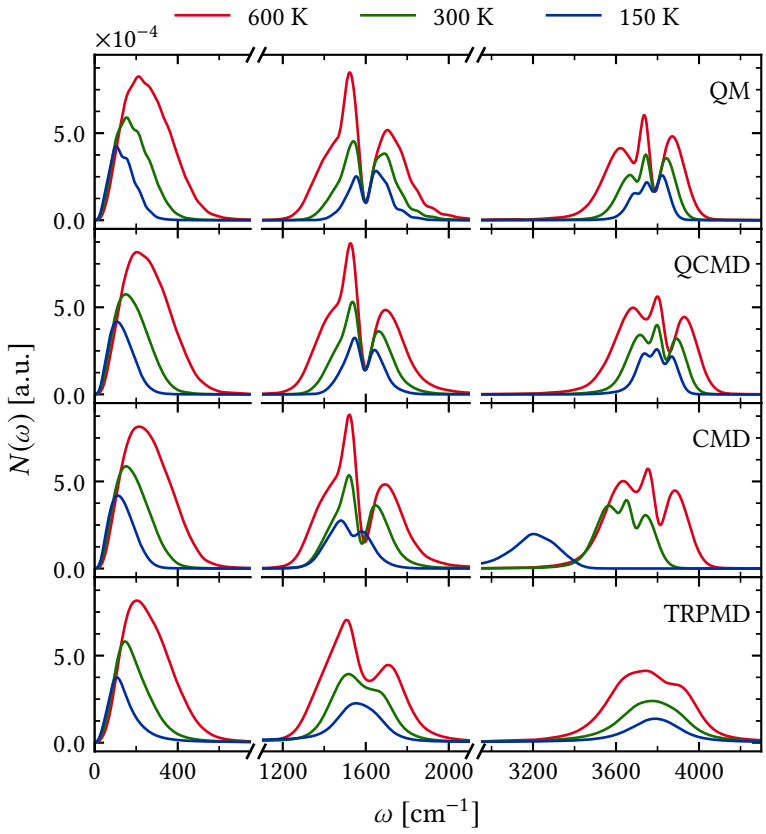

Figure 5.2 Simulated rovibrational absorption spectra for gaseous water, obtained after damping the time-correlation function with a 750 fs Hann window. The QCMD results were calculated using the bond-angle centroids of Section 5.1.1, and show good agreement with the exact quantum results (QM), with no sign of the redshift and broadening seen in the CMD stretch. Note that the absorption intensities are scaled by a factor of 4.5 for $\omega > 1200$ cm^{-1}.

To assess the magnitude of the approximations that QCMD makes to the exact quantum Boltzmann distribution, we once again consider the thermal averages of some static properties. Comparison of the average QCMD OH bond lengths with those obtained using standard PIMD shows very small differences (0.1% at 150 K), indicating that, as for the two-dimensional model, the approximate distribution in Eq. (5.22) is very close to the exact quantum Boltzmann distribution. Note that, since the Partridge–Schwenke dipole moment is non-linear [112], neither CMD nor QCMD are exact in the $t \to 0$ limit for the quantum KTCF [16, 104], and that both methods neglect the Matsubara fluctuation terms necessary to completely describe the dipole-moment dynamics at low temperatures [81, 82].

Before continuing to simulations of water in the condensed phase, we use this opportunity to test the AQCMD algorithm on gas-phase water at 150 K. We find that a value of $\gamma = 64$ is sufficient to reproduce the spectrum obtained by interpolating the force on a grid. The adiabatic simulation requires a time step of $\Delta t = 0.1/\gamma$ fs, i.e. γ times smaller than what would have been used to propagate the dynamics without the mass scaling. We note that the same values of γ and Δt are required to converge ACMD at this temperature, and hence

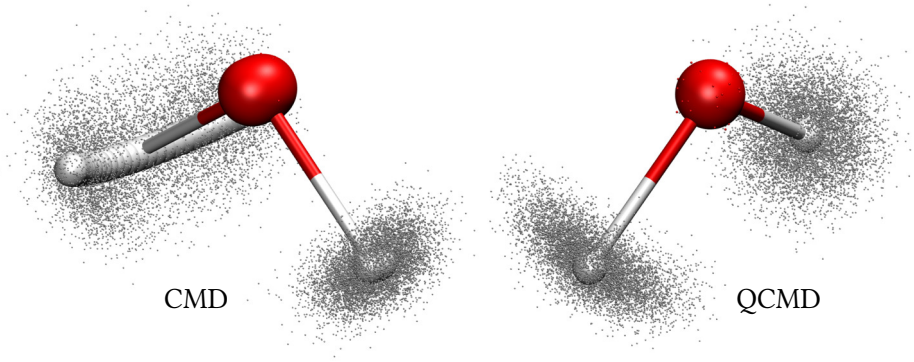

Figure 5.3 Ring-polymer distributions (dots) at the inner turning points of CMD and QCMD trajectories corresponding to very short (but thermally accessible) OH bond lengths, taken from the gas-phase water simulations at 150 K. The CMD distribution fluctuates about an artificial instanton (spheres), whereas the QCMD distribution fluctuates about a point.

that the AQCMD algorithm uses approximately the same amount of CPU time as the ACMD algorithm, since most of the time is spent evaluating the forces on the ring-polymer beads.

In condensed-phase simulations, converged ACMD results can be obtained at significantly lower adiabatic separation [10, 104], provided that the strength of the thermostat acting on the non-centroid modes is carefully tuned [16]. This approach is known as partially-adiabatic CMD (PA-CMD). At this stage we do not attempt a similar partially-adiabatic implementation of QCMD and view it as an important step in future methodological development.

5.3 Liquid water and ice

Given the promising results from QCMD simulations of gaseous water, we are encouraged to apply our method to condensed-phase simulations. This time we use the q-TIP4P/F potential energy surface and the associated linear dipole moment [11], which allows us to draw a direct comparison with the results of a previous study comparing path-integral approximations of the rovibrational spectrum for this model system [16].

5.3.1 Overview of the spectrum

We run CMD, TRPMD, and QCMD simulations, calculating the ACF of the net dipole moment

$$\boldsymbol{\mu} = \sum_{\alpha} \boldsymbol{\mu}_{\alpha},$$

and its time-derivative $\dot{\boldsymbol{\mu}}$, where the index α runs over the molecules in the simulation box. The TCFs are converted into infrared absorption spectra according to [9, 10]

$$n(\omega)\sigma(\omega) = \frac{\beta}{6cV\epsilon_0}\int_{-\infty}^{\infty} dt\, \mathrm{e}^{-\mathrm{i}\omega t} C_{\dot{\boldsymbol{\mu}}\cdot\dot{\boldsymbol{\mu}}}(t) f(t) = \frac{\beta\omega^2}{6cV\epsilon_0}\int_{-\infty}^{\infty} dt\, \mathrm{e}^{-\mathrm{i}\omega t} C_{\boldsymbol{\mu}\cdot\boldsymbol{\mu}}(t) f(t), \tag{5.23}$$

where V is the volume of the simulation cell, $n(\omega)$ is the refractive index, $\sigma(\omega)$ is the absorption cross-section, and $f(t)$ is the Hann window function that dampens the tail of the TCF and reduces ringing artefacts [98]. The widths of the Hann windows used in the different temperature regimes are given in the caption to Figure 5.4.

To compute the QCMD spectra we use the AQCMD algorithm described in Section 5.1.3 as a means to calculate the mean-field forces on the fly. Converged AQCMD results are obtained for $\gamma = 8$ at 600 K, and $\gamma = 32$ at 300 K. At 150 K, we consider adiabaticity parameters up to $\gamma = 128$, until the positions of the peaks and the $t \to 0$ limit of the dipole-derivative TCFs are both converged. At the highest adiabatic separation, the intensity of the stretch peak may not yet be converged (see Appendix C.2), but preliminary calculations with the improved quasicentroid torque estimator suggest otherwise. With these values of γ, the QCMD calculations are approximately 2, 8, and 32 times more expensive than the corresponding CMD calculations, which use the partially adiabatic algorithm [10, 104] and hence smaller values of γ. Further simulation details for this and other path-integral calculations in this section can be found in Appendix C.3.

At 600 K, the QCMD spectra are in very close agreement with TRPMD and CMD (Figure 5.4). Measured from the peak maximum, the QCMD OH stretch at 3600 cm^{-1} is blueshifted by about 15 cm^{-1} relative to CMD and TRPMD. The bend at 1600 cm^{-1} and the libration peak at 500 cm^{-1} are almost identical in all three methods.

At 300 K, noticeable differences emerge due to the curvature problem in CMD and the peak broadening in TRPMD, although these problems are less severe than in the gas-phase at this temperature [16, 85, 86]. The CMD stretch peak is redshifted relative to TRPMD by about 50 cm^{-1}; the QCMD stretch peak is blueshifted by about 20 cm^{-1}. The bend peaks are in good agreement for all three methods. The libration band in QCMD is slightly redshifted; this is almost certainly because of the approximation we made to the quasicentroid torque in Eq. (5.16).

In 150 K ice, there are major differences between the three sets of results, mainly in the stretch region. The curvature problem is strong, artificially broadening and redshifting the CMD stretch by more than 100 cm^{-1}. The TRPMD stretch is also severely broadened. In contrast, the QCMD stretch is sharp, with resolved symmetric and antisymmetric bands.

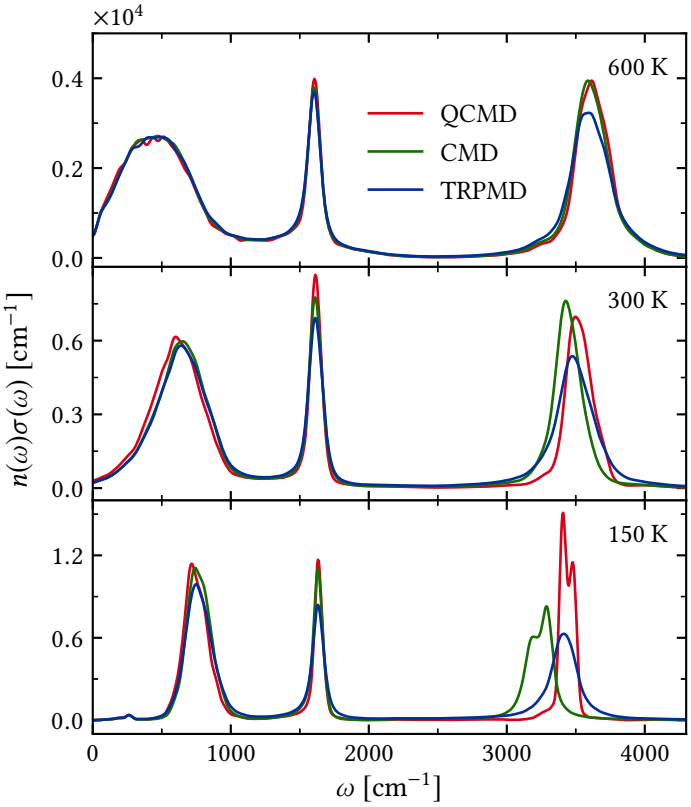

Figure 5.4 Simulated infrared absorption spectra for q-TIP4P/F water, at 600 K (compressed liquid), 300 K (liquid), and 150 K (ice I_h), obtained by damping the time-correlation function with a Hann window of width w = 600 fs at 600 and 300 K, and w = 800 fs at 150 K. The bond-angle centroids used in the QCMD simulations appear to have eliminated the redshifts and broadening seen in the CMD stretch band at 300 and 150 K.

The splitting of the stretch band is a feature specific to the q-TIP4P/F potential and is also observed in classical simulations, but not in experimentally measured spectra [121, 122]. Using a shorter Hann window of 500 fs to coalesce the QCMD stretch peaks (not shown) gives a QCMD stretch that is blueshifted by about 10 cm^{-1} with respect to TRPMD, and is more than twice as intense at its maximum. Note that, as mentioned above, the intensity of the QCMD stretch may not have converged with respect to γ. All three methods remain in close agreement in the libration and bend regions, except for a small redshift in the QCMD libration band, comparable to what we see at 300 K.

5.3.2 Stretch region

To better assess the performance of QCMD in the stretch region (> 2000 cm^{-1}), we compare our results with two other methods: the coloured-noise version of TRPMD, developed by Rossi *et al.* [84], and the local monomer approximation (LMon) of Bowman and co-workers [16, 123–126]. Both methods are expected to do well in the stretch region of the spectrum, but suffer from artefacts at lower frequencies.

In coloured-noise TRPMD, the white-noise PILE thermostat used in most TRPMD calculations is replaced by a generalised Langevin equation (GLE) thermostat that is designed to minimise the dynamical disturbance to the centroids at certain pre-tuned frequencies [84]. Using the GLE(C) parametrisation of the thermostat in Ref. [84] (along with the other simulation parameters in this reference), we propagated eight independent 100 ps TRPMD+GLE(C) trajectories at 300 and 150 K using the i-PI package due to Ceriotti and co-workers [127]. The resulting spectra in the stretch region are shown in Figure 5.5; the low-frequency parts of the spectra, which are corrupted by the thermostat, are shown in Appendix C.3.2.

In the LMon method, the solid or liquid is equilibrated using standard PIMD techniques, then the Schrödinger equation for the nuclei is solved for each monomer independently, with all degrees of freedom except for the internal and a few intramolecular modes of the monomer held fixed [123–126]. Here we use the results of previous LMon calculations [16], in which the PIMD equilibration was done using the same simulation parameters as in the TRPMD calculations of Section 5.3.1. The calculations were performed using a four-mode approximation (LMon-4), in which the internal modes of the water molecule are in turn coupled to each of its three librational modes. We convolve the raw data from these calculations with the same time windows as used in the QCMD calculations (see Appendix C.3), to obtain the spectra shown in Figure 5.5. The approximate treatment of the intermolecular modes means that LMon-4 gives a relatively poor description of the spectrum at 600 K (not shown) and of the libration at all temperatures (see Appendix C.3.2).

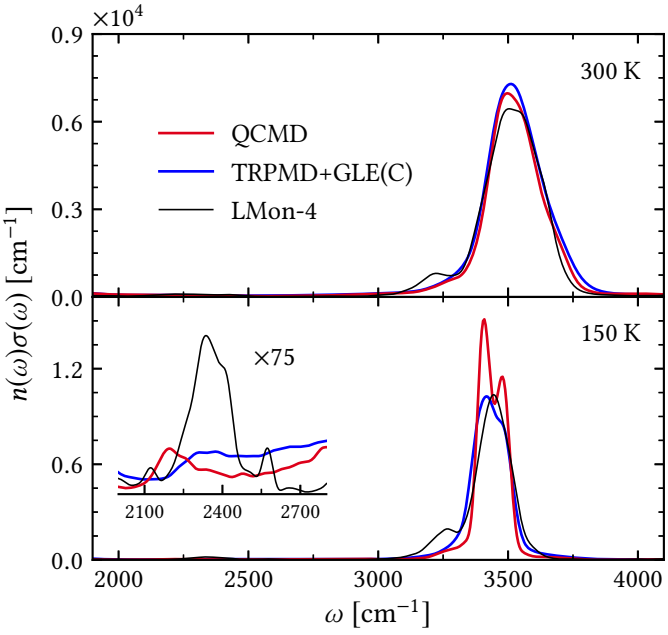

Figure 5.5 The stretch region of the infrared absorption spectra from the same QCMD simulations as in Figure 5.4, compared with TRPMD+GLE(C) spectra calculated as in Ref. [84], and LMon-4 spectra taken from Ref. [16]. The inset magnifies the combination-band part of the spectrum.

The agreement between the QCMD and TRPMD+GLE(C) stretch peaks is excellent: at 300 K the peaks are almost identical; at 150 K the TRPMD+GLE(C) peaks line up with the QCMD peaks, but are somewhat broader, with the bifurcation just visible. This broadening is to be expected since the thermostat couples more strongly to the centroid at lower temperatures. There is probably some cancellation of errors between these two sets of results, as the QCMD method makes a number of static approximations (see Sections 5.1.2 and 5.1.3), and the GLE(C) thermostat interferes strongly with the libration, which is coupled to the dynamics of the stretch modes. One piece of evidence for such errors is that the 300 K QCMD peak is slightly less intense than the TRPMD+GLE(C) peak, whereas one would expect the reverse to be true. Nevertheless the agreement between QCMD and TRPMD+GLE(C) in the stretch region is remarkable, suggesting that both methods give excellent approximations to that part of the spectrum.

The QCMD and LMon-4 results are also in good agreement in the stretch region (Figure 5.5). Clearly one cannot use LMon-4 as a quantum benchmark, since it includes only a few degrees of freedom in the monomer dynamics, which is probably why it does not reproduce the bifurcation of the stretch peak. Even so, we think the comparison in Figure 5.5 highlights an important weakness in the QCMD approach, shared by CMD [128] and TRPMD [16]. The LMon-4 spectrum gives a libration-bend combination band at roughly 2300 cm^{-1} (see the inset of Figure 5.5) and a Fermi resonance that forms a shoulder in the stretch peak at 3200 cm^{-1}. Both of these are much more intense than the corresponding features in the QCMD, CMD and TRPMD spectra. While we cannot say how well the LMon-4 calculations describe these features, it seems highly likely that QCMD, CMD and TRPMD grossly underestimate their intensities. This is not surprising, as we expect such features to depend strongly on Matsubara fluctuations [81, 82] and possibly on quantum coherence—effects which QCMD, CMD and TRPMD neglect.

5.3.3 Static properties

On the basis of the simulated infrared spectra, it seems likely that QCMD approximates the quantum Boltzmann distribution nearly as well as it does in the gas phase and in the two-dimensional model. However, the condensed-phase calculations rely on additional approximations to the quantum Boltzmann distribution: the mean-field forces are calculated using approximate estimators, especially the external torques (see Section 5.1.2), and the AQCMD algorithm only samples the exact mean-field distribution in the limit $\gamma \to \infty$.

To test the magnitude of these static approximations, we compare the AQCMD radial distribution functions (RDFs) for the liquid at 300 K and ice at 150 K with the exact quantum

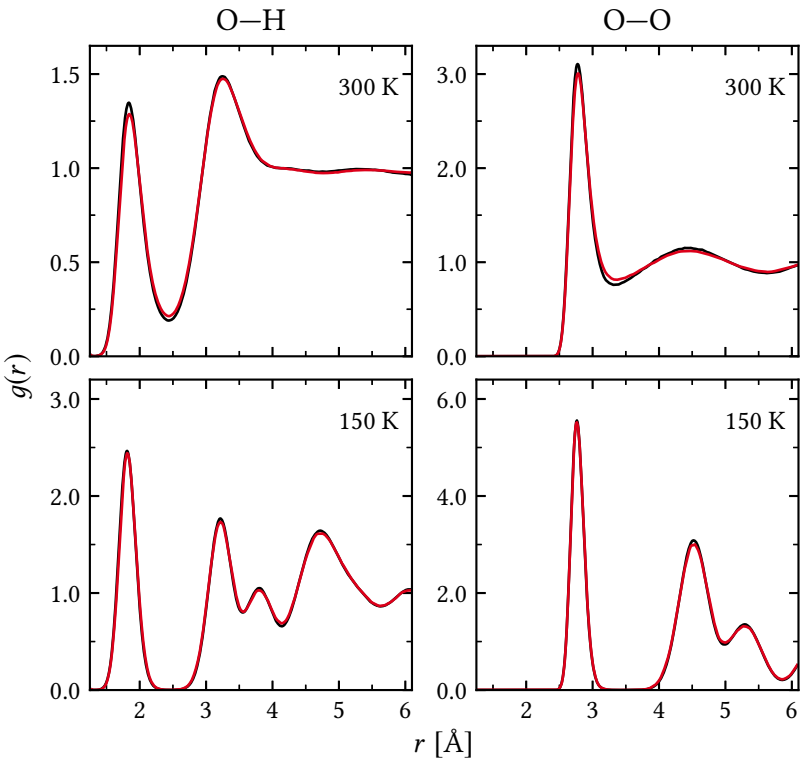

Figure 5.6 Simulated oxygen–hydrogen O—H and oxygen–oxygen O—O radial distribution functions (RDFs) for q-TIP4P/F water, calculated using QCMD (red) and standard PIMD (black). Hydrogen–hydrogen RDFs (not shown) are in similarly close agreement. The QCMD results are given for an adiabatic separation of $\gamma = 64$ at 300 K and $\gamma = 128$ at 150 K. Only the intermolecular part of the distribution is shown for O—H; the intramolecular distributions obtained using the two methods agree to within graphical accuracy.

RDFs from PIMD simulations (see Figure 5.6). As expected, the AQCMD RDFs are close to the exact values, although there are small errors at 300 K, indicating that AQCMD gives a slightly less structured liquid than it should. Given that the AQCMD RDFs are in almost perfect agreement with the exact values for 150 K ice, and that the intramolecular peaks in the O–H RDF (not shown) agree to within graphical accuracy, we think that the small errors at 300 K are mainly the result of approximating the monomer torques by Eq. (5.16). A small contribution to the errors might also arise from incomplete adiabatic separation: increasing γ from 32 (not shown) to 64 brings the AQCMD RDF at 300 K closer to the PIMD reference.

These results suggest that QCMD gives an excellent approximation to the quantum Boltzmann distributions in water and ice, except for small errors in the long-range correlations at 300 K, which are most likely due to the approximation made to the quasicentroid torque estimator in Eq. (5.16). This approximation is also thought to cause the small redshift in the

libration band of the infrared spectrum at 300 and 150 K (see Figure 5.4). An improved torque estimator, such as the one proposed at the end of Section 5.1.2, may be able to reduce these small errors [117].

Chapter 6

Conclusions and further work

In this work we have set out to improve our understanding of the path-integral methods designed to combine exact quantum Boltzmann statistics with classical dynamics. Much progress in this direction has been made by Althorpe and co-workers [81–83, 88], who developed Matsubara dynamics—a rigorous mathematical framework within which many of the approximate methods discussed in this thesis can be derived. We have built on their work by proposing an alternative, mean-field formulation of Matsubara dynamics, presented in Chapter 3. The improved convergence properties of the new formulation have allowed us to perform numerical simulations that have yielded new insight into the properties of the CMD method. Our conclusions have lead us to develop a new path-integral approximation (QCMD), which we have shown in Chapter 4 to correct the failings of CMD in simulations of the rovibrational dynamics of a two-dimensional model system. We have subsequently used QCMD in Chapter 5 to simulate different phases of water, showing that our new method offers the most accurate approximation of its vibrational fundamental features compared to other quantum-Boltzmann-conserving path-integral methods available at the time of writing.

We have started our work by reformulating Matsubara dynamics as a mean-field approximation to the quantum Kubo-transformed time-correlation function (see Section 3.1). The original derivation by Hele *et al.* [81] arrived at a classical path-integral dynamics by mean-fielding the jagged collective path coordinates (non-Matsubara modes), while restricting the dependence of the external potential to only the smooth coordinates (Matsubara modes). This "truncated" formulation describes the quantum statistics exactly, but *only* in the limit of infinitely many Matsubara modes, which has prevented the application of Matsubara dynamics to numerical simulations of all but the simplest potentials [81–83]. In our formulation, we do not make any assumptions as to the functional form of the external potential, thus retaining an exact description of the quantum Boltzmann distribution for any number of the remaining

Matsubara coordinates. This has enabled us to converge some mean-field Matsubara dynamics simulations of a chemically relevant two-dimensional model system introduced in Section 3.3, which we have been unable to do using the original formulation. The new results allow us to gauge the effect of quantum coherence on the vibrational dynamics of our model system; even for this low-dimensional potential they appear to be minor, slightly sharpening the vibrational fundamental band and shifting it to the red by about 20 cm^{-1}.

Our results also suggest that at sufficiently high temperatures (around 800 K for this model) CMD comes very close to fully converged Matsubara dynamics, singling it out for use in spectroscopic simulations. However, as discussed in Section 3.3.3, low-temperature CMD suffers from the curvature problem, which we find can be divided into two distinct regimes. In the "shallow curvature" regime CMD predicts the correct line shapes (compared to Matsubara dynamics), and its high-frequency peaks shift to the red relatively slowly as the temperature is lowered. At this point the three lowest modes in Matsubara dynamics are sufficient to correctly describe the main spectral features. At lower temperatures still, in the "deep curvature" regime, CMD line shapes deteriorate, and the redshift rapidly increases. In this regime many more Matsubara modes are needed.

We have found that the deep curvature regime is connected to the formation of artificial instantons in CMD. At low temperatures, a ring polymer with a centroid constrained to a (thermally accessible) position around the inner turning point can lower its energy by expanding into a delocalised minimum-energy configuration (instanton). In this case, the beads of the centroid-constrained ring polymer no longer fluctuate about the centroid, but rather about the instanton, leading to an artificially softened mean-field force. Bearing in mind that CMD agrees with Matsubara dynamics in the high-temperature regime, and that only a few Matsubara modes are required for an accurate description of the vibrational fundamentals in the shallow curvature regime, we conclude that a mean-field approximation to the exact KTCF can lead to accurate rovibrational spectra, provided that the approximation gives rise to mean-field distributions that are always centred on the dynamical (non-mean-fielded) coordinate.

One way of achieving this is to release more Matsubara modes from the mean field, which introduces a phase and creates a sign problem. Releasing any *linear combination* of Matsubara modes has similar consequences. This has motivated us to construct a mean-field approximation to Matsubara dynamics based around *curvilinear* coordinates (Section 4.2.1). We have shown that this approximation can lead to real, phase-free dynamics, provided that the dynamical coordinates are invariant under imaginary time translation and reversal. An upper bound on the number of such coordinates is just over half the number of Matsubara

modes (see Appendix B.2.2), and so the approach has a considerable degree of flexibility. For now we have chosen to keep a single dynamical coordinate per physical degree of freedom, basing our mean-field dynamics on curvilinear centroids or *quasicentroids* (Section 4.2.2).

We have named our dynamical coordinates "quasicentroids" because they are always close to (but not on top of) the Cartesian centroids. This proximity allows us to make several approximations to the mean-field dynamics of the quasicentroids, which we have shown to be minor, and which greatly simplify the practical implementation of QCMD (Section 4.3). In particular, we have assumed that the mean-field quasicentroid Hamiltonian is separable, and that the contributions to the mean-field forces are largely from the external potential. This has allowed us to use a standard symplectic algorithm (velocity Verlet [49]) to integrate the quasicentroid dynamics, and has enabled us to calculate the approximate mean-field forces in simulations of gaseous and condensed-phase water without needing to define a complementary set of "non-quasicentroid" coordinates.

The drawbacks of having to make these assumptions are far outweighed by the robustness of the QCMD mean-field approximation. The quasicentroid coordinates have been chosen because they force the ring-polymer distribution to remain compact at all times, so that the quasicentroid approximately coincides with the mode[1] of the distribution. This fixes the design flaw of CMD, preventing the formation of artificial instantons and overcoming the curvature problem. For our two-dimensional model, simulated QCMD fundamental bands are close to the exact quantum results at all the temperatures that we have tested (50–800 K), and are nearly on top of the Matsubara dynamics spectra. We have obtained similarly encouraging results for gaseous water (Section 5.2), where QCMD is seen to improve on the approximations derived from established path-integral methods.

For simulations in the condensed phase we have had to introduce a suitable set of rotational quasicentroid coordinates (vibrational and translational coordinates follow trivially from the results in Chapter 4). We have taken inspiration from molecular spectroscopy, defining the quasicentroid orientation in terms of an "Eckart-like" frame (Section 5.1.1). This definition rigorously minimises the spread of the mean-field distribution in the gas phase and appears to be near-optimal in the condensed phase.

We have tackled the issue of calculating mean-field forces on the fly by adapting the adiabatic CMD (ACMD) algorithm (Section 5.1.3). The resulting adiabatic QCMD algorithm (AQCMD) has similar convergence properties to ACMD and requires approximately the same amount of computational resources to produce converged infrared absorption spectra. There remains the important distinction that ACMD has a partially adiabatic variant (PA-CMD),

[1] Here we use the term "mode" in the statistical sense, rather than as in "normal mode".

which, in effect, interpolates between TRPMD and CMD [10, 104]. This method makes use of much smaller levels of adiabatic separation, reducing the simulation time to no more than several times that of TRPMD. It is not currently possible to formulate a partially adiabatic version of QCMD because we have not been able to implement a curvilinear analogue of TRPMD. To do this, we would have to define a *full* set of curvilinear coordinates (including the "non-quasicentroid" fluctuations) and integrate the corresponding non-separable equations of motion. This is a challenging problem that will have to be addressed in future development.

Despite the need for relatively high levels of adiabatic separation, the AQCMD algorithm is efficient enough to yield converged infrared spectra for liquid water and ice (Section 5.3), although the convergence of ice simulations is tentative. The calculations have required additional approximations to the mean-field forces, most notably to the quasicentroid torque (Section 5.1.2). Even so, analysis of static properties calculated with QCMD suggests that these approximations are relatively minor, and can likely be further reduced by improving the torque estimator as described at the end of Section 5.1.2. Apart from a small redshift in the libration peak, QCMD simulations appear to give an excellent approximation to the exact spectra, as far as can be judged from comparison to other path-integral methods and approximate wavefunction-based calculations (LMon-4, see Section 5.3.2). Work is currently underway to improve the AQCMD algorithm, which we hope will soon allow us to run simulations using more realistic (and expensive) water potentials, such as MB-pol [20, 129]. With these potentials we could directly compare simulated spectra with experimental results, thus getting both an exact reference, and an opportunity to use our method in a predictive and interpretative capacity.

It remains to address the two major weaknesses of QCMD. First, similarly to the path-integral dynamics approximations introduced in Chapter 2, QCMD is a (quasi-)centroid-following method that only provides a reliable approximation to the dynamics of a small (centroid-like) subset of the Matsubara coordinates. Because of this, QCMD, as well as CMD and (T)RPMD, generally give poor results for non-linear operators, which depend explicitly on the dynamics of the Matsubara fluctuation modes. The same is true for overtones and combination bands, which are strongly influenced by the dynamical coupling of the centroids to the non-centroid fluctuations. The only way around this is to use a method that provides a more accurate description of these fluctuations. We hope that the development of such a practical method can be aided by the theory of mean-field approximations presented in Chapter 4.

Nevertheless, it should be noted that while polarisable dipole-moment surfaces such as MB-pol are highly non-linear functions of position, classical, CMD, and TRPMD simulations

of the vibrational fundamental peak intensities show good overall agreement with experiment [17, 128, 130]. This suggests that the main function of the non-linearity is, in this case, to describe the inhomogeneous distribution of local dipole moments, each of which fluctuates almost linearly. We thus expect QCMD calculations using such dipole-moment surfaces to still produce accurate descriptions of fundamental features, despite the reservation concerning general non-linear operators.

The second weakness of QCMD in its current form is that it is specific to systems comprised of bent triatomic molecules. The question of how it can be generalised to other systems is equivalent to asking how readily we can identify collective degrees of freedom that give rise to compact ring-polymer distributions. Building on the ideas of Chapter 5, generalisations to systems comprised of small, semi-rigid molecules should be relatively straightforward. In fact we have recently started developing an approach that should be able to tackle most non-dissociative molecular systems. However our ultimate goal is an algorithm that can identify and follow the optimal collective bead coordinate on the fly, automatically ensuring the compactness of the mean-field distribution, and thus giving the best mean-field approximation to Matsubara dynamics.

Appendix A

Mean-field Matsubara dynamics

A.1 Path-integral time-correlation function

We derive the path-integral representation of the Kubo-transformed time-correlation function following previous work by Althorpe and co-workers [81, 88]. For the sake of brevity, we drop the normalisation of the TCF by the partition function Z [see Eq. (2.20)] in this and the following section. First, we convert the imaginary-time integral in the Kubo transform of Eq. (2.21) into a Riemann sum,

$$C_{AB}(t) = \lim_{N\to\infty} \frac{1}{N} \sum_{l=1}^{N} \int_{-\infty}^{\infty} \mathrm{d}q \, \left\langle q \left| \left[\mathrm{e}^{-\beta_N \hat{H}}\right]^l \hat{A} \left[\mathrm{e}^{-\beta_N \hat{H}}\right]^{N-l} \mathrm{e}^{+\mathrm{i}\hat{H}t/\hbar} \hat{B} \mathrm{e}^{-\mathrm{i}\hat{H}t/\hbar} \right| q \right\rangle. \tag{A.1}$$

Next, using the cyclic permutation property of the trace, we rewrite the sum as

$$C_{AB}^{[N]}(t) = \frac{1}{N} \sum_{l=1}^{N} \int \mathrm{d}q \, \left\langle q \left| \hat{A} \left[\mathrm{e}^{-\beta_N \hat{H}}\right]^{N-l} \mathrm{e}^{+\mathrm{i}\hat{H}t/\hbar} \hat{B} \mathrm{e}^{-\mathrm{i}\hat{H}t/\hbar} \left[\mathrm{e}^{-\beta_N \hat{H}}\right]^l \right| q \right\rangle. \tag{A.2}$$

From here onwards we omit the integration bounds. Assuming for the sake of simplicity that both $\hat{A}$ and $\hat{B}$ are functions of the position operator $\hat{q}$, each term in the sum can be cast in a "ring-polymerised" form,

$$\begin{aligned} \int \mathrm{d}q \, \left\langle q \left| \hat{A} \left[\mathrm{e}^{-\beta_N \hat{H}}\right]^{N-l} \mathrm{e}^{+\mathrm{i}\hat{H}t/\hbar} \hat{B} \mathrm{e}^{-\mathrm{i}\hat{H}t/\hbar} \left[\mathrm{e}^{-\beta_N \hat{H}}\right]^l \right| q \right\rangle = \int \mathrm{d}x_N \int \mathrm{d}x_l \int \mathrm{d}x_l' \int \mathrm{d}z_l \, A(x_N) B(z_l) \times \\ \left\langle x_N \left| \left[\mathrm{e}^{-\beta_N \hat{H}}\right]^{N-l} \right| x_l' \right\rangle \left\langle x_l' \left| \mathrm{e}^{+\mathrm{i}\hat{H}t/\hbar} \right| z_l \right\rangle \left\langle z_l \left| \mathrm{e}^{-\mathrm{i}\hat{H}t/\hbar} \right| x_l \right\rangle \left\langle x_l \left| \left[\mathrm{e}^{-\beta_N \hat{H}}\right]^l \right| x_N \right\rangle, \end{aligned} \tag{A.3}$$

where we relabel the original integration variable $q \to x_N$, insert resolutions of the identity in terms of x'_l, z_l and x_l (in that order, left to right) between each pair of imaginary- and real-time propagators, and act with $\hat{A}$ and $\hat{B}$ to obtain the factors $A(x_N)$ and $B(z_l)$. We then insert a set of resolutions of the identity

$$\int \mathrm{d}x_k \int \mathrm{d}x'_k \int \mathrm{d}z_k \, |x'_k\rangle\langle x'_k|\mathrm{e}^{+\mathrm{i}\hat{H}t/\hbar}|z_k\rangle\langle z_k|\mathrm{e}^{-\mathrm{i}\hat{H}t/\hbar}|x_k\rangle\langle x_k| \tag{A.4}$$

between each pair of adjacent factors of $\mathrm{e}^{-\beta_N \hat{H}}$, and

$$\int \mathrm{d}x'_N \int \mathrm{d}z_N \, |x'_N\rangle\langle x'_N|\mathrm{e}^{+\mathrm{i}\hat{H}t/\hbar}|z_N\rangle\langle z_N|\mathrm{e}^{-\mathrm{i}\hat{H}t/\hbar} \tag{A.5}$$

immediately before $|x_N\rangle$ in Eq. (A.3). This leads to the highly symmetric expression

$$\int \mathrm{d}^N\mathbf{x} \int \mathrm{d}^N\mathbf{x}' \int \mathrm{d}^N\mathbf{z} \, A(x_N)B(z_l) \prod_{k=1}^{N} \left[\langle x_{k+1}|\mathrm{e}^{-\beta_N \hat{H}}|x'_k\rangle\langle x'_k|\mathrm{e}^{+\mathrm{i}\hat{H}t/\hbar}|z_k\rangle\langle z_k|\mathrm{e}^{-\mathrm{i}\hat{H}t/\hbar}|x_k\rangle \right], \tag{A.6}$$

where $\int \mathrm{d}^N\mathbf{x} = \int \mathrm{d}x_1 \cdots \int \mathrm{d}x_N$, and similarly for $\mathbf{x}'$ and $\mathbf{z}$. Writing each of the terms in Eq. (A.1) in this way, we note that the result is invariant under the cyclic permutation of the indices $k = 1, \ldots, N$, allowing us to replace $A(x_N)$ with $A_N(\mathbf{x})$ as defined in Eq. (2.39). We then transform the integration variables from $\mathbf{x}$ and $\mathbf{x}'$ to

$$q_k = \left(x_l + x'_l\right)/2 \qquad \text{and} \qquad \Delta_k = x'_l - x_l, \tag{A.7}$$

to get

$$\begin{aligned} C_{AB}^{[N]}(t) = \int \mathrm{d}^N\mathbf{q} \int \mathrm{d}^N\mathbf{\Delta} \int \mathrm{d}^N\mathbf{z} \, A_N(\mathbf{q} - \mathbf{\Delta}/2)B_N(\mathbf{z}) \times \\ \prod_{l=1}^{N} \Big[\langle q_{l+1} - \Delta_{l+1}/2|\mathrm{e}^{-\beta_N \hat{H}}|q_l + \Delta_l/2\rangle \times \\ \langle q_l + \Delta_l/2|\mathrm{e}^{+\mathrm{i}\hat{H}t/\hbar}|z_l\rangle\langle z_l|\mathrm{e}^{-\mathrm{i}\hat{H}t/\hbar}|q_l - \Delta_l/2\rangle \Big] \end{aligned} \tag{A.8}$$

with $B_N(\mathbf{z})$ defined analogously to $A_N(\mathbf{x})$. Lastly, we expand the double sum

$$A_N(\mathbf{q} - \mathbf{\Delta}/2)B_N(\mathbf{z}) = \frac{1}{N^2} \sum_{j=1}^{N} \sum_{l=1}^{N} A(q_j - \Delta_j/2)B(z_l) \tag{A.9}$$

and consider the $N(N-1)$ off-diagonal terms ($j \neq l$). For these, integration over z_j in Eq. (A.8) can be performed analytically, producing a factor of $\delta(\Delta_j)$ and allowing $A(q_j - \Delta_j/2)$ to be

replaced with $A(q_j)$. This simplification cannot be made for the N remaining diagonal terms ($j = l$), each of which upon integration evaluates to the "right" time-correlation function,

$$C_{AB}^{[R]}(t) = \mathrm{Tr}[\hat{A}\mathrm{e}^{-\beta\hat{H}}\mathrm{e}^{\mathrm{i}\hat{H}t/\hbar}\hat{B}\mathrm{e}^{-\mathrm{i}\hat{H}t/\hbar}]. \tag{A.10}$$

The summed contribution of such terms to Eq. (A.8) scales as N^{-1}, and can therefore be neglected in the limit as $N \to \infty$. This leads to the final path-integral representation of the Kubo-transformed TCF,

$$\begin{aligned} C_{AB}(t) = \lim_{N\to\infty} \int \mathrm{d}^N\mathbf{q} \int \mathrm{d}^N\mathbf{\Delta} \int \mathrm{d}^N\mathbf{z}\, A_N(\mathbf{q})B_N(\mathbf{z}) \times \\ \prod_{l=1}^{N} \Big[\big\langle q_{l+1} - \Delta_{l+1}/2 \big| \mathrm{e}^{-\beta_N\hat{H}} \big| q_l + \Delta_l/2 \big\rangle \times \\ \big\langle q_l + \Delta_l/2 \big| \mathrm{e}^{+\mathrm{i}\hat{H}t/\hbar} \big| z_l \big\rangle \big\langle z_l \big| \mathrm{e}^{-\mathrm{i}\hat{H}t/\hbar} \big| q_l - \Delta_l/2 \big\rangle \Big], \end{aligned} \tag{A.11}$$

concluding the derivation.

A.2 Path-integral Liouvillian

To obtain a phase-space representation of the exact TCF, we insert

$$\frac{1}{(2\pi\hbar)^N} \int \mathrm{d}^N\mathbf{p} \int \mathrm{d}^N\mathbf{\Delta}' \prod_{l=1}^{N} \mathrm{e}^{\mathrm{i}(\Delta_l - \Delta_l')p_l/\hbar} = 1 \tag{A.12}$$

into Eq. (A.11). After changing the order of integration we get

$$C_{AB}(t) = \lim_{N\to\infty} \frac{1}{(2\pi\hbar)^N} \int \mathrm{d}^N\mathbf{q} \int \mathrm{d}^N\mathbf{p} \left[\mathrm{e}^{-\beta\hat{H}}\right]_N^{\mathrm{W}}(\mathbf{p},\mathbf{q}) A_N(\mathbf{q}) \left[\hat{B}(t)\right]_N(\mathbf{p},\mathbf{q}), \tag{A.13}$$

where we introduce the generalised Wigner transforms

$$\left[\mathrm{e}^{-\beta\hat{H}}\right]_N^{\mathrm{W}}(\mathbf{p},\mathbf{q}) = \int \mathrm{d}^N\mathbf{\Delta} \prod_{l=1}^{N} \big\langle q_{l+1} - \Delta_{l+1}/2 \big| \mathrm{e}^{-\beta_N\hat{H}} \big| q_l + \Delta_l/2 \big\rangle \mathrm{e}^{\mathrm{i}p_l\Delta_l/\hbar} \tag{A.14}$$

and

$$\begin{aligned}\left[\hat{B}(t)\right]_N(\mathbf{p},\mathbf{q}) = \int \mathrm{d}^N\mathbf{z} \int \mathrm{d}^N\mathbf{\Delta}\, B_N(\mathbf{z}) \\ \times \prod_{l=1}^{N} \left\langle q_l - \Delta_l/2 \middle| \mathrm{e}^{+\mathrm{i}\hat{H}t/\hbar} \middle| z_l \right\rangle \left\langle z_l \middle| \mathrm{e}^{-\mathrm{i}\hat{H}t/\hbar} \middle| q_l + \Delta_l/2 \right\rangle \mathrm{e}^{\mathrm{i}p_l\Delta_l/\hbar},\end{aligned} \tag{A.15}$$

as first defined by Hele *et al.* [81]. Note that the second expression is just a sum of one-dimensional Wigner transforms

$$\begin{aligned}\left[\hat{B}(t)\right]_N &= \frac{1}{N}\sum_{l=1}^{N} \int \mathrm{d}\Delta_l \left\langle q_l - \Delta_l/2 \middle| \mathrm{e}^{+\mathrm{i}\hat{H}t/\hbar} \hat{B} \mathrm{e}^{-\mathrm{i}\hat{H}t/\hbar} \middle| q_l + \Delta_l/2 \right\rangle \mathrm{e}^{\mathrm{i}p_l\Delta_l/\hbar} \\ &= \frac{1}{N}\sum_{l=1}^{N} B(t)_W(p_l, q_l),\end{aligned} \tag{A.16}$$

where $B(t)_W$ is the Weyl symbol corresponding to the operator $\hat{B}(t)$. To derive the exact quantum Liouvillian in the path-integral representation, we consider the time derivative of the KTCF,

$$\frac{\mathrm{d}}{\mathrm{d}t} C_{AB}(t) = \mathrm{Tr}\left\{ \hat{A}_\beta \frac{\mathrm{d}\hat{B}(t)}{\mathrm{d}t} \right\} = \mathrm{Tr}\left\{ \hat{A}_\beta \left(\frac{\mathrm{i}}{\hbar} \left[\hat{H}, \hat{B}(t)\right] \right) \right\}. \tag{A.17}$$

Retracing the steps in Eqs. (A.1) to (A.13) we arrive at

$$\begin{aligned}\frac{\mathrm{d}}{\mathrm{d}t} C_{AB}(t) = \lim_{N\to\infty} \frac{1}{(2\pi\hbar)^N} \int \mathrm{d}^N\mathbf{q} \int \mathrm{d}^N\mathbf{p} \left[\mathrm{e}^{-\beta\hat{H}}\right]_{\overline{N}}(\mathbf{p},\mathbf{q})\, A_N(\mathbf{q}) \\ \times \frac{1}{N}\sum_{l=1}^{N} \frac{\mathrm{i}}{\hbar} [\hat{H}, \hat{B}(t)]_W(p_l, q_l).\end{aligned} \tag{A.18}$$

Next we note the following properties of the Wigner transform:

1. the functional form of monomial operators that depend only on momentum $\hat{p}$ or only on position $\hat{q}$ is invariant under the transformation [47, Eq. (2.41)], so that

$$H_W(p,q) = p^2/2m + V(q) \qquad \text{and} \qquad B_W(q) = B(q);$$

2. the Wigner transform of a commutator $[\hat{\Omega}_1, \hat{\Omega}_2]$ is proportional to the Moyal bracket [47, Eqs. (2.59) to (2.65)], so that

$$\frac{\mathrm{i}}{\hbar}[\hat{\Omega}_1, \hat{\Omega}_2]_W = -\{\{\Omega_1, \Omega_2\}\},$$

where

$$\{\{\Omega_1, \Omega_2\}\} \equiv -\frac{2}{\hbar}\Omega_{1,W}(p,q)\sin\left(\frac{\hbar}{2}\left[\frac{\overleftarrow{\partial}}{\partial p}\frac{\overrightarrow{\partial}}{\partial q} - \frac{\overleftarrow{\partial}}{\partial q}\frac{\overrightarrow{\partial}}{\partial p}\right]\right)\Omega_{2,W}(p,q),$$

and the overhead arrows indicate the direction in which the derivatives act.

Substituting these results into Eq. (A.18) gives

$$\begin{aligned}\frac{\mathrm{d}}{\mathrm{d}t}C_{AB}(t) = \lim_{N\to\infty}\frac{1}{(2\pi\hbar)^N}\int \mathrm{d}^N\mathbf{q}\int \mathrm{d}^N\mathbf{p}\left[\mathrm{e}^{-\beta\hat{H}}\right]_{\overline{N}}(\mathbf{p},\mathbf{q})A_N(\mathbf{q})\times \\ \frac{1}{N}\sum_{l=1}^{N}H(p_l,q_l)\frac{2}{\hbar}\sin\left(\frac{\hbar}{2}\left[\frac{\overleftarrow{\partial}}{\partial p_l}\frac{\overrightarrow{\partial}}{\partial q_l} - \frac{\overleftarrow{\partial}}{\partial q_l}\frac{\overrightarrow{\partial}}{\partial p_l}\right]\right)B(t)_W(p_l,q_l).\end{aligned} \tag{A.19}$$

Because mixed derivatives of $V(q_l)$ are zero, we can rewrite this as

$$\frac{\mathrm{d}}{\mathrm{d}t}C_{AB}(t) = \lim_{N\to\infty}\frac{1}{(2\pi\hbar)^N}\int \mathrm{d}^N\mathbf{q}\int \mathrm{d}^N\mathbf{p}\left[\mathrm{e}^{-\beta\hat{H}}\right]_{\overline{N}}(\mathbf{p},\mathbf{q})A_N(\mathbf{q})\hat{L}_N\left[\hat{B}(t)\right]_N(\mathbf{p},\mathbf{q}) \tag{A.20}$$

$$C_{AB}(t) = \lim_{N\to\infty}\frac{1}{(2\pi\hbar)^N}\int \mathrm{d}^N\mathbf{q}\int \mathrm{d}^N\mathbf{p}\left[\mathrm{e}^{-\beta\hat{H}}\right]_{\overline{N}}(\mathbf{p},\mathbf{q})A_N(\mathbf{q})\mathrm{e}^{\hat{L}_N t}B_N(\mathbf{q}), \tag{A.21}$$

where $\hat{L}_N$ is the exact path-integral Liouvillian

$$\hat{L}_N = \frac{1}{m}\mathbf{p}\cdot\boldsymbol{\nabla}_{\mathbf{q}} - V_N(\mathbf{q})\frac{2N}{\hbar}\sin\left(\frac{\hbar}{2}\overleftarrow{\boldsymbol{\nabla}}_{\mathbf{q}}\cdot\overrightarrow{\boldsymbol{\nabla}}_{\mathbf{p}}\right), \tag{A.22}$$

and

$$V_N(\mathbf{q}) = \frac{1}{N}\sum_{l=1}^{N}V(q_l), \tag{A.23}$$

concluding the derivation.

A.3 Mean-field approximation

Consider the exact quantum partition function, given by Eq. (A.21) with $A_N(\mathbf{q}) = B_N(\mathbf{q}) = 1$. The generalised Wigner transform in the integrand can be written as

$$\left[\mathrm{e}^{-\beta\hat{H}}\right]_N(\mathbf{p},\mathbf{q}) \xrightarrow{N\to\infty} \left(\frac{m}{2\pi\beta_N\hbar^2}\right)^{N/2} \int \mathrm{d}^N\mathbf{\Delta}\, \exp\left\{-\beta_N \sum_{l=1}^{N} \frac{1}{2}\left[V\left(q_l + \frac{\Delta_l}{2}\right) + V\left(q_l - \frac{\Delta_l}{2}\right)\right]\right\} \times$$
$$\exp\left\{-\beta_N \sum_{l=1}^{N} \frac{m\omega_N^2}{2}\left[(q_{l+1}-q_l)^2 + \frac{1}{4}(\Delta_{l+1}+\Delta_l)^2 - \Delta_l(q_{l+1}-q_{l-1})\right] - \mathrm{i}\omega_N p_l \Delta_l\right\}, \tag{A.24}$$

where $\beta_N = \beta/N$ and $\omega_N = (\beta_N\hbar)^{-1}$. We now make the orthogonal transformation

$$x_l = \sum_{n=-\nu}^{\nu} T_{ln} X_n \tag{A.25}$$

where the matrix elements T_{ln} are defined in Eq. (2.41), N is odd, $\nu = (N-1)/2$, and x_l denotes any of p_l, q_l, Δ_l. The corresponding "normal-mode" coordinate X_n denotes P_n, Q_n, or D_n respectively. After the transformation, the second line of Eq. (A.24) becomes

$$\exp\left\{-\beta_N \sum_{n=-\nu}^{\nu} m\omega_n^2 Q_n^2/2 + m\Omega_n^2 D_n^2/2 + m\omega_n\Omega_n D_n Q_{-n} - \mathrm{i}\omega_N P_n D_n\right\}, \tag{A.26}$$

where

$$\omega_n = 2\omega_N \sin\left(\frac{\pi n}{N}\right) \qquad \text{and} \qquad \Omega_n = \omega_N \cos\left(\frac{\pi n}{N}\right). \tag{A.27}$$

We now integrate over the coordinates with $|n| > (M-1)/2 \equiv \mu$ for some positive odd M,

$$\begin{aligned} Z_M(\mathbf{P}'_M, \mathbf{Q}'_M) = \frac{1}{(2\pi\hbar)^M}\left(\frac{m}{2\pi\beta_N\hbar^2}\right)^{N/2} &\int \mathrm{d}^N\mathbf{Q} \int \mathrm{d}^M\mathbf{P}_M \int \mathrm{d}^M\mathbf{D}_M \\ &\times \prod_{|n|\le\mu} \delta(Q_n - Q'_n)\,\delta(P_n - P'_n) \\ &\times \exp\left\{-\beta_N\left[\sum_{n=-\nu}^{\nu} m\omega_n^2 Q_n^2/2 + \left\{f^+(\mathbf{Q},\mathbf{D}_M) + f^-(\mathbf{Q},\mathbf{D}_M)\right\}/2\right]\right\} \\ &\times \exp\left\{-\beta_N\left[\sum_{n=-\mu}^{\mu} m\Omega_n^2 D_n^2/2 + m\omega_n\Omega_n D_n Q_{-n} - \mathrm{i}\omega_N P_n D_n\right]\right\}, \end{aligned} \tag{A.28}$$

where $\mathbf{X}_M$ is the subset of normal-mode coordinates $\{X_n \,|\, -\mu \le n \le \mu\}$ and

$$f^{\pm}(\mathbf{Q}, \mathbf{D}_M) = \frac{1}{N}\sum_{l=1}^{N} V\left(\sum_{n=-\nu}^{\nu} T_{ln} Q_n \pm \sum_{|n|\le\mu} T_{ln} D_n\right). \tag{A.29}$$

Note that for $|n| \le \mu$,

$$\lim_{\substack{N\to\infty \\ M\ll N}} \Omega_n = \omega_N \sim \mathcal{O}(N) \qquad \text{and} \qquad \lim_{\substack{N\to\infty \\ M\ll N}} \omega_n = \frac{2\pi n}{\beta\hbar} \equiv \widetilde{\omega}_n \sim \mathcal{O}(1). \tag{A.30}$$

This means that the term on the last line of Eq. (A.28) tends to a delta function. To show this, we define the "Matsubara modes" (so called because $\widetilde{\omega}_n$ are the bosonic Matsubara frequencies),

$$\widetilde{X}_n = X_n/\sqrt{N} \sim \mathcal{O}(1). \tag{A.31}$$

We then rewrite the last line of Eq. (A.28) in the specified limit as

$$\begin{aligned} &\exp\left\{-\frac{\beta m\omega_N^2}{2}\sum_{|n|\le\mu}\left[\widetilde{D}_n + \frac{1}{\omega_N}(\widetilde{\omega}_n\widetilde{Q}_{-n} - \mathrm{i}\widetilde{P}_n/m)\right]^2\right\}\exp\left\{\frac{\beta m}{2}\sum_{|n|\le\mu}\left[\widetilde{\omega}_n\widetilde{Q}_{-n} - \mathrm{i}\widetilde{P}_n/m\right]^2\right\} \\ &\xrightarrow[M\ll N]{N\to\infty} \left(\frac{2\pi}{\beta m\omega_N^2}\right)^{M/2}\delta^M(\widetilde{\mathbf{D}}_M)\exp\left\{-\beta\sum_{|n|\le\mu}\left[\frac{\widetilde{P}_n^2}{2m} - \frac{m\widetilde{\omega}_n^2\widetilde{Q}_n^2}{2} + \mathrm{i}\widetilde{\omega}_n\widetilde{P}_n\widetilde{Q}_{-n}\right]\right\} \end{aligned} \tag{A.32}$$

After integrating over $\widetilde{D}_M$ we get

$$\begin{aligned} Z_M(\mathbf{P}'_M, \mathbf{Q}'_M) = &\left(\frac{N}{2\pi\hbar}\right)^M\left(\frac{mN}{2\pi\beta_N\hbar^2}\right)^{(N-M)/2}\int \mathrm{d}^N\widetilde{\mathbf{Q}}\int \mathrm{d}^M\widetilde{\mathbf{P}}_M\prod_{|n|\le\mu}\delta\left(\widetilde{Q}_n - \widetilde{Q}'_n\right)\delta\left(\widetilde{P}_n - \widetilde{P}'_n\right) \\ &\times\exp\left\{-\beta\left[\sum_{|n|\le\mu}\left(\frac{\widetilde{P}_n^2}{2m} + \mathrm{i}\widetilde{\omega}_n\widetilde{P}_n\widetilde{Q}_{-n}\right) + \sum_{|n|>\mu}\frac{m\omega_n^2\widetilde{Q}_n^2}{2} + \frac{1}{N}\sum_{l=1}^{N} V\left(\sum_n \sqrt{N}T_{ln}\widetilde{Q}_n\right)\right]\right\}. \end{aligned} \tag{A.33}$$

Hence the exact quantum partition function can be written as

$$Z = \frac{1}{(2\pi\hbar)^M}\int \mathrm{d}^M\widetilde{\mathbf{Q}}_M\int \mathrm{d}^M\widetilde{\mathbf{P}}_M\, \mathrm{e}^{-\beta\mathcal{H}_M(\widetilde{\mathbf{P}}_M,\widetilde{\mathbf{Q}}_M)}\mathrm{e}^{-\mathrm{i}\beta\theta_M(\widetilde{\mathbf{P}}_M,\widetilde{\mathbf{Q}}_M)}, \tag{A.34}$$

where $\mathcal{H}_M(\widetilde{\mathbf{P}}_M, \widetilde{\mathbf{Q}}_M)$ is the mean-field Hamiltonian

$$\mathrm{e}^{-\beta\mathcal{H}_M(\widetilde{\mathbf{P}},\widetilde{\mathbf{Q}})} = \frac{1}{(2\pi\hbar)^{N-M}} \int \mathrm{d}^N\mathbf{q} \int \mathrm{d}^N\mathbf{p}\, \delta(\mathbf{q}, \widetilde{\mathbf{Q}}_M)\, \delta(\mathbf{p}, \widetilde{\mathbf{P}}_M)\, \mathrm{e}^{-\beta_N[H_N(\mathbf{p},\mathbf{q}) - N\widetilde{S}_M(\widetilde{\mathbf{Q}}_M)]}, \tag{A.35}$$

$$\delta(\mathbf{x}, \widetilde{\mathbf{X}}_M) = \prod_{n=-\mu}^{\mu} \delta\left(\sum_{l=1}^{N} N^{-1/2} T_{ln} x_l - \widetilde{X}_n\right). \tag{A.36}$$

Here, $H_N(\mathbf{p}, \mathbf{q})$ is the ring-polymer Hamiltonian, $\widetilde{S}_M(\widetilde{\mathbf{Q}}_M)$ is the spring energy of the Matsubara modes, and $\theta_M(\widetilde{\mathbf{P}}_M, \widetilde{\mathbf{Q}}_M)$ is the Matsubara phase, defined in Eqs. (2.29), (3.10) and (3.14) respectively. We can integrate the momenta analytically, to get

$$Z = \frac{1}{(2\pi\hbar)^M} \int \mathrm{d}^M\widetilde{\mathbf{Q}}_M \int \mathrm{d}^M\widetilde{\mathbf{P}}_M\, \mathrm{e}^{-\beta[|\widetilde{\mathbf{P}}_M|^2/2m + \mathcal{F}_M(\widetilde{\mathbf{Q}}_M)]} \mathrm{e}^{-\mathrm{i}\beta\theta_M(\widetilde{\mathbf{P}}_M, \widetilde{\mathbf{Q}}_M)}, \tag{A.37}$$

where the free energy $\mathcal{F}_M(\widetilde{\mathbf{Q}}_M)$ is defined in Eq. (3.9). Eq. (A.37) is analogous to the "truncated" Matsubara partition function of Ref. [81], which tends to the same limit as $M \to \infty$, but differs by the sign of the Matsubara phase θ_M. As shown by Willatt [88, Section. 3.3.2], changing the sign is equivalent to the simultaneous reversal of real ($t \to -t$) and imaginary ($l \to N - l$) time, which leaves the partition function and the TCFs we consider here unaffected. For this reason, and to be consistent with previous work, we write the phase factor as $\mathrm{e}^{\mathrm{i}\beta\theta_M}$ from here on.

To calculate the approximate Liouvillian in Eq. (3.4), we need only consider the mean-field average of $\boldsymbol{\nabla}_{\widetilde{\mathbf{Q}}_M} V_N(\mathbf{q})$, as all the other terms in the nascent Liouvillian of Eq. (3.7) depend only on the Matsubara coordinates and are unaffected by the mean-fielding. Repeating the steps in Eqs. (A.24) to (A.33) with an additional factor of $\boldsymbol{\nabla}_{\widetilde{\mathbf{Q}}_M} V_N(\mathbf{q})$, we get

$$\begin{aligned} &\frac{\int \mathrm{d}^N\mathbf{p} \int \mathrm{d}^N\mathbf{q} \left[\mathrm{e}^{-\beta\hat{H}}\right]_{\overline{N}} \delta(\mathbf{q}, \widetilde{\mathbf{Q}}_M)\, \delta(\mathbf{p}, \widetilde{\mathbf{P}}_M)\, \boldsymbol{\nabla}_{\widetilde{\mathbf{Q}}_M} V_N(\mathbf{q})}{\int \mathrm{d}^N\mathbf{p} \int \mathrm{d}^N\mathbf{q} \left[\mathrm{e}^{-\beta\hat{H}}\right]_{\overline{N}} \delta(\mathbf{q}, \widetilde{\mathbf{Q}}_M)\, \delta(\mathbf{p}, \widetilde{\mathbf{P}}_M)} = \\ &\frac{\int \mathrm{d}^N\mathbf{q}\, \delta(\mathbf{q}, \widetilde{\mathbf{Q}}_M) \boldsymbol{\nabla}_{\widetilde{\mathbf{Q}}_M} V_N(\mathbf{q})\, \mathrm{e}^{-\beta[W_N(\mathbf{q}) - S_M(\widetilde{\mathbf{Q}}_M)]}}{\int \mathrm{d}^N\mathbf{q}\, \delta(\mathbf{q}, \widetilde{\mathbf{Q}}_M) \mathrm{e}^{-\beta[W_N(\mathbf{q}) - S_M(\widetilde{\mathbf{Q}}_M)]}} = \boldsymbol{\nabla}_{\widetilde{\mathbf{Q}}_M} \mathcal{F}_M(\widetilde{\mathbf{Q}}_M), \end{aligned} \tag{A.38}$$

which leads to the final expression for the mean-field Liouvillian in Eq. (3.8).

A.4 Local normal-mode approximation

We can understand the origin of some of the spurious features discussed in Section 3.3.1 by considering a local normal-mode approximation to Matsubara dynamics. Here the approximation is derived using the "truncated" Matsubara formalism, but can easily be extended to the mean-field picture. To find the local normal modes, we expand the Matsubara potential about the centroid,

$$\widetilde{V}_M(\widetilde{\mathbf{Q}}_M) = \widetilde{V}_M(\widetilde{\mathbf{Q}}_0) + [\widetilde{\mathbf{Q}}']^\top \boldsymbol{\nabla}_{\widetilde{\mathbf{Q}}'} \widetilde{V}_M(\widetilde{\mathbf{Q}}_0) + \frac{1}{2}[\widetilde{\mathbf{Q}}']^\top \mathbf{K}(\widetilde{\mathbf{Q}}_0)\, \widetilde{\mathbf{Q}}' + O(\widetilde{\mathbf{Q}}')^3, \tag{A.39}$$

where $\widetilde{\mathbf{Q}}_0$ is a vector of Matsubara coordinates with all the non-centroid modes set to zero, and $\widetilde{\mathbf{Q}}'$ is a truncated vector of normal-mode coordinates with the centroids removed. By converting to bead representation it is straightforward to show that the linear term vanishes, and so the transformation that diagonalises the dynamical matrix $\mathbf{K}(\widetilde{\mathbf{Q}}_0)$ is precisely the local normal mode transformation. The dynamical matrix has a particularly simple form,

$$K_{ni,mj} = \frac{1}{N}\left[\sum_{l=1}^{N} \frac{\partial}{\partial \widetilde{Q}_{ni}} \frac{\partial}{\partial \widetilde{Q}_{mj}} V\left(\sum_{k=\overline{\mu}}^{\mu} \sqrt{N} T_{lk} \widetilde{\mathbf{Q}}_k\right)\right] = \sum_{l=1}^{N} T_{ln} T_{lm} \frac{\partial^2 V(\widetilde{\mathbf{Q}}_0)}{\partial \widetilde{Q}_{0,i} \partial \widetilde{Q}_{0,j}} = K^{(F)}_{ij} \delta_{nm}, \tag{A.40}$$

where n, m, and k run over the normal mode indices, i and j index the F spatial dimensions, and $\mathbf{K}^{(F)}$ is the $F \times F$ Hessian matrix calculated for the potential $V(\mathbf{x})$ at $\mathbf{x} = \widetilde{\mathbf{Q}}_0$. For a two-dimensional axially symmetric potential

$$V(\widetilde{\mathbf{Q}}_0) = V(R_0) \qquad R_0 = \sqrt{\widetilde{X}_0^2 + \widetilde{Y}_0^2},$$

the Hessian is

$$\mathbf{K}^{(2)}(\widetilde{\mathbf{Q}}_0) = \begin{pmatrix} \cos^2\Theta_0 \frac{\mathrm{d}^2V}{\mathrm{d}R_0^2} + \sin^2\Theta_0 \frac{1}{R_0}\frac{\mathrm{d}V}{\mathrm{d}R_0} & \frac{1}{2}\sin 2\Theta_0 \left[\frac{\mathrm{d}^2V}{\mathrm{d}R_0^2} - \frac{1}{R_0}\frac{\mathrm{d}V}{\mathrm{d}R_0}\right] \\ \frac{1}{2}\sin 2\Theta_0 \left[\frac{\mathrm{d}^2V}{\mathrm{d}R_0^2} - \frac{1}{R_0}\frac{\mathrm{d}V}{\mathrm{d}R_0}\right] & \sin^2\Theta_0 \frac{\mathrm{d}^2V}{\mathrm{d}R_0^2} + \cos^2\Theta_0 \frac{1}{R_0}\frac{\mathrm{d}V}{\mathrm{d}R_0} \end{pmatrix} \tag{A.41}$$

where

$$\widetilde{X}_0 = R_0 \cos\Theta_0 \qquad \widetilde{Y}_0 = R_0 \sin\Theta_0. \tag{A.42}$$

This matrix is diagonalised by

$$\mathbf{U}(\widetilde{\mathbf{Q}}_0) = \begin{pmatrix} \cos\Theta_0 & -\sin\Theta_0 \\ \sin\Theta_0 & \cos\Theta_0 \end{pmatrix} = \frac{1}{R_0}\begin{pmatrix} \widetilde{X}_0 & -\widetilde{Y}_0 \\ \widetilde{Y}_0 & \widetilde{X}_0 \end{pmatrix}, \tag{A.43}$$

which corresponds to the local normal modes (not to be confused with the quasicentroids of Chapters 4 and 5)

$$\overline{Q}_{ni} = \sum_{j=1}^{2} U_{ji} \widetilde{Q}_{nj} \qquad \Leftrightarrow \qquad \widetilde{Q}_{ni} = \sum_{j=1}^{2} U_{ij} \overline{Q}_{nj} \tag{A.44a}$$

for $n \neq 0$, and

$$\overline{Q}_{0i} = \widetilde{Q}_{0i} \tag{A.44b}$$

for $n = 0$. The coordinates $\overline{Q}_{n1}$ and $\overline{Q}_{n2}$, $n \neq 0$, can be identified as the vibrational and the rotational modes, respectively. Expressed in these coordinates, the Matsubara Hamiltonian becomes

$$\widetilde{H}_M(\overline{\mathbf{P}}, \overline{\mathbf{Q}}) = \frac{1}{2m} \overline{\mathbf{P}}^{\top} \mathbf{G}^{-1} \overline{\mathbf{P}} + \widetilde{V}_M \left(\left\{ \overline{\mathbf{Q}}_0, \mathbf{U} \overline{\mathbf{Q}}_n \,|\, n \neq 0 \right\} \right), \tag{A.45}$$

where $\mathbf{G}^{-1}$ is the inverse metric tensor

$$[\mathbf{G}^{-1}]_{ni,mj} = \sum_{k,s} \frac{\partial \overline{Q}_{ks}}{\partial \widetilde{Q}_{ni}} \frac{\partial \overline{Q}_{ks}}{\partial \widetilde{Q}_{mj}}. \tag{A.46}$$

We distinguish three groups of elements:

1. $n, m \neq 0 \quad \Rightarrow \quad [\mathbf{G}^{-1}]_{ni,mj} = \delta_{nm}\delta_{ij}$

2. $n = 0, m \neq 0 \quad \Rightarrow \quad [\mathbf{G}^{-1}]_{0i,mj} = -\sum_{s=1}^{2} \frac{\partial U_{js}}{\partial \widetilde{Q}_{0i}} \overline{Q}_{ms} \equiv B_{ij}^{(m)}$

3. $n = m = 0 \quad \Rightarrow \quad [\mathbf{G}^{-1}]_{0i,0j} = 1 + \sum_{k\neq 0} \sum_{s=1}^{2} B_{is}^{(k)} B_{js}^{(k)}$

For an axially symmetric potential

$$\frac{\partial \mathbf{U}}{\partial \widetilde{X}_0} = \frac{1}{R_0} \begin{pmatrix} \sin^2 \Theta_0 & \frac{1}{2} \sin 2\Theta_0 \\ -\frac{1}{2} \sin 2\Theta_0 & \sin^2 \Theta_0 \end{pmatrix} \qquad \frac{\partial \mathbf{U}}{\partial \widetilde{Y}_0} = \frac{1}{R_0} \begin{pmatrix} -\frac{1}{2} \sin 2\Theta_0 & -\cos^2 \Theta_0 \\ \cos^2 \Theta_0 & -\frac{1}{2} \sin 2\Theta_0 \end{pmatrix},$$

and so the coupling matrices $\mathbf{B}^{(k)}$ scale as $O(|\overline{\mathbf{Q}}_k|/|\overline{\mathbf{Q}}_0|)$. These couple the dynamics of the centroid and the local normal modes. If we neglect this coupling, we get the approximate

local-normal-mode (LNM) Hamiltonian

$$\overline{H}_M(\overline{\mathbf{P}},\overline{\mathbf{Q}}) = \frac{1}{2m}\overline{\mathbf{P}}^{\top}\overline{\mathbf{P}} + \widetilde{V}_M\left(\left\{\overline{\mathbf{Q}}_0, \mathbf{U}\overline{\mathbf{Q}}_n \,|\, n \neq 0\right\}\right), \tag{A.47}$$

with the corresponding equations of motion

$$\frac{\mathrm{d}\overline{P}_{ni}}{\mathrm{d}t} = -\frac{\partial\widetilde{V}_M}{\partial\overline{Q}_{ni}} \qquad \frac{\mathrm{d}\overline{Q}_{ni}}{\mathrm{d}t} = \frac{\overline{P}_{ni}}{m}, \tag{A.48}$$

where

$$\frac{\partial\widetilde{V}_M}{\partial\overline{\mathbf{Q}}_{n\neq0,i}} = \sum_{s=1}^{2} U_{si}\frac{\partial\widetilde{V}_M}{\partial\widetilde{\mathbf{Q}}_{n\neq0,s}} \tag{A.49}$$

and

$$\begin{aligned}
\frac{\partial\widetilde{V}_M}{\partial\overline{X}_0} &= \frac{\partial\widetilde{V}_M}{\partial\widetilde{X}_0} - \frac{\sin\Theta_0}{R_0}\sum_{k\neq0}\left[\widetilde{X}_k\frac{\partial\widetilde{V}_M}{\partial\widetilde{Y}_k} - \widetilde{Y}_k\frac{\partial\widetilde{V}_M}{\partial\widetilde{X}_k}\right] \\
\frac{\partial\widetilde{V}_M}{\partial\overline{Y}_0} &= \frac{\partial\widetilde{V}_M}{\partial\widetilde{X}_0} + \frac{\cos\Theta_0}{R_0}\sum_{k\neq0}\left[\widetilde{X}_k\frac{\partial\widetilde{V}_M}{\partial\widetilde{Y}_k} - \widetilde{Y}_k\frac{\partial\widetilde{V}_M}{\partial\widetilde{X}_k}\right].
\end{aligned} \tag{A.50}$$

The transformation in Eq. (A.43) defines a rotating frame of reference that follows the centroid coordinate. Neglecting $\mathbf{B}^{(k)}$ removes the coupling between this rotation and the fluctuations of the non-centroid modes [131, §39]. Since these fluctuations are in turn coupled to the vibrational dynamics of the centroid, the local normal-mode approximation has the net effect of removing the part of the centroid rovibrational coupling that is mediated by the non-centroid modes.

In Figure A.1 we compare the three-mode truncated Matsubara spectra calculated at 200 K with and without the LNM approximation. The only significant difference between the two spectra is the disappearance of the spurious wiggles at around 3000 cm^{-1} when the LNM approximation is used, which strongly suggests that their origin lies in the rotational dynamics of the centroid. We get similar results for mean-field Matsubara dynamics (not shown), obtained by replacing $\widetilde{V}_M$ in Eqs. (A.48) to (A.50) with $\mathcal{F}_M$. Presumably when the number of Matsubara modes M is sufficiently large, the ring polymer can deform to follow the curve of the potential energy surface without unphysical interference with the dynamics of the centroid, although this is clearly not the case for the elliptical $M = 3$ ring-polymer loops.

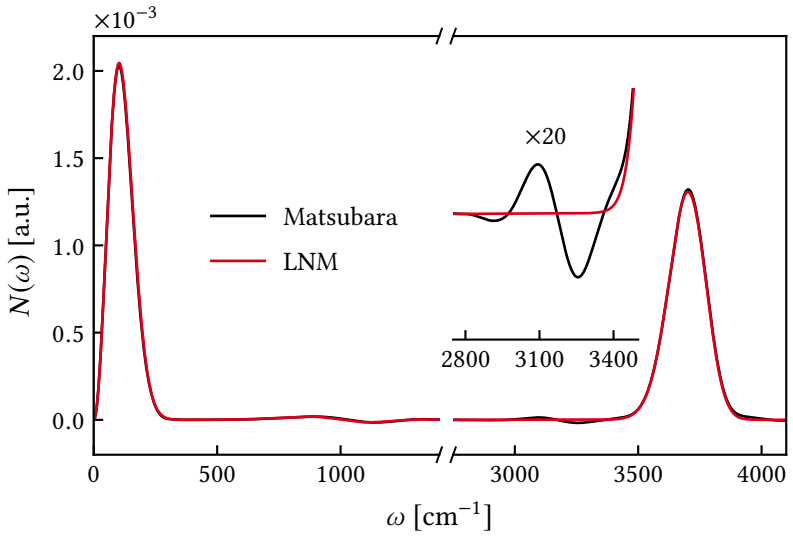

Figure A.1 IR absorption spectra for the two-dimensional Morse potential in Eq. (3.22), simulated using three-mode ($M = 3$) truncated Matsubara dynamics and its local-normal-mode (LNM) approximation at $T = 200$ K. The neglect of rovibrational coupling between the centroid and non-centroid modes in the LNM approximation causes the high-frequency wiggles (magnified in the inset) to disappear, while leaving the rest of the spectrum largely unaffected.

A.5 The cross-over radius of CMD

To derive the expression for the cross-over radius in Eq. (3.27), consider the ring-polymer potential $W_N(\mathbf{q})$ expressed in plane polar coordinates,

$$W_N(\mathbf{r},\boldsymbol{\theta}) = \frac{1}{N}\sum_{l=1}^{N}\left\{V(r_l) + \frac{m\omega_N^2}{2}\left[(r_l - r_{l+1})^2 + r_l r_{l+1}(\theta_l - \theta_{l+1})^2\right] + \mathcal{O}(\theta_l - \theta_{l+1})^4\right\}, \tag{A.51}$$

$$r_l = \sqrt{x_l + y_l} \qquad \theta_l = \tan^{-1}(y_l/x_l). \tag{A.52}$$

To find the centroid-constrained instanton, we minimise $W_N(\mathbf{q})$ subject to

$$\frac{1}{N}\sum_{l=1}^{N} r_l \cos\theta_l = \widetilde{X}_0 \qquad \frac{1}{N}\sum_{l=1}^{N} r_l \sin\theta_l = \widetilde{Y}_0. \tag{A.53}$$

Without loss of generality we set $\widetilde{Y}_0 = 0$, constraining the centroid to lie on the x-axis. In the derivation we will approach the critical radius R_c from above, so that until R_c is reached, the minimum-energy configuration remains collapsed at the centroid. Hence we can expand

Eq. (A.51) to second order in $(r_l - \widetilde{X}_0)$ and θ_l

$$W_N(\mathbf{r},\boldsymbol{\theta}) = \frac{1}{N}\sum_{l=1}^{N}\left\{V(\widetilde{X}_0) + \frac{\mathrm{d}V}{\mathrm{d}\widetilde{X}_0}(r_l - \widetilde{X}_0) + \frac{1}{2}\frac{\mathrm{d}^2V}{\mathrm{d}\widetilde{X}_0^2}(r_l - \widetilde{X}_0)^2 + \frac{m\omega_N^2}{2}(r_l - r_{l+1})^2 + \frac{m\omega_N^2}{2}\widetilde{X}_0^2(\theta_l - \theta_{l+1})^2\right\}. \tag{A.54}$$

It will now be convenient to introduce polar "normal-mode coordinates"

$$R_n = \frac{1}{\sqrt{N}}\sum_{l=1}^{N} T_{ln} r_l \qquad\qquad \Theta_n = \frac{1}{\sqrt{N}}\sum_{l=1}^{N} T_{ln}\theta_l, \tag{A.55}$$

where the transformation matrix T_{ln} is defined in Eq. (2.41). Expanding the first constraint in Eq. (A.53) to second order in $R_{n\neq 0}$ and Θ_n yields

$$R_0 - \widetilde{X}_0 = \frac{1}{2}\widetilde{X}_0\sum_n \Theta_n^2,$$

which we may use to simplify the term

$$\begin{aligned}\frac{1}{N}\sum_{l=1}^{N}(r_l - \widetilde{X}_0)^2 &= \sum_n R_n^2 - \widetilde{X}_0\left(2R_0 - \widetilde{X}_0\right)\\ = \sum_n R_n^2 - \left(R_0 - \frac{1}{2}\widetilde{X}_0\sum_n\Theta_n^2\right)&\left(R_0 + \frac{1}{2}\widetilde{X}_0\sum_n\Theta_n^2\right) = \sum_n R_n^2 - R_0^2,\end{aligned} \tag{A.56}$$

correct to second order in Θ_n. With this simplification, the potential energy becomes

$$W_N(\mathbf{r},\boldsymbol{\theta}) = V(\widetilde{X}_0) + \frac{1}{2}\sum_{n\neq 0}\left\{\frac{\mathrm{d}^2V}{\mathrm{d}\widetilde{X}_0^2} + m\omega_n^2\right\}R_n^2 + \frac{1}{2}\sum_n\left\{\widetilde{X}_0\frac{\mathrm{d}V}{\mathrm{d}\widetilde{X}_0} + m\omega_n^2\widetilde{X}_0^2\right\}\Theta_n^2,$$

which implicitly incorporates the first constraint from Eq. (A.53). The second constraint can be incorporated explicitly using the method of Lagrange undetermined multipliers [89, pp. 167–173]. It is then straightforward to show that for $\mathrm{d}^2V/\mathrm{d}\widetilde{X}_0^2 > 0$ the extremal points are $\Theta_0 = 0$, $R_{n\neq 0} = 0$, and

$$\widetilde{X}_0\left\{\frac{\mathrm{d}V}{\mathrm{d}\widetilde{X}_0} + m\omega_n^2\widetilde{X}_0\right\}\Theta_n = 0.$$

This has a non-trivial solution for $\Theta_{\pm 1} \neq 0$ when

$$\widetilde{X}_0 = -\frac{1}{m\omega_1^2}\frac{\mathrm{d}V}{\mathrm{d}\widetilde{X}_0}, \tag{A.57}$$

which, after relaxing the condition that the centroid lie on the x-axis and taking the limit $N \to \infty$, gives us the final expression in Eq. (3.27).

A.6 Simulation details

A.6.1 The one-dimensional quartic potential

DVR calculations To calculate the exact Kubo-transformed time-correlation functions in Section 3.2 we used the 10 lowest eigenstates of the quartic oscillator $V(q) = 1/4q^4$. These were calculated in the discrete variable representation (DVR) proposed by Colbert and Miller [25], on a grid of 500 points ranging from −7 to 7 a.u.

PIMD calculations The mean-field forces for CMD and three-mode mean-field Matsubara dynamics [MF(3)] were calculated using standard PIMD techniques [50]. In both cases we used $N = 16$ beads at $\beta = 1$ and $N = 64$ beads and $\beta = 8$. The non-centroid modes $\widetilde{Q}_n$ were subject to a local Path-Integral Langevin Equation thermostat (PILE-L) [92] with friction parameters $\gamma_n = \omega_n$, where ω_n are the frequencies defined in Eq. (2.44). We used the symplectic propagator from Ref. [92] to integrate the equations of motion while holding M Matsubara modes fixed.

In the case of CMD we only needed to constrain the centroid $\widetilde{Q}_0$ ($M = 1$). The positions at which it was fixed spanned either 65 (for $\beta = 1$) or 129 (for $\beta = 8$) equally spaced points between −10 and 10 a.u. At each point we ran 100 independent trajectories that were first equilibrated for $t_{\mathrm{eq}} = 10\beta\hbar$ and then propagated for 10^5 steps with an integration step $\Delta t = 0.01\beta\hbar$. We recorded the value of

$$-\frac{\partial \widetilde{V}_M}{\partial \widetilde{Q}_0} = -\frac{1}{N}\sum_{l=1}^{N}\frac{\partial V(q_l)}{\partial q_l}$$

after each time step, and calculated its average over the steps and trajectories to obtain the mean-field centroid force at each grid point.

In the case of three-mode Matsubara dynamics we had to additionally constrain $\widetilde{Q}_{\pm 1}$. Defining

$$\rho_1 = \sqrt{\widetilde{Q}_{-1}^2 + \widetilde{Q}_1^2} \qquad \phi_1 = \tan^{-1}\left(\widetilde{Q}_1/\widetilde{Q}_{-1}\right)$$

we note that by imaginary-time translation symmetry, the three-mode Matsubara potential does not depend on θ_1 (see [88, Eq. 3.65–3.70]). Hence we only needed to consider a two-dimensional grid in $\widetilde{Q}_0$ and ρ_1. This was done by setting $\widetilde{Q}_{-1} = 0$ and letting $(\widetilde{Q}_0, \widetilde{Q}_1)$ take on values on a 65×33 regular grid ranging from $(-10, 0)$ to $(10, 10)$. At each point we ran 5 independent trajectories that were first equilibrated for $t_{\mathrm{eq}} = 10\beta\hbar$, and then propagated for 10^6 steps with an integration time step $\Delta t = 0.005\beta\hbar$. The mean-field centroid force was calculated as before, and the non-centroid force was calculated as the thermal average of

$$-\frac{\partial \widetilde{V}_M}{\partial \rho_1} = -\frac{\partial \widetilde{V}_M}{\partial \widetilde{Q}_1}\bigg|_{\widetilde{Q}_{-1}=0} \qquad \text{where} \qquad -\frac{\partial \widetilde{V}_M}{\partial \widetilde{Q}_n} = -N^{-1/2}\sum_{l=1}^{N} T_{ln}\frac{\partial V(q_l)}{\partial q_l}.$$

Dynamics simulations To calculate the time-correlation functions in Figure 3.1 we propagated a set of n_{traj} independent trajectories for each of CMD, Matsubara, mean-field Matsubara [MF(3)], and classical dynamics using the velocity Verlet algorithm [49], with an integration time step $\Delta t = 0.01\beta\hbar$. The forces for CMD and MF(3) were obtained by cubic spline interpolation [98] of the pre-calculated values described above.

Table A.1 Simulation parameters for the one-dimensional quartic potential. The parameters are for both $\beta = 1$ and $\beta = 8$, unless indicated otherwise.

	CMD Classical	Matsubara	MF(3)	AMF(3)	
				$\beta = 1$	$\beta = 8$
n_{traj}	800	800	640	65536	5120
n_{sample}	10^4	10^5	10^5	10^2	10^3
t_{rel}	$2\beta\hbar$	$2\beta\hbar$	$\beta\hbar$	2	8
t_{prod}	40	40	30	20	30

Each trajectory was first equilibrated for $t_{\mathrm{eq}} = 10\beta\hbar$ using a Langevin thermostat with friction $\gamma_0 = 1$. This was followed by a series of alternating production intervals of length t_{prod}, where the thermostat was switched off, and relaxation intervals of length t_{rel}, where the thermostat was switched on. At every production interval we calculated the correlation of the centroid position with its value at the start of the interval, giving a total of n_{sample} contributions to the thermally averaged TCF per trajectory. An analogous procedure was used for the adiabatic [AMF(3)] simulations in Section 3.2.2, except that the time step was set to $\Delta t = 0.02$ at both temperatures, and the symplectic integrator from Ref. [92] was used to propagate the ring-polymer dynamics. In addition, a PILE-L thermostat was acting on the

non-Matsubara modes ($n \neq 0, \pm 1$) at all times, with a friction parameter $\gamma = \Omega$, where Ω is defined in Eq. (3.21). In Table A.1 we summarise the values of n_{traj}, n_{sample}, t_{rel}, and t_{prod} used by the different methods.

It remains to add that the trajectories in Matsubara and mean-field Matsubara dynamics simulations do not sample the phase in the Boltzmann distribution of Eq. (3.12), and so to get the time-correlation functions we had to calculate

$$\widetilde{C}_{AB}^{[M]} = \left\langle \mathrm{e}^{\mathrm{i}\beta\theta_M} A_M(0) B_M(t) \right\rangle \times \left\langle \mathrm{e}^{\mathrm{i}\beta\theta_M} \right\rangle^{-1},$$

where

$$\langle \cdots \rangle = \int \mathrm{d}^M \widetilde{\mathbf{P}}_M \int \mathrm{d}^M \widetilde{\mathbf{Q}}_M \, (\cdots) \, \mathrm{e}^{-\beta \mathcal{H}_M(\widetilde{\mathbf{P}}_M, \widetilde{\mathbf{Q}}_M)}.$$

For the denominator, we may deform the integration contour so as to get a positive definite estimator

$$\left\langle \mathrm{e}^{\mathrm{i}\beta\theta_M} \right\rangle = \left\langle \mathrm{e}^{-\beta \widetilde{S}_M(\widetilde{\mathbf{Q}}_M)} \right\rangle,$$

where $\widetilde{S}_M(\widetilde{\mathbf{Q}}_M)$ is defined in Eq. (3.10). This estimator has better convergence properties and is used in all our Matsubara-dynamics calculations.

A.6.2 The two-dimensional Morse potential

DVR calculations To calculate the exact KTCFs (and hence the exact power spectra), we transformed the Schrödinger equation to plane polar coordinates and separated it into an angular and a radial part. The angular equation was solved analytically, and the radial equations were solved numerically in the DVR representation due to Colbert and Miller [25, App. A2]. For the calculation we used a radial grid of 1000 points ranging from 0 to 6 a.u., and kept all the eigenstates with energies below 0.1875 a.u.

PIMD calculations To calculate the mean-field centroid forces for the CMD simulations in Section 3.3.2 we used a procedure analogous to the one described in Appendix A.6.1. By symmetry, the mean-field angular forces on the centroid are zero, and so we only needed to consider the radial forces at a range of displacements from the origin. We did so by constraining the y-component of the centroid at $\widetilde{Y}_0 = 0$ and letting $\widetilde{X}_0$ take on values on a regular grid of n_{pts} points between 0.5 and 2.0 Å. At each point we ran 5 independent trajectories that were first equilibrated for 3 ps and then propagated for 2000 ps under a PILE-L thermostat with non-centroid friction $\gamma_n = \omega_n$. The number of beads N, the grid size n_{pts}, and

the integration time step Δt are summarised in Table A.2 for the different temperatures in Figure 3.5.

Table A.2 Simulation parameters for CMD mean-field force calculations for the two-dimensional Morse potential.

T/K	200	400	600–800
N	64	32	16
n_{pts}	129	65	65
Δt/fs	0.05	0.10	0.10

Dynamics simulations To calculate the time-correlation functions used to produce the spectra in Sections 3.3.1 and 3.3.2, we followed a procedure analogous to the one described in Appendix A.6.1. Unless indicated otherwise, the number of ring-polymer beads at the different temperatures was taken to be the same as in the PIMD calculations in Table A.2.

Table A.3 Mean-field Matsubara dynamics simulation parameters for the two-dimensional Morse potential. The numbers in brackets are for the five-mode simulation. The adiabatic separation is $\gamma = 32$ throughout.

T/K	200	400	500	600	800
N	32(24)	32	16	16	16
n_{traj}	64(512)	64	64	64	256
n_{sample}	$10^3(5\times10^5)$	1000	4000	4000	4000

We used an integration time step of $\Delta t = 0.1$ fs everywhere except for mean-field Matsubara dynamics, which required $\Delta t = 0.1/\gamma$ fs, where γ is the adiabaticity constant. All TCFs were calculated to span 500 fs. At the start of each simulation we equilibrated the system for 500 fs under a PILE-L thermostat with a centroid/dynamical-mode friction $\gamma_0 = 1.0$ fs^{-1}, except for TRPMD, which used the more optimal $\gamma_0 = 0.01$ fs^{-1}. The non-centroid/mean-fielded-mode friction was set to $\gamma_n = \omega_n$. The subsequent production intervals where each 1000 fs long and separated by relaxation intervals of 100 fs. To accelerate convergence we made use of horizontal statistics, time-averaging the contributions to the TCFs over each production interval, as described in Ref. [48, Sec. 6.3.2].

Table A.4 Selected simulation parameters for the methods in Figures 3.4 and 3.5. Unless stated otherwise, the parameters are the same at all temperatures.

	CMD	TRPMD[a]	Matsubara	
			$M = 3$	$M = 5$
n_{traj}	5	4	8	10
n_{sample}	10^6	10^3	[b]	5×10^8

[a] Except at 800 K, where $n_{\text{traj}} = 8$ and $n_{\text{sample}} = 4000$.
[b] $n_{\text{sample}} = 10^4$ at 200 K, 4×10^4 at 300 and 400 K, and 16×10^4 at 500 and 600 K.

Mean-field Matsubara dynamics was propagated using the adiabatic algorithm with $\gamma = 32$. The number of beads, trajectories, and production intervals used at the different temperatures is summarised in Table A.3. Truncated Matsubara dynamics was propagated using the standard velocity Verlet algorithm [49]. To calculate the forces, we propagated a ring-polymer with $N = 16$ beads, explicitly constraining the Matsubara modes with $|n| > (M-1)/2$ to zero. CMD was also propagated under the velocity Verlet algorithm and used pre-calculated grid forces that were interpolated with cubic splines [98]. TRPMD was propagated using the symplectic integrator from Ref. [92]. The number of trajectories and production intervals in these simulations is summarised in Table A.4.

Appendix B

Quasicentroid molecular dynamics

B.1 Matsubara Liouvillian in curvilinear coordinates

In Section 4.2.1 we consider the part of the mean-field Matsubara Liouvillian that acts only on the curvilinear coordinates $(\overline{\boldsymbol{\pi}}_a, \boldsymbol{\xi}_a)$. This is derived from the Liouvillian expressed in terms of $(\boldsymbol{\pi}, \boldsymbol{\xi})$,

$$\begin{aligned}\hat{L}_{\mathrm{MF}}(\boldsymbol{\pi},\boldsymbol{\xi}) = \{\,\cdot\,,\mathcal{H}_M\} &= \sum_{k=1}^{M}\left\{\frac{\partial\mathcal{H}_M}{\partial\pi_k}\frac{\partial}{\partial\xi_k} - \frac{\partial\mathcal{H}_M}{\partial\xi_k}\frac{\partial}{\partial\pi_k}\right\} \\ &= \sum_{k=1}^{M}\left\{\left(\mathbf{G}^{-1}\boldsymbol{\pi}\right)_k\frac{\partial}{\partial\xi_k} - \frac{\partial\mathcal{F}_M}{\partial\xi_k}\frac{\partial}{\partial\pi_k} - \left[\frac{1}{2}\boldsymbol{\pi}^{\top}\frac{\partial\mathbf{G}^{-1}}{\partial\xi_k}\boldsymbol{\pi}\right]\frac{\partial}{\partial\pi_k}\right\},\end{aligned} \tag{B.1}$$

where we have used the fact that $(\boldsymbol{\pi}, \boldsymbol{\xi})$ are related to the Matsubara modes by a canonical transformation, so that $\hat{L}_{\mathrm{MF}}(\boldsymbol{\pi}, \boldsymbol{\xi})$ can be written as a Poisson bracket [1]. Under the transformation in Eq. (4.5), the derivatives in the above expression change according to

$$\begin{aligned}\frac{\partial}{\partial\pi_k} &\to \frac{\partial}{\partial\overline{\pi}_k} \\ \frac{\partial}{\partial\xi_k} &\to \frac{\partial}{\partial\xi_k} - \mathrm{i}\sum_{j=1}^{M}\frac{\partial(\mathbf{G}\mathbf{c})_j}{\partial\xi_k}\frac{\partial}{\partial\overline{\pi}_j}.\end{aligned} \tag{B.2}$$

Expanding Eq. (B.1) in terms of the new variables and using the relation

$$\frac{\partial\mathbf{M}}{\partial x}\mathbf{M}^{-1} = -\mathbf{M}\frac{\partial\mathbf{M}^{-1}}{\partial x} \qquad \Leftrightarrow \qquad \mathbf{M}\frac{\partial\mathbf{M}^{-1}}{\partial x}\mathbf{M} = -\frac{\partial\mathbf{M}}{\partial x}, \tag{B.3}$$

which holds for any invertible matrix $\mathbf{M}$, we obtain the final expression in Eq. (4.11).

B.2 Imaginary-time symmetries

In Chapter 4, we use symmetry to derive the sufficient conditions for the mean-field Liouvillian to be real. Here we give a brief summary of the symmetry relations that lead to this result.

B.2.1 Matsubara modes

For the following derivation, it will be convenient to define Matsubara coordinates in the continuum picture as the Fourier coefficients of a path $q(\tau)$ that is periodic in imaginary time τ with period $\beta\hbar$:

$$\widetilde{Q}_n = \begin{cases} \frac{\sqrt{2}}{\beta\hbar}\int_0^{\beta\hbar} \mathrm{d}\tau\ \cos(\widetilde{\omega}_n\tau)q(\tau), & -\mu \le n < 0, \\ \frac{\sqrt{2}}{\beta\hbar}\int_0^{\beta\hbar} \mathrm{d}\tau\ \sin(\widetilde{\omega}_n\tau)q(\tau), & 0 < n \le \mu, \\ \frac{1}{\beta\hbar}\int_0^{\beta\hbar} \mathrm{d}\tau\, q(\tau), & n = 0, \end{cases} \tag{B.4}$$

where $\mu = (M-1)/2$, and M is odd. Considering the effect of imaginary-time translation, $\hat{R}_{\tau'}q(\tau) = q(\tau+\tau')$, it follows that [88]

$$\hat{R}_{\tau'}\begin{bmatrix}\widetilde{Q}_{\overline{n}} \\ \widetilde{Q}_n\end{bmatrix} = \begin{bmatrix}\cos(\widetilde{\omega}_n\tau') & \sin(\widetilde{\omega}_n\tau') \\ -\sin(\widetilde{\omega}_n\tau') & \cos(\widetilde{\omega}_n\tau')\end{bmatrix}\begin{bmatrix}\widetilde{Q}_{\overline{n}} \\ \widetilde{Q}_n\end{bmatrix}, \tag{B.5}$$

where $n > 0$ and $\overline{n} \equiv -n$. From this we conclude that

$$\frac{\mathrm{d}\widetilde{Q}_n}{\mathrm{d}\tau} = \lim_{\delta\tau\to 0}\delta\tau^{-1}[\hat{R}_{\delta\tau}\widetilde{Q}_n - \widetilde{Q}_n] = -\widetilde{\omega}_n\widetilde{Q}_{\overline{n}}, \tag{B.6}$$

which holds for all values of n, given the convention $\widetilde{\omega}_{\overline{n}} = -\widetilde{\omega}_n$ and $\widetilde{\omega}_0 = 0$. We also note that if we treat $(\widetilde{Q}_{\overline{n}}, \widetilde{Q}_n)$ as the (x, y) coordinates of a point on a two-dimensional plane, translation in imaginary time by τ' is equivalent to rotation by an angle $-\widetilde{\omega}_n\tau'$ (i.e. for positive τ', the rotation is clockwise).

Going back to the definition in Eq. (B.4), it is clear that under the reversal of imaginary time, $\hat{E}q(\tau) = q(-\tau)$, the coordinates transform as

$$\hat{E}\widetilde{Q}_{\overline{n}} = \widetilde{Q}_{\overline{n}} \qquad \text{and} \qquad \hat{E}\widetilde{Q}_n = -\widetilde{Q}_n. \tag{B.7}$$

Finally, reflection in imaginary time about a point τ', such that $\hat{\sigma}_{\tau'} q(\tau) = q(2\tau' - \tau)$, acts on the Matsubara coordinates as

$$\hat{\sigma}_{\tau'} \begin{bmatrix} \widetilde{Q}_{\bar{n}} \\ \widetilde{Q}_n \end{bmatrix} = \begin{bmatrix} \cos(2\widetilde{\omega}_n \tau') & \sin(2\widetilde{\omega}_n \tau') \\ \sin(2\widetilde{\omega}_n \tau') & -\cos(2\widetilde{\omega}_n \tau') \end{bmatrix} \begin{bmatrix} \widetilde{Q}_{\bar{n}} \\ \widetilde{Q}_n \end{bmatrix} \equiv \hat{E} \bullet \hat{R}_{2\tau'} \begin{bmatrix} \widetilde{Q}_{\bar{n}} \\ \widetilde{Q}_n \end{bmatrix}, \tag{B.8}$$

where $\bullet$ denotes composition of operations. Therefore we can deduce the behaviour of a function of Matsubara modes under reflection based on how it transforms under imaginary time translation and reversal. The centroid $\widetilde{Q}_0$ is clearly unaffected by any of these transformations. It follows that the centroid forms the basis for the Σ^+ irreducible representation of the $C_{\infty v}$ point group [132], and that pairs of modes $\widetilde{Q}_{\pm n}$ form the bases for the Π, Δ, Φ, ... irreducible representations. The momenta $\widetilde{\mathbf{P}}_M$ transform in the same way as the positions, from which it can be shown that the Matsubara phase θ_M transforms as the Σ^- irreducible representation, and that the Matsubara Hamiltonian $\mathcal{H}_M$ transforms as Σ^+.

B.2.2 Symmetrised coordinates

We now prove that it is possible to construct a set of coordinates that satisfy Eqs. (4.13) and (4.14), and discuss their symmetry properties. First, we introduce the plane polar coordinates (ρ_n, ϕ_n), such that

$$\begin{aligned} \widetilde{Q}_{\bar{n}} &= \rho_n \cos(\phi_n) & \rho_n &= \sqrt{\widetilde{Q}_{\bar{n}}^2 + \widetilde{Q}_n^2}, \\ \widetilde{Q}_n &= \rho_n \sin(\phi_n) & \phi_n &= \tan^{-1}\left(\widetilde{Q}_n / \widetilde{Q}_{\bar{n}}\right). \end{aligned} \tag{B.9}$$

Given the results of Appendix B.2.1, these transform according to

$$\begin{aligned} \hat{R}_{\tau'} \rho_n &= \rho_n & \hat{R}_{\tau'} \phi_n &= \phi_n - \widetilde{\omega}_n \tau', \\ \hat{E} \rho_n &= \rho_n & \hat{E} \phi_n &= -\phi_n, \end{aligned} \tag{B.10}$$

which is consistent with the analogy between the pair of modes $(\widetilde{Q}_{\bar{n}}, \widetilde{Q}_n)$ and a rotating vector. Next we note that

$$\psi_n = \phi_n - n\phi_1 \quad (1 < n \leq \mu) \tag{B.11}$$

satisfies

$$\hat{R}_{\tau'} \psi_n = \psi_n \qquad \text{and} \qquad \hat{E} \psi_n = -\psi_n. \tag{B.12}$$

The angles ψ_n are analogous to body-fixed angles in many-particle systems. Hence we define a set of coordinates $\{\widetilde{Q}_0,\ \rho_1,\ \phi_1,\ \rho_n,\ \psi_n \mid 1 < n \leq \mu\}$ such that

$$\begin{aligned} \widetilde{Q}_{\overline{1}} &= \rho_1 \cos(\phi_1), & \widetilde{Q}_{\overline{n}} &= \rho_n \cos(\psi_n + n\phi_1), \\ \widetilde{Q}_1 &= \rho_1 \sin(\phi_1), & \widetilde{Q}_n &= \rho_n \sin(\psi_n + n\phi_1). \end{aligned} \tag{B.13}$$

The centroid $\widetilde{Q}_0$ and the radii ρ_n $(0 < n \leq \mu)$ are invariant under imaginary-time translation and reversal. They all transform according to the Σ^+ irreducible representation of the $C_{\infty v}$ group. The angles ψ_n $(1 < n \leq \mu)$ are invariant under translation and change sign under inversion. This corresponds to the Σ^- irreducible representation. The angle ϕ_1 satisfies

$$\frac{\partial \widetilde{Q}_n}{\partial \phi_1} = n\widetilde{Q}_{\overline{n}}, \tag{B.14}$$

as per Eq. (4.13) with a proportionality constant $\alpha = -\widetilde{\omega}_1^{-1}$. Therefore this set of coordinates has exactly the symmetry properties described in Section 4.2.1. Other sets with the same symmetries can be constructed by combining even and odd functions of the Σ^+ and Σ^- coordinates. In what follows we discuss some of the properties of such symmetrised sets.

Symmetries of the momenta The momenta associated with a symmetrised set of coordinates $\boldsymbol{\xi}$, such that $\xi_\tau \in \boldsymbol{\xi}$ satisfies Eq. (4.13), are given by

$$\pi_l = \sum_n \frac{\partial \widetilde{Q}_n}{\partial \xi_l} \widetilde{P}_n. \tag{B.15}$$

To determine their symmetry, we need to know how the partial derivatives $\frac{\partial}{\partial \xi_l}$ transform under imaginary time translation and reversal. For $\xi_l \neq \xi_\tau$ it follows trivially that the corresponding irreducible representation Γ_l is the same as for the coordinate ξ_l. For $\xi_l \equiv \xi_\tau$ we observe that

$$\hat{R}_{\tau'} \frac{\partial}{\partial \xi_\tau} = \frac{\partial}{\partial(\xi_\tau + \alpha^{-1}\tau')} = \frac{\partial}{\partial \xi_\tau} \qquad \text{and} \qquad \hat{E} \frac{\partial}{\partial \xi_\tau} = -\frac{\partial}{\partial \xi_\tau}, \tag{B.16}$$

which means that $\Gamma_\tau = \Sigma^-$. Apart from the possible change of sign of the partial derivative, the sum in Eq. (B.15) is unaffected by imaginary-time transformations. Therefore $\pi_l \sim \Gamma_l$, which is to say that the momenta conjugate to Σ^+ coordinates transform as Σ^+, and the momenta conjugate to Σ^- coordinates transform as Σ^-. The remaining momentum π_τ is proportional

to the Matsubara phase θ_M,

$$\pi_\tau = \sum_n \frac{\partial \widetilde{Q}_n}{\partial \xi_\tau} \widetilde{P}_n = -\alpha \sum_n \widetilde{\omega}_n \widetilde{Q}_{\overline{n}} \widetilde{P}_n = -\alpha \theta_M, \tag{B.17}$$

and also transforms as Σ^-.

Symmetries of the metric tensor The components of the metric tensor are given by

$$G_{kl} = \sum_n \frac{\partial \widetilde{Q}_n}{\partial \xi_k} \frac{\partial \widetilde{Q}_n}{\partial \xi_l}, \tag{B.18}$$

and are clearly invariant under imaginary-time translation. It is also clear that a component G_{kl} is symmetric under imaginary-time reversal if both ξ_k and ξ_l change sign or remain the same, and is antisymmetric otherwise. This can be summarised as

$$\Gamma_{kl} = \Gamma_k \otimes \Gamma_l, \tag{B.19}$$

where Γ_{kl} is the irreducible representation that characterises G_{kl}, and the product $\Gamma_k \otimes \Gamma_l$ is given by

$$\begin{aligned} \Sigma^+ \otimes \Sigma^+ &= \Sigma^+ & \Sigma^+ \otimes \Sigma^- &= \Sigma^-, \\ \Sigma^- \otimes \Sigma^+ &= \Sigma^- & \Sigma^- \otimes \Sigma^- &= \Sigma^+. \end{aligned} \tag{B.20}$$

B.2.3 Symmetrised Liouvillian

For a symmetrised set of coordinates that satisfy Eqs. (4.13) and (4.14), the part of the Matsubara Liouvillian defined in Eq. (4.11) simplifies to

$$\mathrm{Re}\{\mathcal{L}_a\} = \sum_{k \in a} \left(\frac{\partial \overline{\mathcal{H}}_M}{\partial \overline{\pi}_k} \frac{\partial}{\partial \xi_k} - \frac{\partial \overline{\mathcal{H}}_M}{\partial \xi_k} \frac{\partial}{\partial \overline{\pi}_k} + \alpha^{-2} \frac{\partial G_{k\tau}}{\partial \xi_\tau} \frac{\partial}{\partial \overline{\pi}_k} \right), \tag{B.21a}$$

$$\mathrm{Im}\{\mathcal{L}_a\} = 2 \sum_{k \in a} \sum_{j=1}^{M} \left(\mathbf{G}^{-1} \overline{\boldsymbol{\pi}} \right)_j \left[\sum_{|n| \leq \mu} \widetilde{\omega}_n \frac{\partial \widetilde{Q}_n}{\partial \xi_j} \frac{\partial \widetilde{Q}_{\overline{n}}}{\partial \xi_k} \right] \frac{\partial}{\partial \overline{\pi}_k}. \tag{B.21b}$$

We have already shown that the metric tensor $\mathbf{G}$ is invariant under τ-translation. It follows that $\frac{\partial G_{k\tau}}{\partial \xi_\tau} = 0$, and so the last term in Eq. (B.21a) vanishes. The Hamiltonian $\overline{\mathcal{H}}_M$ has Σ^+ symmetry, and if we insist that all of $\xi_{k \in a}$ are also Σ^+, then Eq. (B.21a) is Σ^+ overall and survives mean-fielding. To determine the symmetry of the imaginary term in Eq. (B.21b), we

use

$$G_{kl}^{-1} = \sum_n \frac{\partial \xi_k}{\partial \widetilde{Q}_n} \frac{\partial \xi_l}{\partial \widetilde{Q}_n}, \tag{B.22}$$

which allows us to write

$$\begin{aligned} \mathrm{Im}\{\mathcal{L}_a\} &= 2 \sum_{k\in a} \sum_{n,n'} \sum_{l,j=1}^{M} \widetilde{\omega}_n \overline{\pi}_l \frac{\partial \xi_l}{\partial \widetilde{Q}_{n'}} \frac{\partial \xi_j}{\partial \widetilde{Q}_{n'}} \frac{\partial \widetilde{Q}_n}{\partial \xi_j} \frac{\partial \widetilde{Q}_{\overline{n}}}{\partial \xi_k} \frac{\partial}{\partial \overline{\pi}_k} \\ &= 2 \sum_{k\in a} \sum_{n} \sum_{l=1}^{M} \widetilde{\omega}_n \overline{\pi}_l \frac{\partial \xi_l}{\partial \widetilde{Q}_n} \frac{\partial \widetilde{Q}_{\overline{n}}}{\partial \xi_k} \frac{\partial}{\partial \overline{\pi}_k} = 2 \sum_{k\in a} \left[\sum_n \widetilde{\omega}_n \frac{\partial \widetilde{Q}_{\overline{n}}}{\partial \xi_k} \overline{P}_n \right] \frac{\partial}{\partial \overline{\pi}_k}, \end{aligned} \tag{B.23}$$

where $\overline{\mathbf{P}}_M$ are the Matsubara counterparts of the analytically-continued curvilinear momenta $\overline{\boldsymbol{\pi}}$. Comparing the expression in brackets to Eq. (B.17) we conclude that the imaginary part of the Matsubara Liouvillian is Σ^- and must therefore vanish under mean-fielding.

B.3 Polar quasicentroids

B.3.1 Instantons in a two-dimensional rotor

In Section 4.2.2 we claim that constraining a ring-polymer at an average radius and angle prevents it from stretching into an instanton. We now prove this for a two-dimensional rotor described by the centrosymmetric potential $V(r)$. Expressed in polar coordinates, the ring-polymer potential energy is

$$W_N(\mathbf{r}, \boldsymbol{\theta}) = \frac{1}{N} \sum_{l=1}^{N} \left\{ V(r_l) + \frac{m\omega_N^2}{2} [r_l^2 + r_{l+1}^2 - 2 r_l r_{l+1} \cos(\theta_l - \theta_{l+1})] \right\}. \tag{B.24}$$

We will minimise $W_N(\mathbf{r}, \boldsymbol{\theta})$ subject to the conditions in Eq. (4.21). Introducing the "normal-mode" coordinates $\mathbf{R}$, $\boldsymbol{\Theta}$ from Eq. (A.55) we expand W_N in a Taylor series about

$$R_0 = R \qquad \Theta_0 = \Theta$$

and truncate at second order in $R_{n\neq 0}$ and $\Theta_{n\neq 0}$, to get

$$W_N(\mathbf{r}, \boldsymbol{\theta}) \sim V(R) + \sum_{n\neq 0} \left\{ \left[\frac{1}{2} \frac{\mathrm{d}^2 V}{\mathrm{d}R^2} + \frac{m\omega_n^2}{2} \right] R_n^2 + \frac{m\omega_n^2}{2} R^2 \Theta_n^2 \right\} \tag{B.25}$$

It follows that at the point where the ring polymer is about to form an instanton,

$$\frac{\partial W_N}{\partial \Theta_n} = m\omega_n^2 R^2 \Theta_n = 0, \qquad (n \neq 0) \tag{B.26}$$

i.e. the minimum-energy configuration will not have a spread in the angular degrees of freedom. Similarly for the radial degrees of freedom

$$\frac{\partial W_N}{\partial R_n} = \frac{\mathrm{d}^2 V}{\mathrm{d}R^2} R_n + m\omega_n^2 R_n = 0 \quad \Rightarrow \quad R_n = 0 \quad \text{or} \quad -\frac{d^2 V}{dR_0^2} = m\omega_n^2, \qquad (n \neq 0). \tag{B.27}$$

Therefore an instanton can only form when the radial curvature of the potential is below $-4\pi^2 m/\beta^2\hbar^2$. Polar quasicentroids have been chosen to approximate the vibrational dynamics of bound atoms, for which we can expect the curvature to be positive in thermally accessible regions. For example, the smallest radius of negative curvature in the Morse potential of Eq. (3.22) is

$$r_c = r_{\mathrm{eq}} + \frac{\ln 2}{\alpha} \approx 2.43 \text{ a.u.} \tag{B.28}$$

This is well outside the thermally accessible region at any of the temperatures considered in this work, and we should therefore see no spurious instantons in quasicentroid distributions.

B.3.2 Polar mean-field Hamiltonian

Consider the curvilinear coordinates $\boldsymbol{\xi} = \{r_l,\ \theta_l \mid l = 1, \ldots, N\}$ defined in Eq. (4.22), with the corresponding momenta

$$\pi_l^{(r)} = [\mathbf{q}_l \cdot \mathbf{p}_l]/r_l \qquad\qquad \pi_l^{(\theta)} = \mathbf{q}_l \times \mathbf{p}_l. \tag{B.29}$$

We wish to calculate the mean-field Hamiltonian

$$\mathrm{e}^{-\beta \mathscr{H}_{\mathrm{MF}}(\pi_R, \pi_\Theta, R_0, \Theta_0)} = \lim_{N\to\infty} \frac{1}{(2\pi\hbar)^{2N-2}} \int \mathrm{d}^N \boldsymbol{\pi}_r \int \mathrm{d}^N \boldsymbol{\pi}_\theta \int \mathrm{d}^N \mathbf{r} \int \mathrm{d}^N \boldsymbol{\theta}\, \mathrm{e}^{-\beta[T_N(\boldsymbol{\pi},\boldsymbol{\xi}) + W_N(\boldsymbol{\xi})]}$$
$$\delta\left(\frac{1}{N}\sum_{l=1}^N \pi_l^{(r)} - \pi_R\right) \delta\left(\frac{1}{N}\sum_{l=1}^N \pi_l^{(\theta)} - \pi_\Theta\right) \delta\left(\frac{1}{N}\sum_{l=1}^N r_l - R_0\right) \delta\left(\frac{1}{N}\sum_{l=1}^N \theta_l - \Theta_0\right). \tag{B.30}$$

The integral over the momenta can be performed analytically. First we write the kinetic energy as

$$T_N(\boldsymbol{\pi}, \boldsymbol{\xi}) = \frac{1}{2mN} \left[\boldsymbol{\pi}_r^\top \mathbf{I}_N \boldsymbol{\pi}_r + \boldsymbol{\pi}_\theta^\top \mathbf{D} \boldsymbol{\pi}_\theta\right], \tag{B.31}$$

where $\mathbf{I}_N$ is the $N \times N$ identity matrix, and

$$\mathbf{D} = \operatorname{diag}\left[r_1^{-2} \dots r_N^{-2}\right]. \tag{B.32}$$

Next, we introduce the "normal-mode" coordinates

$$\Pi_n^{(r)} = \frac{1}{\sqrt{N}} \sum_{l=1}^{N} T_{ln} \pi_l^{(r)} \qquad \Pi_n^{(\theta)} = \frac{1}{\sqrt{N}} \sum_{l=1}^{N} T_{ln} \pi_l^{(\theta)}, \tag{B.33}$$

which allows us to explicitly impose the constraint in Eq. (B.30). Under this transformation,

$$T_N(\mathbf{\Pi}, \boldsymbol{\xi}) = \frac{1}{2m} \left[\mathbf{\Pi}_r^\top \mathbf{I}_N \mathbf{\Pi}_r + \mathbf{\Pi}_\theta^\top \widetilde{\mathbf{D}} \mathbf{\Pi}_\theta \right], \tag{B.34}$$

where

$$\widetilde{\mathbf{D}} = \mathbf{T}^\top \mathbf{D} \mathbf{T}. \tag{B.35}$$

The integral over $\mathbf{\Pi}_r$ factorises straightforwardly. It evaluates to

$$\begin{aligned} &\int \mathrm{d}^N \boldsymbol{\pi}_r \, \mathrm{e}^{-\frac{\beta_N}{2m} \boldsymbol{\pi}_r^\top \mathbf{I}_N \boldsymbol{\pi}_r} \delta\left(\frac{1}{N} \sum_{l=1}^{N} \pi_l^{(r)} - \pi_R \right) = \\ &\qquad N^{N/2} \mathrm{e}^{-\beta \pi_R^2 / 2m} \prod_{n \neq 0} \left(\int_{-\infty}^{\infty} \mathrm{d}\Pi_n^{(r)} \mathrm{e}^{-\beta [\Pi_n^{(r)}]^2 / 2m} \right) = N^{N/2} \mathrm{e}^{-\beta \pi_R^2 / 2m} \left(\frac{2\pi m}{\beta} \right)^{(N-1)/2}. \end{aligned} \tag{B.36}$$

The integral over $\mathbf{\Pi}_\theta$ can be factorised by performing a block-LDU decomposition of $\widetilde{\mathbf{D}}$ (see Appendix D.2 and [49, pp. 415–420]). It evaluates to

$$\int \mathrm{d}^N \boldsymbol{\pi}_\theta \, \mathrm{e}^{-\frac{\beta_N}{2m} \boldsymbol{\pi}_\theta^\top \mathbf{D} \boldsymbol{\pi}_\theta} \delta\left(\frac{1}{N} \sum_{l=1}^{N} \pi_l^{(\theta)} - \pi_\Theta \right) = N^{N/2} \mathrm{e}^{-\beta \pi_\Theta^2 / 2m \rho^2} \rho^{-1} |\widetilde{\mathbf{D}}|^{-1/2} \left(\frac{2\pi m}{\beta} \right)^{(N-1)/2}, \tag{B.37}$$

where ρ is the root-mean-square radius in Eq. (4.24). The matrix $\widetilde{\mathbf{D}}$ is related to $\mathbf{D}$ by an orthogonal transformation, and so

$$|\widetilde{\mathbf{D}}| = |\mathbf{D}| = \prod_{l=1}^{N} r_l^{-2}. \tag{B.38}$$

Combined, these results produce the final expression in Eq. (4.23).

B.3.3 Approximations to the Liouvillian

In Section 4.2.2 we say that the exact mean-field Hamiltonian can be approximated so that it becomes separable when expressed in terms of the Cartesian quasicentroids in Eq. (4.25). To see why this is a good approximation, consider the root-mean-square radius $\rho(\mathbf{r})$ defined in Eq. (4.24). Using the normal-mode coordinates from Eq. (A.55) we get

$$\rho(\mathbf{r}) = R^2 + y^2, \qquad \text{with} \qquad y^2 \equiv \sum_{n\neq 0} (R_n/R)^2. \tag{B.39}$$

We can expand the ρ-dependent part of the integrand in Eq. (4.23) in a Taylor series about $y = 0$ to give

$$\rho(\mathbf{r}')^{-1} \mathrm{e}^{-\beta T(\pi_R, \pi_\Theta, \rho(\mathbf{r}'))} = R^{-1} \mathrm{e}^{-\beta T(\pi_R, \pi_\Theta, R)} \left[1 + y^2 \left(\frac{\beta \pi_\Theta^2}{2mR^2} - 1 \right) + O(y^4) \right]. \tag{B.40}$$

The approximation in Eq. (4.26) corresponds to truncating this series at the first term, which is justified so long as the radial centroid of the ring-polymer distribution is large compared to its spread. Furthermore, the thermal averages of functions of R and Θ are unaffected by this truncation, which indicates that the coefficient of the neglected terms are on average small.

Using this approximation to factorise the kinetic energy allows us to define the mean-field potential $\mathscr{F}_{\mathrm{MF}}$, such that

$$\begin{aligned} \mathrm{e}^{-\beta \mathscr{F}_{\mathrm{MF}}(R,\Theta)} =& N \left(\frac{m}{2\pi \beta_N \hbar^2} \right)^{N-1} \int \mathrm{d}^N \mathbf{r}' \int \mathrm{d}^N \boldsymbol{\theta}' \times \\ & [J(\mathbf{r}')/R] \, \mathrm{e}^{-\beta [V_N(\mathbf{r}', \boldsymbol{\theta}) + \widetilde{S}_N(\mathbf{r}', \boldsymbol{\theta}')]} \, \delta(R' - R) \, \delta(\Theta' - \Theta) \end{aligned} \tag{B.41}$$

The corresponding forces contain contributions from the external potential $V_N(\mathbf{r}, \boldsymbol{\theta})$, the springs $\widetilde{S}_N(\mathbf{r}, \boldsymbol{\theta})$, and the Jacobian $J(\mathbf{r})/R$. We will now show that for a centrosymmetric potential $V_N(\mathbf{r})$ the spring and the Jacobian contributions cancel each other almost exactly. In this case, integration over the angles in Eq. (B.41) can be performed analytically. Following Kleinert [133, pp. 697–699] we get

$$\begin{aligned} \mathrm{e}^{-\beta \mathscr{F}_{\mathrm{MF}}(R)} \propto R^{-1} \int \mathrm{d}^N \mathbf{r}' \, \delta(R' - R) \sum_{M=-\infty}^{\infty} \prod_{l=1}^{N} \tilde{I}_M \left(\frac{m r_l' r_{l+1}'}{\beta_N \hbar^2} \right) \times \\ \exp \left\{ -\beta_N \sum_{l=1}^{N} \left(V(r_l') + \frac{m\omega_N^2}{2} [r_l' - r_{l+1}']^2 \right) \right\}, \end{aligned} \tag{B.42}$$

where we omit the proportionality constant and use Kleinert's notation for the weighted modified Bessel functions $\tilde{I}_M$. Provided that the potential $V(r)$ is strongly repulsive at the origin, so that contributions from $r_l \to 0$ are negligible, we may use the first term in the asymptotic expansion

$$\tilde{I}_M(z) \xrightarrow{z\to\infty} \mathrm{e}^{-(M^2-1/4)/2z} + \cdots \tag{B.43}$$

to simplify the expression

$$\lim_{N\to\infty} \sum_{M=-\infty}^{\infty} \prod_{l=1}^{N} \tilde{I}_M\left(\frac{m r_l r_{l+1}}{\beta_N \hbar^2}\right) = \mathrm{e}^{f(\mathbf{r})/4}\theta_3(0|\mathrm{i}f(\mathbf{r})/\pi), \tag{B.44}$$

where

$$f(\mathbf{r}) = \lim_{N\to\infty} \frac{\beta_N\hbar^2}{2m} \sum_{l=1}^{N} \frac{1}{r_l r_{l+1}} = \lim_{N\to\infty} \frac{\beta_N\hbar^2}{2m} \sum_{l=1}^{N} r_l^{-2} \tag{B.45}$$

and

$$\theta_3(z|\tau) = 1 + 2\sum_{M=1}^{\infty} \mathrm{e}^{\mathrm{i}M^2\pi\tau}\cos(2Mz) \tag{B.46}$$

is the third Jacobi theta function with lattice parameter τ [Eq. 20.2.3 in 134]. We may use the lattice transformation [Eq. 20.7.32 in 134],

$$\theta_3(z|\tau) = (-\mathrm{i}\tau)^{-1/2}\mathrm{e}^{-\mathrm{i}z^2/\pi\tau}\theta_3(-z/\tau|-1/\tau) \tag{B.47}$$

to approximate

$$\theta_3(0|\mathrm{i}f(\mathbf{r})/\pi) = \sqrt{\frac{\pi}{f(\mathbf{r})}}\,\theta\big(0|\mathrm{i}\pi/f(\mathbf{r})\big) = \sqrt{\frac{\pi}{f(\mathbf{r})}}\left[1 + 2\sum_{M=1}^{\infty}\mathrm{e}^{-M^2\pi^2/f(\mathbf{r})}\right] \approx \sqrt{\frac{\pi}{f(\mathbf{r})}}. \tag{B.48}$$

This is an extremely accurate approximation for values of $\mathbf{r}$ that contribute significantly to the mean-field force calculations in Section 4.3 (relative error less than 10^{-12}). With these simplifications, the mean-field force can be written as

$$-\frac{\partial \mathscr{F}_{\mathrm{MF}}}{\partial R} = -\frac{1}{Z(R)}\left\langle \frac{1}{\beta R} + \frac{1}{\beta}\left(\frac{1}{2f(\mathbf{r}')} - \frac{1}{4}\right)\frac{\partial f(\mathbf{r}')}{\partial R'} + \frac{\partial V_N(\mathbf{r}')}{\partial R'}\right\rangle, \tag{B.49}$$

where

$$\langle\cdots\rangle = \int \mathrm{d}^N\mathbf{r}'\,(\cdots)\sqrt{\frac{\pi}{f(\mathbf{r}')}}\mathrm{e}^{f(\mathbf{r}')/4}\exp\left\{-\beta_N\sum_{l=1}^{N}\left(V(r_l') + \frac{m\omega_N^2}{2}[r_l' - r_{l+1}']^2\right)\right\}\delta(R'-R) \tag{B.50}$$

Expanding in a Taylor series about $r_l = R$ gives

$$\begin{aligned} &\frac{1}{Z(R)}\left\langle \frac{1}{\beta R} + \frac{1}{\beta}\left(\frac{1}{2f(\mathbf{r}')} - \frac{1}{4}\right)\frac{\partial f(\mathbf{r}')}{\partial R'}\right\rangle \\ &= \frac{\hbar^2}{4mR^3} + \frac{1}{Z(R)}\left\langle \frac{3y^2}{\beta R}\left(\frac{\beta\hbar^2}{2mR^2} - 1\right) + O(y^3)\right\rangle, \end{aligned} \tag{B.51}$$

where y is defined in Eq. (B.39). The first term is a quantum mechanical correction to the centrifugal barrier [Eq. 8.21 in 133]. For systems considered in this work it can be safely neglected. The remaining term is second order in y and can also be neglected, provided that the bead distribution is radially compact. Once the corresponding terms are removed from Eq. (B.49), Eq. (4.27) follows directly.

B.4 Simulation details

To calculate the mean-field averages of the radial quasicentroid force in Eq. (4.33), we ran constrained PIMD simulations with the quasicentroid radius R fixed at values spanning a regular grid of 128 points between 1.5 and 2.5 a.u, and the angle Θ fixed at 0. At each point we ran a single trajectory that was first equilibrated for 0.5 ps and then propagated for 50 ps under a PILE-L thermostat with friction

$$\gamma_n = \begin{cases} 0.01\ \mathrm{fs}^{-1} & \text{if } n = 0, \\ |\omega_n| & \text{otherwise.} \end{cases}$$

The number of beads used at the different temperatures is the same as in Table A.2. To integrate the constrained equations of motion we used the OBABO scheme proposed by Leimkuhler and Matthews [110], where the letters denote the sequence of operations needed to propagate the system through a single time step and have the following meaning:

O. Propagate the ring-polymer momenta for $\Delta t/2$ under the PILE-L thermostat [92], followed by RATTLE [109] to constrain the quasicentroid components.

B. Propagate the momenta for $\Delta t/2$ under the forces derived from the ring-polymer potential $W_N(\mathbf{q})$, followed by RATTLE.

A. Propagate the ring-polymer positions for Δt according to the current values of the momenta, followed by SHAKE [108] to constrain the quasicentroid coordinates at the specified values.

The resulting mean-field forces were interpolated with cubic splines and used for the QCMD simulations in Section 4.3. The QCMD simulations followed the procedure outlined in Appendix A.6.2, with a total of 8 independent trajectories propagated at each temperature. Each one was first equilibrated for 10 ps under a Langevin thermostat with friction $\gamma_0 = 0.01$ fs^{-1} and then propagated for a total of 10^5 sampling intervals of 2 ps, separated by relaxation intervals of 0.5 ps, using an integration time step $\Delta t = 0.2$ fs.

Appendix C

Vibrational dynamics of water

C.1 Quasicentroid torque

To arrive at the alternative approximation to the quasicentroid torque we rewrite the rotational Eckart condition in Eq. (5.3b) as

$$\sum_{\alpha} m_{\alpha} \overline{\mathbf{D}}^{(\alpha)} \times \widetilde{\mathbf{D}}^{(\alpha)} = \mathbf{0}, \tag{C.1}$$

where

$$\overline{\mathbf{D}}^{(\alpha)} = \overline{\mathbf{Q}}^{(\alpha)} - \overline{\mathbf{Q}}^{(c)}, \qquad \widetilde{\mathbf{D}}^{(\alpha)} = \widetilde{\mathbf{Q}}_0^{(\alpha)} - \widetilde{\mathbf{Q}}_0^{(c)}, \tag{C.2}$$

and $\overline{\mathbf{Q}}^{(c)} = \widetilde{\mathbf{Q}}_0^{(c)}$ is the (quasi-)centroid centre of mass. We then differentiate Eq. (C.1) twice with respect to time,

$$\sum_{\alpha} m_{\alpha} \ddot{\overline{\mathbf{D}}}^{(\alpha)} \times \widetilde{\mathbf{D}}^{(\alpha)} = \sum_{\alpha} m_{\alpha} \ddot{\overline{\mathbf{D}}}^{(\alpha)} \times \overline{\mathbf{D}}^{(\alpha)} - 2 \sum_{\alpha} \frac{1}{m_{\alpha}} \overline{\mathbf{P}}^{(\alpha)} \times \widetilde{\mathbf{P}}^{(\alpha)}, \tag{C.3}$$

and use Newton's second law to write

$$m_{\alpha} \ddot{\overline{\mathbf{D}}}^{(\alpha)} = -\frac{\partial V_N(\mathbf{q})}{\partial \widetilde{\mathbf{Q}}_0^{(\alpha)}}. \tag{C.4}$$

According to our approximations in Eqs. (5.4) and (5.5), quasicentroids *undergoing mean-field dynamics* satisfy

$$m_{\alpha} \ddot{\overline{\mathbf{D}}}^{(\alpha)} = \frac{1}{\overline{Z}(\overline{\mathbf{Q}})} \left\langle -\frac{\partial V_N(\mathbf{q})}{\partial \overline{\mathbf{Q}}^{(\alpha)}} \right\rangle_{\overline{\mathbf{Q}}}. \tag{C.5}$$

Hence we write the non-mean-field quasicentroid acceleration as

$$m_\alpha \ddot{\overline{\mathbf{D}}}^{(\alpha)} = -\frac{\partial V_N(\mathbf{q})}{\partial \overline{\mathbf{Q}}^{(\alpha)}} + \ldots, \tag{C.6}$$

where (...) denotes terms that vanish under mean-fielding, which we will ignore. Similarly, we expect the last term of Eq. (C.3) to vanish under mean-fielding, as none of the remaining quantities depend on momenta. Equation (C.3) then becomes

$$-\sum_\alpha \frac{\partial V_N(\mathbf{q})}{\partial \overline{\mathbf{Q}}^{(\alpha)}} \times \widetilde{\mathbf{D}}^{(\alpha)} \sim -\sum_\alpha \frac{\partial V_N(\mathbf{q})}{\partial \widetilde{\mathbf{Q}}_0^{(\alpha)}} \times \overline{\mathbf{D}}^{(\alpha)}, \tag{C.7}$$

where "$\sim$" means that the two sides are approximately equal under mean-fielding. We then expand the quasicentroid forces as in Eq. (5.10), getting after cancellation

$$\sum_\alpha \left[\overline{\mathbf{f}}_{\text{int}}^{(\alpha)} + m_\alpha \left(\mathbf{I}^{-1}\overline{\boldsymbol{\tau}}\right) \times \overline{\mathbf{D}}^{(\alpha)}\right] \times \widetilde{\mathbf{D}}^{(\alpha)} \sim -\sum_\alpha \frac{\partial V_N(\mathbf{q})}{\partial \widetilde{\mathbf{Q}}_0^{(\alpha)}} \times \overline{\mathbf{D}}^{(\alpha)}. \tag{C.8}$$

Finally, rearranging the vector triple product on the left-hand side leads to Eqs. (5.17) and (5.18).

C.2 Convergence of AQCMD spectra for water

Convergence of the AQCMD infrared absorption spectra with respect to the adiabatic separation γ at 600 and 300 K was tested by simulating liquid water using a box of 32 molecules, subject to periodic boundary conditions [48, 49]. The simulated spectra converged at $\gamma = 8$ and 32 respectively, as shown in Figure C.1.

The convergence with respect to γ for ice at 150 K had to be tested using a larger simulation box of 96 molecules, in order to ensure a zero net dipole moment [135]. The highest value tested was $\gamma = 128$, which was sufficient to converge the positions of all the bands in the spectrum, but not the relative intensity of the bend and stretch bands (see Figure C.1). However, the dipole-derivative TCF was converged for $t = 0$ already at $\gamma = 64$. This, together with the abrupt nature of convergence at 300 K, suggests that the $\gamma = 128$ spectrum is close to convergence at 150 K.

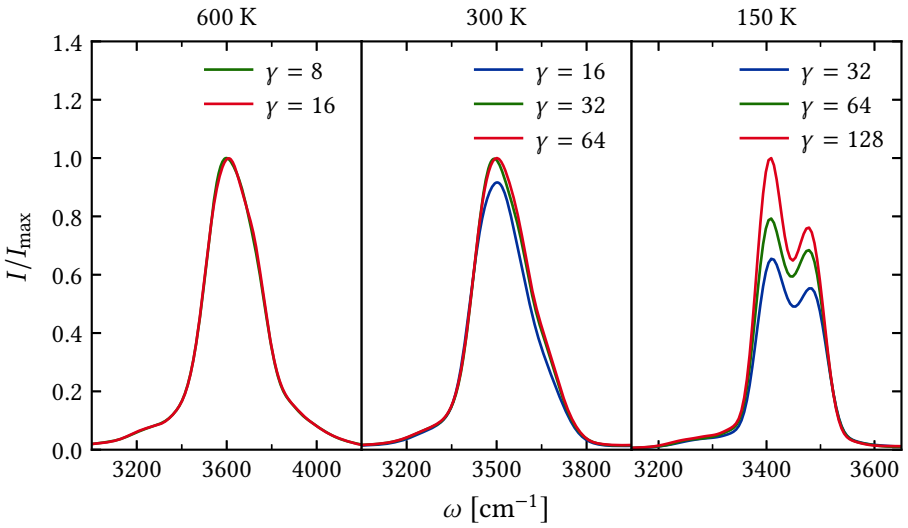

Figure C.1 Simulated infrared absorption spectra in the OH-stretch region of q-TIP4P/F water at 600, 300, and 150 K, calculated with the AQCMD algorithm of Section 5.1.3 at different levels of adiabatic separation γ. In all cases the position of the absorption maximum remains largely unchanged with increasing γ, and only the intensity is noticeably affected. The spectrum at 300 K demonstrates that convergence of the intensity may be quite abrupt, and similar behaviour is anticipated at 150 K.

C.3 Simulation details

C.3.1 Gaseous water

PIMD calculations To calculate the mean-field forces for the CMD and QCMD simulations in Section 5.2 we ran a set of constrained PIMD trajectories on a $64 \times 64 \times 64$ grid in the (quasi-)centroid OH bond lengths and bond angle, R_1, R_2, and Θ. At each grid point we propagated a single trajectory subject to a PILE-L thermostat, using the same friction parameters and means of imposing the constraints as described in Appendix B.4. All other simulation parameters are summarised in Table C.1.

Dynamics simulations To calculate the time-correlation functions that yielded the spectra in Figure 5.2, we ran a set of 50 independent trajectories for each of TRPMD, CMD, and QCMD. Each trajectory was equilibrated for 1500 fs, followed by a series of 1000 production intervals of 2000 fs, separated by relaxation intervals of 300 fs. The (quasi-)centroid thermostat was turned off during the production intervals, and turned back on for equilibration and relaxation.

Table C.1 PIMD simulation parameters for calculating the mean-field QCMD and CMD forces for Partridge–Schwenke gaseous water.

T/K	150	300	600
N	64	32	16
$(R_{\min}, R_{\max})$/a.u.	(1.65, 2.05)	(1.50, 2.50)	(1.50, 2.50)
$(\Theta_{\min}, \Theta_{\max})$	(90°, 126°)	(85°, 130°)	(85°, 130°)
Δt/fs	0.05	0.10	0.10
t_{prod}/ps	5	10	10

The TCF samples from each of the production intervals were time-averaged as described in Appendix A.6.2. TRPMD simulations used a PILE-L thermostat with frictions

$$\gamma_n = \begin{cases} 0.01\ \text{fs}^{-1} & \text{if } n = 0, \\ |\omega_n| & \text{otherwise,} \end{cases}$$

and an integration time step $\Delta t = 0.1$ fs. The number of ring-polymer beads at the different temperatures was the same as for the PIMD simulations in Table C.1. CMD and QCMD simulations used a Langevin thermostat with friction $\gamma_0 = 0.01\ \text{fs}^{-1}$ and an integration time step $\Delta t = 0.2$ fs, with the mean-field forces obtained by cubic spline interpolation of the pre-calculated values.

C.3.2 Liquid water and ice

Liquid water Simulations of the hot compressed liquid (600 K) and the liquid at ambient conditions (300 K) were carried out using a cubic cell of 128 molecules subject to periodic boundary conditions [48, 49]. The cell length was set to 34.1351 a.u. at 600 K and 29.5958 a.u. at 300 K. At each temperature we initialised 8 independent trajectories starting from a set of water molecules on a *bcc* lattice, with their orientations randomised. Each trajectory was propagated under a global Langevin thermostat for 100 ps [92, 102]. The resulting configurations were then converted into collapsed ring polymers of 16 beads at 600 K and 32 beads at 300 K. These were propagated under the PILE-G thermostat [92] for a further 100 ps, to yield the equilibrated starting configurations for the path-integral simulations.

The TRPMD and CMD time-correlation functions were calculated by propagating the equilibrated configurations for a further 100 ps under the PILE-G thermostat. For CMD

we used the partially adiabatic algorithm with an adiabaticity constant $\gamma = 4$. The QCMD time-correlation functions were calculated by propagating the equilibrated configurations for 35 ps according to the procedure set out in Section 5.1.3, with an adiabaticity constant $\gamma = 8$ at 600 K and $\gamma = 32$ at 300 K. The ring polymers were subject to a PILE-L thermostat [92], and the quasicentroids were subject to a global Langevin thermostat, to ensure proper sampling. The first 10 ps of each QCMD trajectory were discarded prior to the calculation of the TCF.

Throughout the simulation the PILE thermostats were set up to have non-centroid frictions $\gamma_n = \lambda \times 2\omega_n$, where ω_n are the normal-mode frequencies from Eq. (2.44) in the case of TRPMD, and the adiabatic frequency from Eq. (5.19) in the case of (Q)CMD. The values of the parameter λ, the (quasi-)centroid friction γ_0, and the simulation time step Δt are summarised in Table C.2.

Table C.2 Simulation parameters for calculating the infrared absorption spectra of q-TIP4P/F liquid water.

	CMD	TRPMD	QCMD[a]	
			QC	RP
λ	0.01	0.5	—	0.5
$\gamma_0/\mathrm{fs}^{-1}$	0.01	0.01	0.01	0.01γ
$\Delta t/\mathrm{fs}$	$0.1/\gamma$	0.1	$0.1/\gamma$	

[a] QC and RP denote the quasicentroid and ring-polymer subsystems respectively.

Ice $\mathbf{I_h}$ Simulations of ice I_h were carried out using an orthorhombic cell with sides $a = 25.6156$, $b = 29.5783$, and $c = 27.8867$, all in atomic units. The initial configuration was the same as used by Willatt [88]. Alternatively, we could have used one of the optimised configurations suggested by Hayward and Reimers [135]. The key point is that the configuration has to satisfy the Bernal–Fowler ice rules [136] and possess a zero net dipole moment. Starting from this configuration, we propagated 15 independent trajectories, first using classical dynamics, and then TRPMD with $N = 64$ ring-polymer beads. The simulation parameters for this equilibration were the same as for the liquid. Eight of the equilibrated configurations were then used to initialise 100 ps long TRPMD and CMD trajectories that were propagated using the same simulation parameters as for the liquid.

For the QCMD simulation we took all 15 of the thermalised ring-polymer configurations and further equilibrated them using the adiabatic algorithm of Section 5.1.3 ($\gamma = 128$), with a PILE-L thermostat acting on the ring polymer and a *local* Langevin thermostat acting on

the quasicentroids. Equilibration was followed by a series of three production intervals, each lasting 2.5 ps, with a global Langevin thermostat acting on the quasicentroids. These intervals were separated by periods of relaxation, during which a local Langevin thermostat acted on the quasicentroids for 300 fs. A PILE-L thermostat was acting on the ring polymers throughout the simulation, with the thermostat friction and integration time step set to the values in Table C.2.

LMon-4 and TRPMD+GLE(C) For completeness, in Figure C.2 we look at the full range of frequencies covered by the simulated QCMD, TRPMD+GLE(C) and LMon-4 spectra. The stretch regions of these spectra are plotted separately in Figure 5.5 and discussed in Section 5.3.2. As mentioned in Section 5.3.2, LMon-4 and TRPMD+GLE(C) provide poor descriptions of the libration band, which is why we did not consider the entire range of frequencies in the main body of this work.

To calculate the TRPMD+GLE(C) spectra, we took 8 equilibrated starting configurations and propagated them for 100 ps using the i-PI simulation package [127]. The simulation parameters were the same as used by Rossi *et al.* in Ref. [84].

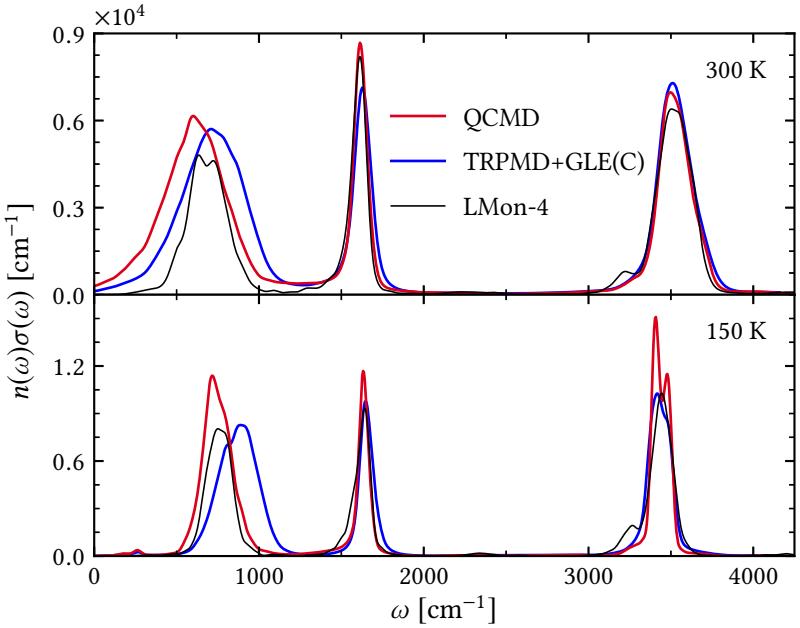

Figure C.2 Simulated infrared spectra from Figure 5.5, showing the libration and bend regions.

To calculate the smooth LMon-4 spectra we needed to post-process the raw output data, which consisted of a list of square transition dipole moments μ_i^2 at discrete frequencies ω_i. To convert the dipole-derivative ACFs into spectra, the path-integral calculations used Eq. (5.23)

with a Hann window [98]

$$f(t) = \begin{cases} \cos^2\left(\frac{\pi t}{2w}\right) & |t| \leq w, \\ 0 & |t| > w, \end{cases} \tag{C.9}$$

where w is the width of the window. Therefore, to be consistent with these results, we calculated the discrete convolution of the raw LMon-4 data with the Fourier transform of the Hann window:

$$n(\omega)\sigma(\omega) \propto \sum_i \mu_i^2 \tilde{f}(\omega - \omega_i) \qquad \text{where} \qquad \tilde{f}(\omega) = \frac{\sin(\omega w)}{\omega[1 - (\omega w/\pi)^2]}. \tag{C.10}$$

The proportionality constant was chosen to match the QCMD spectrum integrated between 2600 and 4500 cm^{-1}.

Appendix D

Useful mathematical relations

This details the mathematical relations used in some of our derivations. Appendix D.1 lists several integrals involving the multivariate Gaussian distribution. Appendix D.2 looks at the block-LDU factorisation of a matrix, where L denotes a unit lower triangular matrix, U is unit upper triangular, and D is a direct sum of two square matrices (and therefore block-diagonal).

D.1 Multivariate Gaussian integrals

Consider the integral

$$I(\mathbf{A},\mathbf{b}) = \int_{\mathbb{R}^N} \mathrm{d}^N\mathbf{x}\, \exp\left\{-\beta\left[\frac{1}{2}\mathbf{x}^\top\mathbf{A}\mathbf{x} - \mathbf{b}^\top\mathbf{x}\right]\right\} \tag{D.1}$$

where $\mathbf{A}$ is a symmetric positive definite matrix that is diagonalised by a real orthogonal transformation $\mathbf{U}$,

$$\mathbf{U}^\top\mathbf{A}\mathbf{U} = \mathrm{diag}(\lambda_1,\ldots,\lambda_N) \equiv \mathbf{\Lambda}. \tag{D.2}$$

Let us define

$$\mathbf{U}^\top\mathbf{x} \equiv \mathbf{y}, \qquad \mathbf{U}^\top\mathbf{b} \equiv \mathbf{v}, \tag{D.3}$$

so that

$$\frac{1}{2}\mathbf{x}^\top\mathbf{A}\mathbf{x} - \mathbf{b}^\top\mathbf{x} = \sum_{l=1}^{N}\left[\frac{1}{2}\lambda_l y_l^2 - v_l y_l\right] = \sum_{l=1}^{N}\frac{1}{2}\lambda_l(y_l - v_l/\lambda_l)^2 - \sum_{l=1}^{N}\frac{1}{2}v_l^2/\lambda_l. \tag{D.4}$$

Defining

$$\tilde{y}_l \equiv y_l - v_l/\lambda_l \tag{D.5}$$

and expressing the integral in terms of the new variable yields

$$I(\mathbf{A},\mathbf{b}) = \prod_{i=1}^{n}\int_{-\infty}^{\infty} \mathrm{d}\tilde{y}_i \, \mathrm{e}^{-\frac{\beta}{2}\lambda_i \tilde{y}_i^2} \mathrm{e}^{\frac{\beta}{2}\lambda_i^{-1} v_i^2} = \prod_{i=1}^{n} \sqrt{\frac{2\pi}{\beta\lambda_i}} \, \mathrm{e}^{\frac{\beta}{2}\lambda_i^{-1} v_i^2} = \left(\frac{2\pi}{\beta}\right)^{n/2} |\mathbf{A}|^{-1/2} \, \mathrm{e}^{\frac{\beta}{2}\mathbf{b}^\top \mathbf{A}^{-1}\mathbf{b}}. \tag{D.6}$$

Now let us calculate the (scaled) first moment of the multivariate Gaussian distribution,

$$\mathbf{j}(\mathbf{M},\mathbf{A},\mathbf{b}) = \int \mathrm{d}\mathbf{x} \, (\mathbf{M}\mathbf{x}) \exp\left\{-\beta\left[\frac{1}{2}\mathbf{x}^\top \mathbf{A}\mathbf{x} - \mathbf{b}^\top \mathbf{x}\right]\right\}, \tag{D.7}$$

where $\mathbf{M}$ is some general matrix. We express the multiplicative factor as

$$\mathbf{M}\mathbf{x} = \mathbf{M}\mathbf{U}\mathbf{y} = \mathbf{M}\mathbf{U}\left(\tilde{\mathbf{y}} + \mathbf{\Lambda}^{-1}\mathbf{v}\right) \tag{D.8}$$

and substitute into the integral over $\tilde{y}_i$. The linear term vanishes upon integration, leaving

$$\mathbf{j}(\mathbf{M},\mathbf{A},\mathbf{b}) = I(\mathbf{A},\mathbf{b})\mathbf{M}\mathbf{U}\mathbf{\Lambda}^{-1}\mathbf{v} = I(\mathbf{A},\mathbf{b})\mathbf{M}\mathbf{A}^{-1}\mathbf{b}. \tag{D.9}$$

Finally, we calculate the (scaled) second moment

$$K(\mathbf{M},\mathbf{A},\mathbf{b}) = \int \mathrm{d}\mathbf{x} \, (\mathbf{x}^\top \mathbf{M}\mathbf{x}) \exp\left\{-\beta\left[\frac{1}{2}\mathbf{x}^\top \mathbf{A}\mathbf{x} - \mathbf{b}^\top \mathbf{x}\right]\right\}. \tag{D.10}$$

Writing

$$\mathbf{x}^\top \mathbf{M}\mathbf{x} = \left[\mathbf{U}^\top \mathbf{x}\right]^\top \mathbf{U}^\top \mathbf{M}\mathbf{U}\left[\mathbf{U}^\top \mathbf{x}\right] \equiv \mathbf{y}^\top \mathbf{\Gamma}\mathbf{y}, \tag{D.11}$$

we expand a single term

$$y_i \Gamma_{ij} y_j = \tilde{y}_i \Gamma_{ij} \tilde{y}_j + v_i \lambda_i^{-1} \Gamma_{ij} \tilde{y}_j + \tilde{y}_i \Gamma_{ij} \lambda_j^{-1} v_j + v_i \lambda_i^{-1} \Gamma_{ij} \lambda_j^{-1} v_j. \tag{D.12}$$

The middle terms are odd and vanish upon integration. The remaining two terms yield

$$K(\mathbf{M},\mathbf{A},\mathbf{b}) = I(\mathbf{A},\mathbf{b})\left(\frac{1}{\beta}\mathrm{Tr}[\mathbf{A}^{-1}\mathbf{M}] + \mathbf{b}^\top \mathbf{A}^{-1}\mathbf{M}\mathbf{A}^{-1}\mathbf{b}\right). \tag{D.13}$$

D.2 Matrix block-*LDU* decomposition

Consider a square matrix $\mathbf{M}$ and its inverse $\mathbf{m}$, that are subdivided into blocks according to

$$\mathbf{M} = \begin{pmatrix} \mathbf{A} & \mathbf{B} \\ \mathbf{C} & \mathbf{D} \end{pmatrix} \qquad \mathbf{m} = \begin{pmatrix} \mathbf{a} & \mathbf{b} \\ \mathbf{c} & \mathbf{d} \end{pmatrix}, \tag{D.14}$$

where $\mathbf{A}$, $\mathbf{B}$, $\mathbf{C}$, $\mathbf{D}$ are $u \times u$, $u \times v$, $v \times u$, and $v \times v$ respectively, and the same holds for the blocks in $\mathbf{m}$. The matrix $\mathbf{M}$ can be decomposed as [137]

$$\begin{pmatrix} \mathbf{A} & \mathbf{B} \\ \mathbf{C} & \mathbf{D} \end{pmatrix} = \underbrace{\begin{pmatrix} \mathbf{I}_{uu} & \mathbf{B}\mathbf{D}^{-1} \\ \mathbf{0}_{vu} & \mathbf{I}_{vv} \end{pmatrix}}_{\mathbf{U}} \underbrace{\begin{pmatrix} \mathbf{M}/\mathbf{D} & \mathbf{0}_{uv} \\ \mathbf{0}_{vu} & \mathbf{D} \end{pmatrix}}_{\mathbf{\Sigma}} \underbrace{\begin{pmatrix} \mathbf{I}_{uu} & \mathbf{0}_{uv} \\ \mathbf{D}^{-1}\mathbf{C} & \mathbf{I}_{vv} \end{pmatrix}}_{\mathbf{L}} \tag{D.15}$$

where $\mathbf{I}_{uu}$ is a $u \times u$ identity matrix and $\mathbf{0}_{uv}$ is a $u \times v$ matrix of zeros. $\mathbf{M}/\mathbf{D}$ denotes the Schur complement of block $\mathbf{D}$ in matrix $\mathbf{M}$, and is defined as

$$\mathbf{M}/\mathbf{D} \coloneqq \mathbf{A} - \mathbf{B}\mathbf{D}^{-1}\mathbf{C}. \tag{D.16}$$

It can be shown that

$$\mathbf{L}^{-1} = \begin{pmatrix} \mathbf{I}_{uu} & \mathbf{0}_{uv} \\ -\mathbf{D}^{-1}\mathbf{C} & \mathbf{I}_{vv} \end{pmatrix}, \tag{D.17}$$

and that an analogous result holds for $\mathbf{U}$. Using this, the inverse of $\mathbf{M}$ can be written as

$$\mathbf{M}^{-1} = \mathbf{L}^{-1}\mathbf{\Sigma}^{-1}\mathbf{U}^{-1} = \begin{pmatrix} [\mathbf{M}/\mathbf{D}]^{-1} & -[\mathbf{M}/\mathbf{D}]^{-1}\mathbf{B}\mathbf{D}^{-1} \\ -\mathbf{D}^{-1}\mathbf{C}[\mathbf{M}/\mathbf{D}]^{-1} & [\mathbf{M}/\mathbf{A}]^{-1} \end{pmatrix}. \tag{D.18}$$

Comparing this block-wise to $\mathbf{M}^{-1} = \mathbf{m}$, we arrive at the relations

$$[\mathbf{M}/\mathbf{D}]^{-1} = \mathbf{a} \qquad [\mathbf{M}/\mathbf{A}]^{-1} = \mathbf{d}, \tag{D.19a}$$

$$-\mathbf{D}^{-1}\mathbf{C} = \mathbf{c}\mathbf{a}^{-1} \qquad -\mathbf{B}\mathbf{D}^{-1} = \mathbf{a}^{-1}\mathbf{b}, \tag{D.19b}$$

which we use when calculating the mean-field Hamiltonian in Section 4.2.

References

1. R. Shankar. *Principles of Quantum Mechanics* 2nd ed. (Springer US, 2012).
2. H. Wang, X. Sun, and W. H. Miller. *J. Chem. Phys.* **108,** 9726–9736 (1998).
3. X. Sun, H. Wang, and W. H. Miller. *J. Chem. Phys.* **109,** 4190–4200 (1998).
4. W. H. Miller. *J. Phys. Chem. A* **105,** 2942–2955 (2001).
5. I. R. Craig and D. E. Manolopoulos. *J. Chem. Phys.* **121,** 3368–3373 (2004).
6. I. R. Craig and D. E. Manolopoulos. *J. Chem. Phys.* **122,** 084106 (2005).
7. I. R. Craig and D. E. Manolopoulos. *J. Chem. Phys.* **123,** 034102 (2005).
8. T. F. Miller and D. E. Manolopoulos. *J. Chem. Phys.* **122,** 184503 (2005).
9. T. F. Miller and D. E. Manolopoulos. *J. Chem. Phys.* **123,** 154504 (2005).
10. S. Habershon, G. S. Fanourgakis, and D. E. Manolopoulos. *J. Chem. Phys.* **129,** 074501 (2008).
11. S. Habershon, T. E. Markland, and D. E. Manolopoulos. *J. Chem. Phys.* **131,** 024501 (2009).
12. N. Boekelheide, R. Salomon-Ferrer, and T. F. Miller. *Proc. Natl. Acad. Sci.* **108,** 16159–16163 (2011).
13. J. B. Rommel, T. P. M. Goumans, and J. Kästner. *J. Chem. Theory Comput.* **7,** 690–698 (2011).
14. S. Habershon, D. E. Manolopoulos, T. E. Markland, and T. F. Miller. *Annu. Rev. Phys. Chem.* **64,** 387–413 (2013).
15. M. Rossi, M. Ceriotti, and D. E. Manolopoulos. *J. Chem. Phys.* **140,** 234116 (2014).

16. M. Rossi, H. Liu, F. Paesani, J. Bowman, and M. Ceriotti. *J. Chem. Phys.* **141,** 181101 (2014).

17. G. R. Medders and F. Paesani. *J. Chem. Theory Comput.* **11,** 1145–1154 (2015).

18. S. Althorpe *et al. Faraday Discuss.* **195,** 671–698 (2016).

19. Y. V. Suleimanov, F. J. Aoiz, and H. Guo. *J. Phys. Chem. A* **120,** 8488–8502 (2016).

20. S. K. Reddy, D. R. Moberg, S. C. Straight, and F. Paesani. *J. Chem. Phys.* **147,** 244504 (2017).

21. B. Cheng, E. A. Engel, J. Behler, C. Dellago, and M. Ceriotti. *Proc. Natl. Acad. Sci.* **116,** 1110–1115 (2019).

22. R. L. Benson, G. Trenins, and S. C. Althorpe. *Faraday Discuss.* **221,** 350–366 (2020).

23. M. Born and R. Oppenheimer. *Ann. Phys.* **389,** 457–484 (1927).

24. J. C. Light, I. P. Hamilton, and J. V. Lill. *J. Chem. Phys.* **82,** 1400–1409 (1985).

25. D. T. Colbert and W. H. Miller. *J. Chem. Phys.* **96,** 1982–1991 (1992).

26. H.-D. Meyer, U. Manthe, and L. S. Cederbaum. *Chem. Phys. Lett.* **165,** 73–78 (1990).

27. U. Manthe, H.-D. Meyer, and L. S. Cederbaum. *J. Chem. Phys.* **97,** 3199–3213 (1992).

28. H. Wang and M. Thoss. *J. Chem. Phys.* **119,** 1289–1299 (2003).

29. H. Wang. *J. Phys. Chem. A* **119,** 7951–7965 (2015).

30. R. Ellerbrock and U. Manthe. *J. Chem. Phys.* **147,** 241104 (2017).

31. R. Ellerbrock and U. Manthe. *J. Chem. Phys.* **148,** 224303 (2018).

32. T. Carrington. *J. Chem. Phys.* **146,** 120902 (2017).

33. P. S. Thomas, T. Carrington, J. Agarwal, and H. F. Schaefer. *J. Chem. Phys.* **149,** 064108 (2018).

34. R. Feynman and F. Vernon. *Ann. Phys.* **24,** 118–173 (1963).

35. R. Feynman and A. Hibbs. *Quantum Mechanics and Path Integrals* (Dover Publications, 2010).

36. M. Topaler and N. Makri. *J. Chem. Phys.* **101,** 7500–7519 (1994).

37. N. Makri. *Chem. Phys. Lett.* **593,** 93–103 (2014).
38. Y. Tanimura and R. Kubo. *J. Phys. Soc. Jpn.* **58,** 101–114 (1989).
39. Y. Tanimura and P. G. Wolynes. *Phys. Rev. A* **43,** 4131–4142 (1991).
40. C. A. Mujica-Martinez and P. Nalbach. *Ann. Phys.* **527,** 592–600 (2015).
41. H.-G. Duan, A. G. Dijkstra, P. Nalbach, and M. Thorwart. *Phys. Rev. E* **92,** 042708 (2015).
42. L. Arceci, S. Barbarino, R. Fazio, and G. E. Santoro. *Phys. Rev. B* **96,** 054301 (2017).
43. L. Chen, Y. Zhao, and Y. Tanimura. *J. Phys. Chem. Lett.* **6,** 3110–3115 (2015).
44. L. Song and Q. Shi. *Phys. Rev. B* **95,** 064308 (2017).
45. R. Zwanzig. *Nonequilibrium Statistical Mechanics* (Oxford University Press, 2001).
46. B. Leimkuhler and S. Reich. *Simulating Hamiltonian Dynamics* (Cambridge University Press, 2005).
47. M. Hillery, R. O'Connell, M. Scully, and E. Wigner. *Phys. Rep.* **106,** 121–167 (1984).
48. M. Allen and D. Tildesley. *Computer Simulation of Liquids* (Clarendon Press, 1989).
49. D. Frenkel and B. Smit. *Understanding Molecular Simulation: From Algorithms to Applications* 2nd ed. (Elsevier Science, 2001).
50. M. Tuckerman. *Statistical Mechanics: Theory and Molecular Simulation* (Oxford University Press, 2010).
51. A. R. Walton and D. E. Manolopoulos. *Mol. Phys.* **87,** 961–978 (1996).
52. W. H. Miller. *J. Chem. Phys.* **125,** 132305 (2006).
53. K. G. Kay. *Chem. Phys.* **322,** 3–12 (2006).
54. G. Di Liberto, R. Conte, and M. Ceotto. *J. Chem. Phys.* **148,** 014307 (2018).
55. H. Wang, D. E. Manolopoulos, and W. H. Miller. *J. Chem. Phys.* **115,** 6317–6326 (2001).
56. A. L. Kaledin and W. H. Miller. *J. Chem. Phys.* **118,** 7174 (2003).
57. F. Gabas, G. Di Liberto, and M. Ceotto. *J. Chem. Phys.* **150,** 224107 (2019).

58. R. Conte, L. Parma, C. Aieta, A. Rognoni, and M. Ceotto. *J. Chem. Phys.* **151,** 214107 (2019).

59. S. Nielsen, R. Kapral, and G. Ciccotti. *J. Chem. Phys.* **115,** 6543 (2001).

60. J. Liu. *Int. J. Quantum Chem.* **115,** 657–670 (2015).

61. J. Liu and W. H. Miller. *J. Chem. Phys.* **131,** 074113 (2009).

62. J. Liu, W. H. Miller, F. Paesani, W. Zhang, and D. A. Case. *J. Chem. Phys.* **131,** 164509 (2009).

63. J. Liu, W. H. Miller, G. S. Fanourgakis, S. S. Xantheas, S. Imoto, and S. Saito. *J. Chem. Phys.* **135,** 244503 (2011).

64. X. Liu and J. Liu. *Mol. Phys.* **116,** 755–779 (2018).

65. J. Liu, A. Nakayama, and N. Makri. *Mol. Phys.* **104,** 1267–1274 (2006).

66. W. H. Miller. *J. Chem. Phys.* **136,** 210901 (2012).

67. Q. Shi and E. Geva. *J. Chem. Phys.* **119,** 9030–9046 (2003).

68. J. A. Poulsen, G. Nyman, and P. J. Rossky. *J. Phys. Chem. B* **108,** 19799–19808 (2004).

69. J. Liu, B. J. Alder, and W. H. Miller. *J. Chem. Phys.* **135,** 114105 (2011).

70. D. Chandler and P. G. Wolynes. *J. Chem. Phys.* **74,** 4078–4095 (1981).

71. T. E. Markland and D. E. Manolopoulos. *J. Chem. Phys.* **129,** 024105 (2008).

72. M. Ceriotti, D. E. Manolopoulos, and M. Parrinello. *J. Chem. Phys.* **134,** 084104 (2011).

73. M. Ceriotti and D. E. Manolopoulos. *Phys. Rev. Lett.* **109,** 100604 (2012).

74. V. Kapil, J. Behler, and M. Ceriotti. *J. Chem. Phys.* **145,** 234103 (2016).

75. V. Kapil, J. VandeVondele, and M. Ceriotti. *J. Chem. Phys.* **144,** 054111 (2016).

76. V. Kapil, A. Cuzzocrea, and M. Ceriotti. *J. Phys. Chem. B* **122,** 6048–6054 (2018).

77. M. Veit, S. K. Jain, S. Bonakala, I. Rudra, D. Hohl, and G. Csányi. *J. Chem. Theory Comput.* **15,** 2574–2586 (2019).

78. J. Cao and G. A. Voth. *J. Chem. Phys.* **100,** 5106–5117 (1994).

79. J. O. Richardson and S. C. Althorpe. *J. Chem. Phys.* **131,** 214106 (2009).

80. T. J. H. Hele and S. C. Althorpe. *J. Chem. Phys.* **138,** 084108 (2013).

81. T. J. H. Hele, M. J. Willatt, A. Muolo, and S. C. Althorpe. *J. Chem. Phys.* **142,** 134103 (2015).

82. T. J. H. Hele, M. J. Willatt, A. Muolo, and S. C. Althorpe. *J. Chem. Phys.* **142,** 191101 (2015).

83. T. J. H. Hele. *Mol. Phys.* **114,** 1461–1471 (2016).

84. M. Rossi, V. Kapil, and M. Ceriotti. *J. Chem. Phys.* **148,** 102301 (2018).

85. A. Witt, S. D. Ivanov, M. Shiga, H. Forbert, and D. Marx. *J. Chem. Phys.* **130,** 194510 (2009).

86. S. D. Ivanov, A. Witt, M. Shiga, and D. Marx. *J. Chem. Phys.* **132,** 031101 (2010).

87. A. Nitzan. *Chemical Dynamics in Condensed Phases: Relaxation, Transfer, and Reactions in Condensed Molecular Systems* (Oxford University Press, 2013).

88. M. J. Willatt. *Matsubara Dynamics and its Practical Implementation.* PhD Thesis (2017).

89. K. Riley, M. Hobson, and S. Bence.
Mathematical Methods for Physics and Engineering: A Comprehensive Guide 3rd ed. (Cambridge University Press, 2006).

90. R. Feynman. *Statistical Mechanics: A Set Of Lectures* (Avalon Publishing, 1998).

91. M. Suzuki. *J. Math. Phys.* **26,** 601–612 (1985).

92. M. Ceriotti, M. Parrinello, T. E. Markland, and D. E. Manolopoulos.
J. Chem. Phys. **133,** 124104 (2010).

93. B. J. Braams and D. E. Manolopoulos. *J. Chem. Phys.* **125,** 124105 (2006).

94. Y. V. Suleimanov. *J. Phys. Chem. C* **116,** 11141–11153 (2012).

95. B. Cheng, A. T. Paxton, and M. Ceriotti. *Phys. Rev. Lett.* **120,** 225901 (2018).

96. T. Yoshikawa, T. Takayanagi, H. Kimizuka, and M. Shiga.
J. Phys. Chem. C **116,** 23113–23119 (2012).

97. Y. Litman, J. Behler, and M. Rossi. *Faraday Discuss.* **221,** 526–546 (2020).

98. W. Press, S. Teukolsky, B. Flannery, and W. Vetterling.
Numerical Recipes in FORTRAN 77 (Cambridge University Press, 1992).

99. C. Chakravarty. *Int. Rev. Phys. Chem.* **16,** 421–444 (1997).

100. C. Chakravarty, M. C. Gordillo, and D. M. Ceperley. *J. Chem. Phys.* **109,** 2123–2134 (1998).

101. U. Weiss. *Quantum Dissipative Systems* (World Scientific, 2012).

102. G. Bussi and M. Parrinello. *Comput. Phys. Commun.* **179,** 26–29 (2008).

103. R. Ramírez and T. López-Ciudad. *J. Chem. Phys.* **111,** 3339–3348 (1999).

104. T. D. Hone, P. J. Rossky, and G. A. Voth. *J. Chem. Phys.* **124,** 154103 (2006).

105. W. H. Miller. *J. Chem. Phys.* **62,** 1899–1906 (1975).

106. J. O. Richardson. *J. Chem. Phys.* **144,** 114106 (2016).

107. S. Andersson, G. Nyman, A. Arnaldsson, U. Manthe, and H. Jónsson.
J. Phys. Chem. A **113,** 4468–4478 (2009).

108. J.-P. Ryckaert, G. Ciccotti, and H. J. Berendsen. *J. Comput. Phys.* **23,** 327–341 (1977).

109. H. C. Andersen. *J. Comput. Phys.* **52,** 24–34 (1983).

110. B. Leimkuhler and C. Matthews. *Proc. R. Soc. A* **472,** 20160138 (2016).

111. H. Partridge and D. W. Schwenke. *J. Chem. Phys.* **106,** 4618–4639 (1997).

112. D. W. Schwenke and H. Partridge. *J. Chem. Phys.* **113,** 6592–6597 (2000).

113. C. Eckart. *Phys. Rev.* **47,** 552–558 (1935).

114. E. Wilson, J. Decius, and P. Cross.
Molecular Vibrations: The Theory of Infrared and Raman Vibrational Spectra
(Dover Publications, 1980).

115. F. Jørgensen. *Int. J. Quantum Chem.* **14,** 55–63 (1978).

116. K. N. Kudin and A. Y. Dymarsky. *J. Chem. Phys.* **122,** 224105 (2005).

117. S. C. Althorpe *et al. Faraday Discuss.* **221,** 478–500 (2020).

118. G. J. Martyna. *J. Chem. Phys.* **104,** 2018–2027 (1996).

119. T. D. Hone and G. A. Voth. *J. Chem. Phys.* **121,** 6412–6422 (2004).

120. J. Tennyson, M. A. Kostin, P. Barletta, G. J. Harris, O. L. Polyansky, J. Ramanlal, and N. F. Zobov. *Comput. Phys. Commun.* **163,** 85–116 (2004).

121. J. E. Bertie, H. J. Labbé, and E. Whalley. *J. Chem. Phys.* **50,** 4501–4520 (1969).

122. E. Whalley. *Can. J. Chem.* **55,** 3429–3441 (1977).

123. Y. Wang and J. M. Bowman. *J. Chem. Phys.* **134,** 154510 (2011).

124. H. Liu, Y. Wang, and J. M. Bowman. *J. Phys. Chem. Lett.* **3,** 3671–3676 (2012).

125. H. Liu, Y. Wang, and J. M. Bowman. *J. Phys. Chem. B* **118,** 14124–14131 (2014).

126. H. Liu, Y. Wang, and J. M. Bowman. *J. Am. Chem. Soc.* **136,** 5888–5891 (2014).

127. V. Kapil *et al. Comput. Phys. Commun.* **236,** 214–223 (2019).

128. K. M. Hunter, F. A. Shakib, and F. Paesani. *J. Phys. Chem. B* **122,** 10754–10761 (2018).

129. S. K. Reddy *et al. J. Chem. Phys.* **145,** 194504 (2016).

130. H. Liu, Y. Wang, and J. M. Bowman. *J. Phys. Chem. B* **120,** 1735–1742 (2016).

131. L. Landau and E. Lifshitz. *Mechanics* 3rd ed. (Elsevier Science, 1982).

132. A. Vincent. *Molecular Symmetry and Group Theory* (Wiley, 2013).

133. H. Kleinert.
Path Integrals in Quantum Mechanics, Statistics, Polymer Physics, and Financial Markets (World Scientific, 2009).

134. F. Olver *et al. NIST Digital Library of Mathematical Functions.*
http://dlmf.nist.gov/, Release 1.0.25 of 2019-12-15.

135. J. A. Hayward and J. R. Reimers. *J. Chem. Phys.* **106,** 1518–1529 (1997).

136. J. D. Bernal and R. H. Fowler. *J. Chem. Phys.* **1,** 515–548 (1933).

137. F. Zhang. *The Schur complement and its applications* (Springer, 2005).